Université catholique de Louvain
Secteur des Sciences et Technologies
Institut de Recherche en Mathématique et Physique
Centre for Cosmology, Particle Physics and Phenomenology

MEASUREMENT OF EXCLUSIVE TWO-PHOTON PROCESSES WITH DILEPTON FINAL STATES IN *pp* COLLISIONS AT THE LHC

Doctoral dissertation presented by

Laurent Forthomme

in fulfilment of the requirements for the degree of
Doctor of Philosophy in Science

Members of the jury:

Prof. Krzysztof Piotrzkowski (supervisor)	UCL, Belgium
Prof. Vincent Lemaitre (president)	UCL, Belgium
Prof. Andrea Giammanco (secretary)	UCL, Belgium
Prof. Laurent Favart	ULB, Belgium
Prof. João Varela	LIP, Portugal

March 2016

CONTENTS

This work has been supported by:

REMERCIEMENTS / ACKNOWLEDGEMENTS

"No estoy seguro de que yo exista, en realidad. Soy todos los autores que he leído, toda la gente que he conocido, todas las mujeres que he amado. Todas las ciudades que he visitado, todos mis antepasados..."

— Jorge Luis Borges (*El Pais*)

My first thanks go to Krzysztof, who allowed me to jump on this doctoral adventure. Beyond the countless tips – either on physics, professional, or other matters – you gave out, you trusted me from the beginning and gave me a large freedom during these four years.

Many thanks to all members of my commitee, for accepting this heavy task of guiding me towards the finalisation of this work.

A warm thank you to Jonathan, for your invariable good will often going beyond understanding. Thanks to you I have been trained by one of the most famous CMS muons experts, but also by a very warm and caring person.

Thank you Gustavo, for these nice conversations on topics as vast as Belgian beers, global muon HLT efficiencies, exclusive physics, the Brazilian habits (especially the correct pronunciation of *livro de cabeceira*), and the proper usage of `Fortran`'s common blocks.

Thanks to Mohsen, Alireza, José, *et al* – all guys orbiting around CERN's building 20. It was a great pleasure to share more than a test beam preparation and operation around these two timing detectors. The long sleepless nights taking care of the *baby* would have been worthless without your kindliness, generosity (and sometimes indulgence).

Je remercie l'équipe administrative de CP3, Ginette, Luc, Carinne et Carine, ainsi que toute l'équipe technique – en particulier Jérôme et Pavel. Combien d'heures, de jours, voire de semaines supplémentaires m'auraient été nécessaires sans votre aide précieuse tout au long de ces années ?

Merci à mes amis, compagnons de chemin, du *Certino* ou du *Petit-Ry*, du sempiternel "petit café" devant la gare, de ma verte province, du *grand-Nord*, de la cité ardente, et de partout ailleurs. Vous qui avez su me faire vivre tout le spectre continu de la vie par vos sourires, vos joies, vos colères, vos peines, vos inquiétudes, vos encouragements, vos certitudes et vos incertitudes, et vos expériences aussi nombreuses que variées.

Et même si ils se retrouvent déjà en partie dans le paragraphe précédent, un merci tout particulier revient à mes co-doctorants et compagnons de cordée, de l'UCL et d'ailleurs. Il est vrai que passer ces quelques années à travailler ensemble (parfois dans un espace confiné comme le `e265` ou le `40-4B20` en pleine CMS week) devait nous rapprocher, mais par votre raison, votre générosité, votre motivation et par notre soutien mutuel durant ces nombreux moments difficiles, l'aventure doctorale n'en aura été que plus riche.

Ein besonderer Dank ergeht an Thomas und Ludivine für ihre wertvolle Unterstützung beim Korrekturlesen.

Merci à mes parents, ma famille (en particulier Estelle), pour m'avoir mené jusqu'ici, et avoir cru en moi jusqu'au bout. Si j'ai pu me consacrer pleinement à ces quatre années de recherche, c'est en grande partie grâce à votre soutien inconditionnel et cette curiosité naturelle que vous m'avez transmise.

Enfin, merci à toi, ma voisine de table et de vie, toi qui as su rester patiente jusqu'á la fin de mes tours et détours, malgré les innombrables nuits débutées seule à entendre résonner le cliquetis des touches de mon clavier, et mes humeurs variables au fil des jours. Par ta tendresse et tes encouragements, tu as su me raccrocher à mes rêves et idéaux, et me faire regarder vers l'avenir.

INTRODUCTION

"La qualité d'un homme se calcule à sa démesure ; tentez, essayez, échouez même, ce sera votre réussite."

— Jacques Brel

The major subject of this thesis involves novel studies of the electroweak gauge boson couplings. As a generic tool to probe such couplings, the processes induced by two-photon fusion will be used because of the unique sensitivity to these couplings they provide at LHC energies. The pioneering measurements of two such two-photon processes, $\gamma\gamma \to W^+W^-$ and $\gamma\gamma \to ZZ$, will be presented.

In chapter 1, the theoretical background regarding two-photon processes will be presented, including the introduction of a simplified factorisation approach to the two-photon production processes which provides a general framework for phenomenological predictions.

Then, in chapter 2, the concept of colliding particle experiments will be described, along with the associated *nomenclature* and detection principles. In particular, the CMS experiment will be presented with all its constitutive elements that enable the detection of two-photon processes.

Afterwards, the measurements of two-photon processes performed with the CMS experiment will be discussed in chapter 3. The associated results for the two-photon exclusive production of lepton and gauge boson pairs will be described in detail, including the observed sensitivity to anomalous behaviours of their couplings to photons.

Finally, in chapter 4, the upgrade of the CMS apparatus in its very forward region will be motivated and described. The focus is set on the joint CMS-TOTEM Precision Proton Spectrometer currently under preparation. As a motivation for the installation of this new detector, a study of one of the measurements described in chapter 3 is discussed again with the inclusion of this additional spectrometer, thus emphasising its impact on the measurement sensitivity. In this context, the `GasToF` detector developed and built at UCLOUVAIN will be presented.

In the scope of this PhD thesis, the author's contributions to the presented research followed three separate directions.

Firstly, he investigated the phenomenology of the two-photon production of lepton pairs, and in particular the quasi-exclusive contribution that involves proton dissociation. Given matrix elements relying on a novel factorisation method of the unintegrated photon fluxes, studied in collaboration with a team of phenomenologists, he developed a Monte Carlo event generator enabling to fully simulate this process using modern computing tools. He extracted the quasi-exclusive to exclusive (or inelastic-to-elastic) scaling factor for any two-photon induced process, produced within a clearly defined kinematic range – crucial for proper simulations.

Secondly, he took part in two analyses using the two high-statistics datasets collected by the CMS experiment in Run-1 and aiming for the first observation of the two-photon exclusive production of $W^{\pm}$ gauge boson pairs at two centre of mass energies. He also studied the vertexing and pileup dependence on the discrepancy observed in the main control region of the “reference" two-photon production of lepton pairs as a mean to investigate the potential flaws in the simulation of the tracks multiplicity in CMS.

Furthermore, he developed a new analysis to probe the two-photon production of neutral Z boson pairs, enabling to quote the first limits ever reached at the LHC on this fully neutral 4-boson coupling which is suppressed at the tree level in the standard model.

Finally, he participated in the study, the development and the construction of `GasToF`, a high-resolution time of flight detector, as part of the *R&D* programme of the joint CMS-TOTEM PPS project. This apparatus was tested at the CERN *Super Proton Synchrotron* during a Fall 2015 test beam campaign. For this, the author was deeply involved in the development of the data acquisition system for this timing detector along with `Quartic`, another prototype used as a benchmark for the PPS. This development was done both on the software and on the hardware sides. At the time of writing this thesis, the collected data is being analysed.

1

TWO-PHOTON PROCESSES

1.1 PRELIMINARY NOTE: MATTER AND INTERACTIONS

In 1909, H. Geiger and his undergraduate student, E. Marsden, performed a scattering experiment under the supervision of a professor hosting them at the University of Manchester, E. Rutherford.

As a test of the contemporary description of the nucleus, a beam of alpha particles was directed towards a thin leaf of gold [1]. Behind this leaf was an extended angular coverage of "detectors" consisting in a fluorescent screen to enable a direct scintillation, visible by a human eye, once illuminated by scattered electrons.

The angular distribution of scattered components was expected to be centred on the incident beam direction. Indeed, with the previous belief that the nucleus itself was containing all positive and negative charges in a rather dense structure (just like a "plum pudding" described by the Thomson nuclear model), the homogeneous location of all components would ensure a minimal scattering effect. Therefore, it predicted a narrow, collimated beam downstream of the foil.

However, the observed distribution, pictured in Fig. 1.1, showed a broad coverage of scattered electrons. It shed light to a more complex structure, where the nucleus is to be considered as a whole, at a distinct distance/energy scale from the electron cloud surrounding it.

This rather "simple" scattering experiment provided a first insight on a structural composition of the nucleus much more complex than any previous modelling. Furthermore, it opened the door to a broad field later known as nuclear physics. The simplest case to study in this domain contains only one single component in its core: the hydrogen nucleus, consisting of a single proton.

1.1.1 *What is in a proton?*

At the middle of the twentieth century, no further sub-components of a proton (or, more generally, a nucleon) were observed.

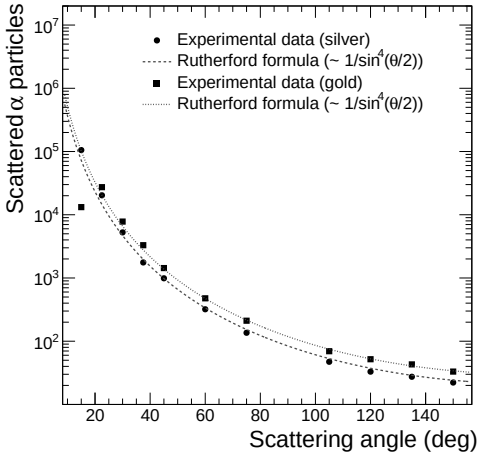

Figure 1.1: Distribution of scattering angles as observed by Geiger and Marsden in their experiment. The dotted line pictures the theoretical prediction (aka "Rutherford formula") behaving like the inverse of the fourth power of half the scattering angle's sine. Figure extracted from [1].

However, with time, the scattering of incoming particles beams with higher and higher energies enabled to probe shorter and shorter distances inside these nuclei, as expected from the extension of the possible energy exchange range. An increasing rate of new particle discoveries were then claimed in many decays and cosmic rays observations, fixed target, or colliding experiments.

To be able to build a model of the nucleon and characterise its interactions with the surroundings, some sub-components were postulated to appear within their core. One acute description was given by the *parton* model, as proposed by Feynman in the 1960s [2], enabling to treat the dynamics of their building blocks.

Provided that the overall composition of these partons inside an observable nucleon is either electrically charged (the proton has a positive electric charge), or neutral (like the neutron), such components are required to carry an electric (fractional) charge as well.

One of the major drawback of this postulate lies in the required nucleon stability problem it raises naturally, as these components must be observed in bound states (such as the proton, the neutron, or the vast collection of pions, kaons, and other compositions as observed at that time). The reason for the partons to bind together inside a nucleon is indeed non-trivial when the components are supposedly attracting or repelling each other due to the electromagnetic force. Hence, another category of partons was introduced to solve this theoretical issue, "gluing" all the partons together with an additional type of charge, the *colour* charge.

In today's terms, one describes these "matter" partons as *quarks*, building blocks of all nucleon "matter", bound together with *gluons* to ensure their hosts' relative stability. The field theory describing the quark interactions, known as quantum chromodynamics (QCD), ensures that quarks are bound as observed in nature. In our current understanding of the whole picture, two types of bound states can be distinguished:

- three quarks or anti-quarks (such as the proton or neutron, referred to as *baryons*, as a reference to their relative heaviness),
- a pair of quark-antiquark (named *mesons*, such as *pions* $\pi^{\pm}, \pi^{0}$, *kaons*).

In addition to these, one may also quote "exotic" bound states. To name a few, one can emphasise the recent experimental discovery for *tetraquarks* (four valence quarks) and *pentaquarks* [3].

Following Rutherford's attempts to probe the atomic structure, a worthy heir of his technique furthermore enabled to probe the inner structure of the proton through its interaction with simpler fundamental particles. The apparatus itself, was once part of the most energetic machines ever built.

Located in the outskirts of Hamburg, Germany, HERA (*Hadron-Elektron-RingAnlage*, or *Hadron-Electron Ring Accelerator*), was an electron-proton collider in operation between 1992 and 2007. It collided a 27.6 GeV electron (or positron) beam with a proton beam in an energy range extending from 820 to 920 GeV, similarly to the Rutherford experiment's alpha particle beam scattered by a heavy target. The experiments built around the collision points allowed to probe the inner structure of the proton, with high available energy transfers from one particle to the other.

In terms of the kinematic notations commonly used in this type of scattering experiment, and defined in Fig. 1.2, this energy transfer $Q^2 = -q^2 > 0$ could scan a wide range extending from a fraction of a GeV^2 to the order of $10^5\ \mathrm{GeV}^2$.

The extended spatial range to be probed with a higher Q^2 exchange is given by a simple geometric argument. Indeed, if one considers two colliding particles, one can picture the energy transfer between these two objects to be inversely proportional to the distance separating them, in analogue with the Coulomb force repelling charged particles. One may introduce the *impact parameter* (or distance of approach) b. The relation between the energy transfer and the impact parameter is then $Q \sim 1/b$.

Other kinematic observables of interest appearing in this scheme are the two Lorentz-invariant, dimensionless deep inelastic scattering scaling variables x and y as defined by J. Bjorken [4]:

$$x_{\mathrm{Bj}} = \frac{-q^2}{2(p\cdot q)} = \frac{Q^2}{2(p\cdot q)}, \quad y_{\mathrm{Bj}} = \frac{p\cdot q}{p\cdot k},$$

where p and q are the 4-momentum of the initial proton and of the virtual photon emitted from the electron.

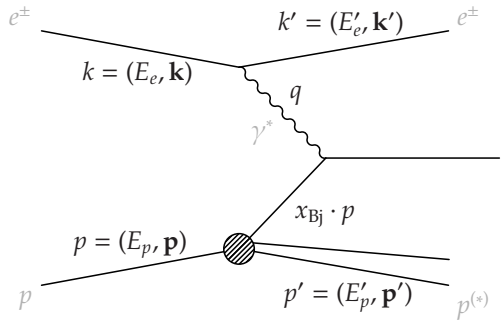

Figure 1.2: Commonly used kinematic variables of an *ep* deep inelastic scattering (DIS) experiment, such as the former HERA collider at DESY.

The first, x_{Bj}, is linked to the "inelasticity" (on the nucleon/parton side) of a given process. It defines the momentum fraction of the proton involved in the central reaction. In other words:

$$\begin{aligned} x_{\mathrm{Bj}} &= 1 \quad \text{for an elastic scattering,} \\ 0 < x_{\mathrm{Bj}} &< 1 \quad \text{for an inelastic scattering.} \end{aligned}$$

The second scaling variable gives the fractional energy loss y_{Bj} of the second incoming particle (the lepton at HERA), also comprised between 0 and 1. These two scalars are today used as a good indicator in the evaluation of several quantities of interest in high-energy physics (HEP).

The full kinematic ranges allowed for the two-dimensional parameter space $x_{\mathrm{Bj}} - Q^2$ are pictured in Fig. 1.3. The diagonal boundaries, corresponding to $y_{\mathrm{Bj}} = 1$, picture the maximal kinematically allowed values of these ranges, given the centre of mass energy reachable by the experiment.

The most significant observable is the variation of every nucleon's substructure with respect to the probed energy range. Indeed, while a full scaling of the functions defining the nucleon structure is expected with respect to the energy transfer in a "naive" point-like approximation of the nucleon, the addition of QCD corrections in the overall scattering amplitude leads to a violation of this scaling, either at low-x_{Bj} (resp. high-x_{Bj}), where the quark content increases (resp. decreases) with Q^2. Hence, this composition has to be observed experimentally for each nucleon in a broad range of Q^2 and x_{Bj}, leading to the extraction of the probability density functions (PDF) of each parton content inside the nucleon.

In the proton case, for a proper estimation of its inner structure, the best environment where these parameterisations can be observed remains an electron-proton collider such as HERA, in which both the asymmetric collision and the fundamental nature of

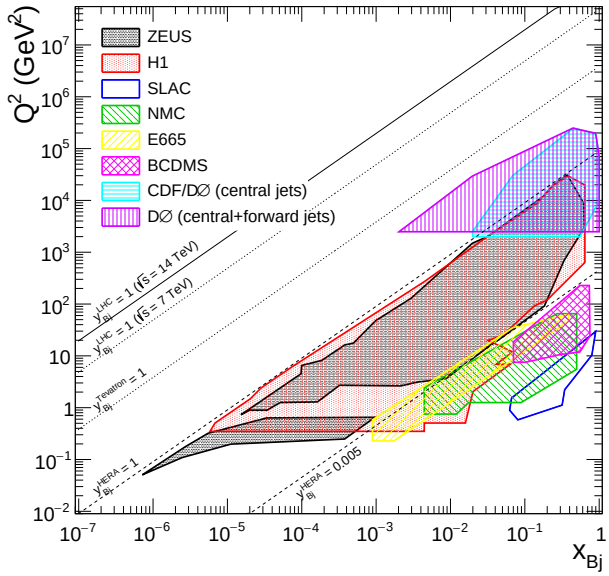

Figure 1.3: Combined deep inelastic scattering kinematic ranges allowed and probed for various pre-LHC colliders and fixed targets experiments.

the electron allow to probe it in its core. One can quote for instance the estimation of these parton contents by HERA's two main detectors, ZEUS [5] and H1 [6], leading to the measurement of all proton structure functions still heavily used nowadays. The x_{Bj} and Q^2 dependence on these PDFs are shown in Fig. 1.4 for one of the numerous parameterisations available[1]: the MSTW 2008 [7], and for two virtuality values: $Q^2 = 10$ GeV^2 and $Q^2 = 10^4$ GeV^2.

As pictured in Fig. 1.4, an increase in the energy transfer Q^2 leads to the increase of the low x_{Bj} components of the PDFs, while the large x_{Bj} contributions decrease. This behaviour is expected from the discussion given above when considering the larger phase space opened for larger virtualities, thus enabling to probe the deeper substructure of the nucleon. Its effect can be evaluated numerically for all PDFs through a system of coupled equations: the DGLAP evolution equations [8–10].

These observations and formalisms provide a common ground in the description of the matter components observed experimentally. In the next section, the interactions and hierarchies acting between all these fundamental ingredients are described.

[1] The collection of parameterisation usually differ from the various data samples used in the global fit, as well as the parametric form of the PDFs.

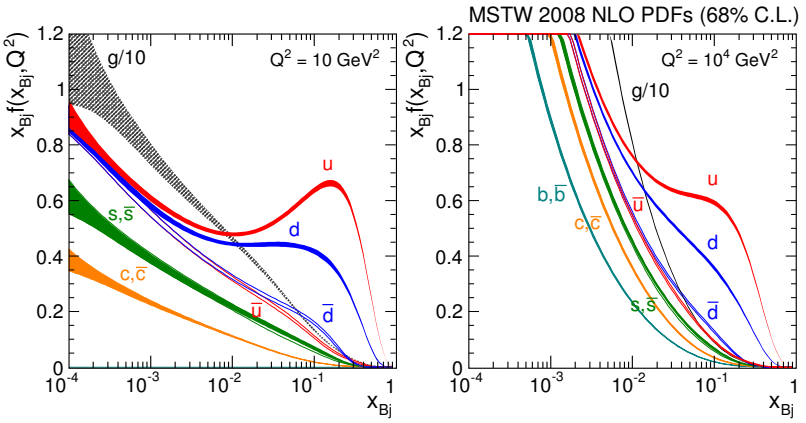

Figure 1.4: Parton density functions for the quark/antiquark and gluon parton distributions as predicted at the next-to-leading order (NLO) by the MSTW 2008 global fits. Two energy transfer scales are given for these distributions, $Q^2 = 10$ and 10^4 GeV^2. These fits are performed over a broad range of datasets, as obtained by HERA, TEVATRON, and fixed target experiments. Figure extracted from [7].

1.1.2 *The standard model of elementary interactions*

The standard model (SM) is a quantum field theory, a theoretical construction built around the high multiplicity of observations, characterisations and discoveries of particles since the first half of twentieth century. Defined in a mathematical formalism, it combines both the description of all matter components and their properties, with a modelling of all interactions known between these elements.

Either the matter constituents introduced earlier in the parton model, along with the elementary leptons, and the forces acting between these two categories are defined in terms of fields, or with the particles generated by their action. Therefore, one may divide the finite collection of particles introduced in this model into the matter components, to which both the quarks and the elementary leptons (such as the electron) belong, and the particles mediating an interaction. The criterion used to distinguish these two categories, the *fermions* and the *bosons* respectively, is a given quantum number defining their nature: the intrinsic angular momentum (or *spin*). In these two categories, it can either take an odd or an even multiple of half the Planck constant value $\hbar$.

Among the quantum numbers associated to each field, one also finds the intrinsic charges. These can be the common electric charge (integer for all particles but the free quarks) introduced in electromagnetism, or the threefold colour charge of the strong interaction. The colour charge is only carried by the quarks and gluons. Each quark can therefore be characterised by one single colour charge (or anti-colour for

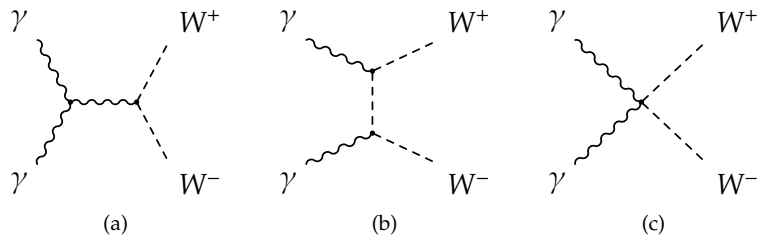

Figure 1.5: Trilinear (*s*-channel (a) and *t*-channel (b) diagrams) and quartic (diagram (c)) gauge couplings involved in the $\gamma\gamma \to W^+W^-$ scattering through the non-Abelian nature of the electroweak theory.

the anti-quarks), while an eightfold representation can combine all colour/anti-colour charge doublets, giving rise to eight different gluons.

However, as the "colourless" states (either the meson with a quark/antiquark couple carrying the same colour/anti-colour, or the baryon with three quarks having all three colours or anti-colours combined in a bound state such as the proton) are the only physical objects observed so far in nature, the confinement of these coloured quarks in colourless hadrons is assumed.

All possible interactions are described through a combination of global (independent from any space-time coordinate choice) and local symmetries defining their inner rules. The SM is combining both the $SU(2) \times U(1)$ symmetry of the electroweak sector formulated by Glashow, Salam and Weinberg in the 1960s, and the QCD $SU(3)_C$ colour symmetry generated by this threefold colour charge defined above in the scope of the strong interaction.

In particular, if one restrains to the electroweak sector, one may notice the non-Abelian structure associated with this symmetry, through which pure bosonic interactions are predicted. One direct consequence of this property is the possible gauge-invariant tri- and quadrilinear couplings it allows. An example of such interactions is pictured in Fig. 1.5 for the fourfold interactions between two photons and two $W^\pm$ gauge bosons, in which both the triple (*s*- and *t*-channels) and quartic gauge couplings are predicted to contribute to the full amplitude at the tree level.

As mentioned in the last sections, the half-integer spin category, or *fermions*, is defining the matter's building blocks. In this division, one finds the leptons (with their associated neutrinos) and the quarks. These two categories are furthermore replicated to form three families only distinguished by their masses hierarchy. For instance, in the lepton sector, the electron, the muon and the tau families are characterised by an approximate mass hierarchy 1:200:3500. An non-exhaustive list of properties characterising these fermions is given on table 1.1.

Family	(Anti)matter components							
		electron		electron neutrino		up		down
I	$e^{\mp}$	0.511×10^{-3}	ν_e	$< 0.45 \times 10^{-6}$	u	0.0023	d	0.0048
		∓ 1		0		$\pm 2/3$		$\mp 1/3$
		muon		muon neutrino		charm		strange
II	$\mu^{\mp}$	0.105658	ν_μ	< 0.00019	c	1.275(25)	s	0.095
		∓ 1		0		$\pm 2/3$		$\mp 1/3$
		tau		tau neutrino		top		bottom
III	$\tau^{\mp}$	1.77682(16)	ν_τ	< 0.0182	t	173.21(87)	b	4.18(3)
		∓ 1		0		$\pm 2/3$		$\mp 1/3$
	Leptons				*Quarks*			
	Fermions							

Table 1.1: The fermion sector of the standard model, describing all building blocks of the matter. Beside the particle symbols the mass (in GeV) and electrical charge (in units of $e = 1.602 \times 10^{-19}$ C) are given from [11].

Moreover, the integer spin case defining the *boson* class is composed of particles mediating an interaction. These force carriers are the *photon* γ for the electromagnetism, the $W^{\pm}$ and the Z bosons for the weak force, and the eight gluons g for the strong interaction. A listing of several properties characterising these particles is shown on table 1.2.

A full conservation of the non-Abelian $SU(2)$ symmetry in the weak sector of the standard model would imply a massless set of physical intermediate fields, as described in [12]. However, one may notice that experimentally the weak interaction is characterised by its short range. Unlike the infinite range electromagnetism mediated by a massless field (the photon), the electroweak gauge bosons $W^{\pm}$ and Z are thus required to be massive. A *spontaneous breaking* of this custodial symmetry is therefore required.

Formally, following the *Goldstone theorem* described in details in [13], each spontaneous symmetry breaking involves the apparition of a new scalar field for each one of its generators. For instance, one may quote the pions for the breakdown of the fundamental QCD symmetry through quark confinement. In the electroweak case, this scalar field (the Brout-Englert-Higgs, or BEH field) is mediated by a boson, commonly named the *Higgs boson*. While predicted already in the 1960s, its experimental discovery through its numerous decay channels was only made possible in 2012 [14, 15]. Its properties are shown on table 1.2.

In the SM, the mass of the physical states of the weak gauge bosons (along with several other fermionic and bosonic fields, such as the leptons and quarks) is generated

Force carriers				Higgs sector	
Electroweak interaction		Strong interaction			
	photon		gluon		Higgs boson
γ	0	g	0	H	125.09(24)
	0		0		0
	W boson				
$W^{\pm}$	80.835(15)				
	± 1				
	Z boson				
Z	91.1876(21)				
	0				
Bosons				*Boson*	

Table 1.2: The boson sector of the standard model, defining all particles mediating an interaction. Beside the particle symbols the mass (in GeV) and electrical charge (in units of $e = 1.602 \times 10^{-19}$ C) are given, extracted from [11].

through their interaction with the BEH field. Thus, the intrinsic mass of these particles is directly proportional to the coupling of their field to this latter.

Going beyond the scope of this thesis, a broader description of this mechanism can be found elsewhere [16, 17].

1.1.2.1 *Dimensional analysis*

One may use a purely Lagrangian formalism to embed into a scalar functional, the action, the whole symmetry structure of the SM defined in the former section. In this scheme, any "beyond-the-standard model " (BSM) extension can be expressed as a set of additional terms to be embedded in the resulting Lagrangian density $\mathcal{L}$. This enables to formulate it as an infinite expansion in energy dimensions (effective Lagrangian approach):

$$\mathcal{L}^{\text{eff}}_{\text{BSM}} = \mathcal{L}^{(4)}_{\text{SM}} + \sum_{d=5}^{\infty} \frac{1}{\Lambda^{(d-4)}} \sum_{k} c_k^{(d)} O_k^{(d)} = \mathcal{L}^{(4)}_{\text{SM}} + O(\Lambda^{-1}), \tag{1.1}$$

where Λ is a typical energy scale at which new physics behaviours start to become noticeable.

Hence, two components define the total density:

- a renormalisable, "general" standard model Lagrangian (relying on order 2 and 4 operators only), and representing the full panel of interactions within the electroweak and strong forces,

- an infinite sum of higher order d-dimensional operators, the set of $O_k^{(d)}$ components with their associated coefficients $c_k^{(d)}$.

This infinite set of higher-dimensional operators can then be constrained by applying all symmetries observed in nature, either from experimental observations, or from basic postulates to the model. For instance, one can apply the conservation of lepton and baryon number as a mean to limit their multiplicity.

Nevertheless, this multiplicity of operators increases with the energy dimensional order considered in the expansion. If one restrains to the dimension-6 order operators in which both the lepton and the baryon numbers are conserved for instance, 59 operators are required to describe the full symmetry group [18].

One can furthermore restrict the multiplicity by selecting a particular (set of) initial and final state(s), and search for discrepancies in their experimental tests. In section 1.4.1 we will extract a batch of couplings of interests, probing multiple anomalous operators through several processes. In particular, in this thesis, the processes in which two photons are forming the initial state will be studied in details.

1.2 TWO-PHOTON FUSION PROCESSES

In this section, the two-photon production processes will be studied in details as a subset of the so-called *central exclusive processes* (CEP).

In a proton-proton colliding experiment such as the LHC defined hereafter (see Section 2.1), the exclusivity condition can be translated in a requirement to observe the full picture of the physical system created in the two-proton scattering, including both the two outgoing forward protons along with the central system.

In this thesis, the following notation will be used for these central exclusive events:

$$pp \to p^{(*)} X p^{(*)}$$

where X indicates any class of central system produced in the process, defined as the full final state with the exception of the outgoing states $p^{(*)}$ of the protons giving rise to the event.

Two possible outcomes can be observed with these outgoing protons:

- they remain intact in the final state (the "elastic" case, noted p),

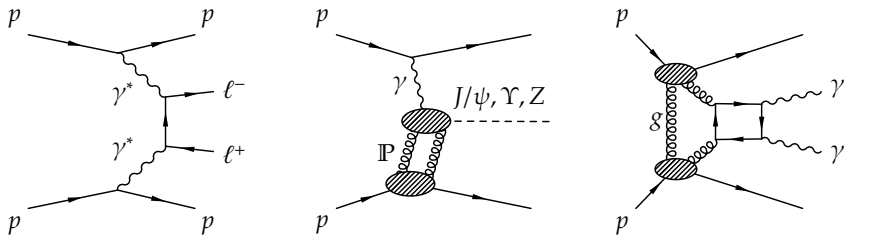

(a) Two-photon exchange process

(b) Photon-pomeron fusion (photoproduction)

(c) Double-pomeron exchange (DPE)

Figure 1.6: Examples of exclusive processes in proton-proton scatterings.

- the virtuality producing the central system reaches a high value, thus dissociating the proton in a shower of remnants (written as p^*).

Depending on the energy range of this loss, this latter case is often referred to as the *hadronisation* or *fragmentation* phenomenon. In this scenario, the colour-charged partons building the proton are given a sufficiently high virtuality to break the bound state. Therefore, freed from the strong confinement, the partons are emitted in a cone with an opening angle mainly determined by the total proton energy.

The CEPs are characterised by the exchange of a neutral colour-singlet (*i.e.* handling no electric nor colour charge) object carrying a momentum fraction ξ, hence with a 4-momentum $p \equiv \xi p_i$ (where p_i is the incoming proton's 4-momentum). The neutrality of the exchanged particles gives rise to a neutral central system (the sum of all centrally produced particles electrical charges is null). At first order, this intermediate object can either be a photon (including the purely electrodynamic coupling to the proton), or a pomeron.

The latter case, going beyond the scope of this work, is an artefact introduced in the 1960s to explain the steady rise of the hadron-hadron collisions cross section. In the QCD formalism, it can be pictured as a bound state of at least two gluons [19, 20], both to provide the momentum building the central system, and to cancel any colour flow in the exchange. It carries the same quantum numbers as the vacuum state [21].

For two types of intermediate particles, three different classes of events can be built. These classes are pictured in the Fig. 1.6. One may already emphasise the first diagram (Fig. 1.6a) representing the two-photon processes developed later in this text.

The two-photon ($\gamma\gamma$) interactions, as well as the two additional process types ($\gamma\mathbb{P}$, $\mathbb{P}\mathbb{P}$) are characterised by an equivalent set of properties, such as:

- a well-defined, clearly isolated central system,
- a large rapidity gap providing a separation between the central system X and the two outgoing protons (or remnants) $p^{(*)}$.

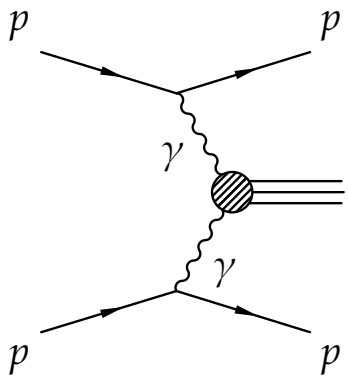

Figure 1.7: A generic two-photon process as observed in a hadron collider. The two incoming photons contribute to create a central system within a broad energy range.

This latter characteristic directly arises from the neutral and colourless type of exchange involved, thus preventing any hadronic activity in the mediating particle range.

At a proton-proton collider such as the LHC, the central exclusive processes are giving rise to a class of very clean events. They are usually contrasting with a higher central activity characterising deep-inelastic scattering processes more commonly studied in this energy range.

The general picture of the two-photon interactions studied here in a proton-proton colliding experiment is summarised in Fig. 1.7. Several physical observables are tightly bound to this class of processes. To quote a few:

- the rate of production and the kinematic distribution associated to both incoming photons, characterised by the so-called *photon fluxes*,
- the "hard", central two-photon process cross section, which can be indirectly studied as a probe of its theoretical predictions,
- the scattered protons status and kinematics, highly dependant on the kinematics of the intermediate photons.

Many topics in HEP rely in the study of two-photon interactions. One can quote for instance the direct experimental probe of SM couplings through the search for $\gamma\gamma \to \gamma\gamma$ processes [22] (where the SM contribution is of of $O(\alpha^4)$ and involves an inner charged fermion or a boson box), the search for gravitons [23] or extra dimensions [24, 25], the two-photon production of super-symmetric particles candidate [26], the central exclusive Higgs boson photo-production [27, 28], or the quantum electrodynamics

(QED) productions of leptons and gauge bosons pairs. This latter category will be studied in details in sections 1.3 and 1.4. Therefore, an accurate modelling of these processes is a strong requirement at LHC energy scales.

In this chapter, both the low- and high photon virtualities will be covered. In the first part, the formalism of a widely used approximation relying on the low values of these virtualities will be introduced. Then, the high-Q^2 limit will be studied through one of the most direct and cleanest two-photon process, the lepton pair production.

1.2.1 *Equivalent photon approximation*

In the scope of a pp collider such as the LHC, the theoretical evaluation of a total production cross section for a two-photon generated process can be hasardous, given the virtuality range reachable by the intermediate photons.

One may therefore need to introduce a computational technique to quote a total cross section, given its central $\gamma\gamma \to X$ process. Among these methods, one finds the *equivalent photon approximation* (EPA).

A way to introduce this technique is to picture the coupling of photons with a high-energy, charged particle using a simplified view. Indeed, one can remember that in a classical view the electric and magnetic components of the electromagnetic field surrounding a highly-boosted particle are approximately orthogonal to its direction.

Hence, the first approximation introduced by von Weizsäcker and Williams [29, 30] in the 1930s, and named after them, supposes that all radiations have a polarisation vector contained in a plane orthogonal to the particle's direction. Therefore, this postulates that these photons are produced close to their mass shell, with a minimal scattering angle with respect to the initial particle.

This approximation allows to write the photon flux (at a given photon energy ω) as a function of the photon energy density $\mathrm{d}U$ using a pure classical electrodynamics formalism:

$$\mathrm{d}n_{\omega}^{\mathrm{class}} = \frac{\mathrm{d}U(\omega)}{\hbar\omega} \simeq \frac{e^2}{\hbar c}\frac{\mathrm{d}\omega}{\omega},$$

with e the fundamental (electron) charge, $\hbar$ the normalised Planck constant, and c the speed of light in vacuum. In this scope, one may introduce a simplified, natural units system in which $\hbar = c = 1$, widely used in HEP.

This model was furthermore extended decades after by Budnev *et al.* [31], in an attempt to simplify the expression of any two-photon produced system using a limited number of assumptions. The first goal of these developments was to study the two-photon production of hadrons using electron-positron colliders, but it soon became an essential framework in many processes, for many incoming (primary) particles.

The first postulate is that the photon virtuality should be low enough for any longitudinal photon polarisation effects on the produced system to remain negligible.

The photons are therefore supposed to be real, and produced collinearly to the incoming beam momentum (hence, no transverse component is expected for the central system).

In this scheme, one can compute the total production rate for any (real) photon-induced process using a convolution of its "hard" central component, and the integrated photon fluxes. The simplest case is the photo-production, in which one single flux is convoluted to the central system (the second incoming particle being the second proton's parton $\hat{p}$):

$$\mathrm{d}\sigma(pp \to p^{(*)}(\gamma\hat{p} \to X)p^{(*)}) = \mathrm{d}\hat{\sigma}(\gamma_\omega\hat{p} \to X) \otimes \mathrm{d}n_\omega.$$

In the two-photon case, one may use the two fluxes $\mathrm{d}n_{\omega_{1,2}}$ to obtain:

$$\mathrm{d}\sigma(pp \to p^{(*)}(\gamma\gamma \to X)p^{(*)}) = \mathrm{d}\hat{\sigma}(\gamma_{\omega_1}\gamma_{\omega_2} \to X) \otimes \mathrm{d}n_{\omega_1} \otimes \mathrm{d}n_{\omega_2}. \tag{1.2}$$

These integrated photon fluxes are defined using the scale-dependant electric and magnetic form factors F_E and F_M of the incoming particle emitting the photon in the process:

$$\mathrm{d}^{(2)}n_\omega = \frac{\alpha}{\pi}\frac{\mathrm{d}\omega}{\omega}\frac{\mathrm{d}Q^2}{Q^2}\left\{\left(1-\frac{\omega}{E_i}\right)\left(1-\frac{Q^2_{\mathrm{min}}}{Q^2}\right)F_E(Q^2) + \frac{\omega^2}{2E_i^2}F_M(Q^2)\right\}, \tag{1.3}$$

with E_i the incoming beam particle energy, and Q_{min} the minimal energy transfer to the photon, defined as:

$$Q^2_{\mathrm{min}} \equiv Q^2_{\mathrm{min}}(\omega) \simeq \frac{m_i^2\omega^2}{E_i^2 - \omega E_i} = \frac{m_i^2\xi^2}{1-\xi},$$

with m_i the incoming particle's mass, and $\xi = \omega/E_i$ the photon's fraction of the incoming particle energy (also called *Feynman x*). This expression is furthermore integrated over the full available virtuality range Q^2, to provide the total photon flux (given an upper limit to this squared momentum transfer, Q^2_{max}, set as a free parameter in this approximation):

$$f_\gamma(\xi) = \int_{Q^2_{\mathrm{min}}}^{Q^2_{\mathrm{max}}} \mathrm{d}Q^2 \frac{\mathrm{d}^2 n_\omega}{\mathrm{d}\xi \mathrm{d}Q^2}. \tag{1.4}$$

One can notice that the flux at this stage is only dependent to the incoming particle nature through its mass, and the electromagnetic F_E and F_M components in Eq. (1.3).

These latter two can either quote the purely elastic flux, as predicted by an electromagnetic treatment of both the parameters, or introduce the inelastic component, using a parameterised description extracted from a fit to their experimental values (the so-called *structure functions*). Furthermore, in the elastic photon scattering scenario, *i.e.* for $x_{\mathrm{Bj}} \to 1$, the differential photon flux (1.3) may be simplified if one assumes no difference between the incoming and the outgoing beam particles' mass. This elastic flux can therefore be integrated over the allowed range of ω with this additional

constraint, thus one obtains $\mathrm{d}n_\omega \sim \mathrm{d}Q^2/Q^2$ only.

In the following parts of this text, the emphasis will be put on the protons as incoming particles case. There, the two elastic form factors are directly related to the two *Sachs factors* [32] G_E and G_M (whose values are precisely known experimentally), respectively defining the distribution of the proton charge and its magnetisation current. A linear combination is given by:

$$F_E^{(\mathrm{el})}(Q^2) = \frac{4m_i^2 G_E^2(Q^2) + Q^2 G_M^2(Q^2)}{4m_i^2 + Q^2}, \quad F_M^{(\mathrm{el})}(Q^2) = G_M^2(Q^2). \tag{1.5}$$

One can parameterise these two form factors through the dipole approximation introduced in [33, 34]:

$$G_E(Q^2) = \left(1 + \frac{Q^2}{0.71\ \mathrm{GeV}^2}\right)^{-2}, \quad G_M(Q^2) = 2.79 \cdot G_E(Q^2),$$

where the normalisation scale applied to the squared momentum transfer Q^2 is extracted from an experimental scan over this parameter, and the constant relating the electric and magnetic parts is the proton magnetic moment μ_p. This formulation of the elastic photon flux enables to see that the low-Q^2 transfers are expected to contribute the most to the total cross section, while the larger transfers are mostly suppressed in such purely elastic scatterings.

The dissociative case is slightly more challenging to estimate, relying on the local structure of the proton, and probed in the scope of DIS experiments.

One may use the formalism of the *structure functions*, providing an energy-dependent picture of the quark and gluon composition of the incoming beam particle. These are directly linked to the parton distribution functions introduced earlier in this chapter, given any external transfer of energy Q^2 applied to the nucleon.

In the particular case of the proton, two of these structure functions can be isolated: F_1 and F_2, describing the electric charge distribution inside the proton. Several linear combinations of these two parameters were introduced in the literature, following the pace of experimental observations.

A special attention may be drawn to the latter structure function F_2, for the characterisation of the inelastic photon flux. If one leaves aside higher order perturbations in α_s, the direct relation between its formalism and the various quark (resp. anti-quark) PDFs q_f (resp. $\bar{q}_f$) inside this nucleon is given by:

$$F_2(x_{\mathrm{Bj}}, Q^2) = x_{\mathrm{Bj}} \sum_f e_f^2 \left\{ q_f(x_{\mathrm{Bj}}, Q^2) + \bar{q}_f(x_{\mathrm{Bj}}, Q^2) \right\},$$

with e_f being the parton electric charge.

As a mean to compute the inelastic photon flux, one may integrate the single F_2 structure function over its full virtuality range:

$$F_E^{(\text{inel})}(Q^2) = \int \frac{\mathrm{d}x_{\text{Bj}}}{x_{\text{Bj}}} F_2(Q^2, x_{\text{Bj}}), \quad F_M^{(\text{inel})}(Q^2) = \int \frac{\mathrm{d}x_{\text{Bj}}}{x_{\text{Bj}}^3} F_2(Q^2, x_{\text{Bj}}).$$

Given the determination of the photon fluxes $f_\gamma(x)$ through (1.4), any two-photon produced cross section can be computed using a rewritten form of (1.2):

$$\sigma_{pp\to p^{(*)}Xp^{(*)}} = \int_{w_0}^{\sqrt{s}} \mathrm{d}w_{\gamma\gamma} \frac{\mathrm{d}\mathcal{L}_{\gamma\gamma}}{\mathrm{d}w_{\gamma\gamma}} \sigma_{\gamma\gamma\to X}(w_{\gamma\gamma}), \tag{1.6}$$

with w_0 the minimal two-photon centre of mass energy allowed by the full process kinematics, and the relative two-photon luminosity spectrum as defined in [35]:

$$\frac{\mathrm{d}\mathcal{L}_{\gamma\gamma}}{\mathrm{d}w_{\gamma\gamma}} = \int_{w_{\gamma\gamma}^2/s}^1 \mathrm{d}x \frac{2}{xs} w_{\gamma\gamma} f_\gamma(x) f_\gamma\left(\frac{w_{\gamma\gamma}^2}{xs}\right).$$

This latter quantity acts as a general convolution factor to the overall production cross section as described in (1.6). One can see that its formulation is left as general as possible, depending only on the form factors $F_{E,M}(Q^2)$. This allows this EPA to be used in a large panel of production mechanisms for the two incoming photon fluxes, including proton-proton, or heavy-ion-induced photo-productions [36].

One can find a numerical estimation of this convolution factor in Fig. 1.8 for 3.5 TeV protons. This figure uses a F_2 parameterisation extracted from *ep* collisions (probing the $\gamma^* p$ interactions) at HERA, as quoted in [37].

1.2.2 *Gap survival probability, and re-scattering effects*

As seen earlier in this section, the phenomenology of central exclusive processes relies on the exchange of two colourless objects by the beam particles to create the central system. An interesting observational feature of this colourless exchange is the significant rapidity gap it predicts between the central system and the scattered protons, thus a large region in which no particle activity is expected.

However, with the increase of the energy transfer Q^2, the probability for the production of particles inside this gap through secondary, higher order processes, rises as well. This behaviour arises from the geometrical argument introduced earlier, if one recalls that this energy transfer is inversely related to an effective impact parameter b of the incoming particles scattering, *i.e.* $Q^2 \sim 1/b^2$.

In that scope, the more virtuality exchanged by the primary particles, the shorter the distance of approach. This can lead to secondary effects altering the theoretical

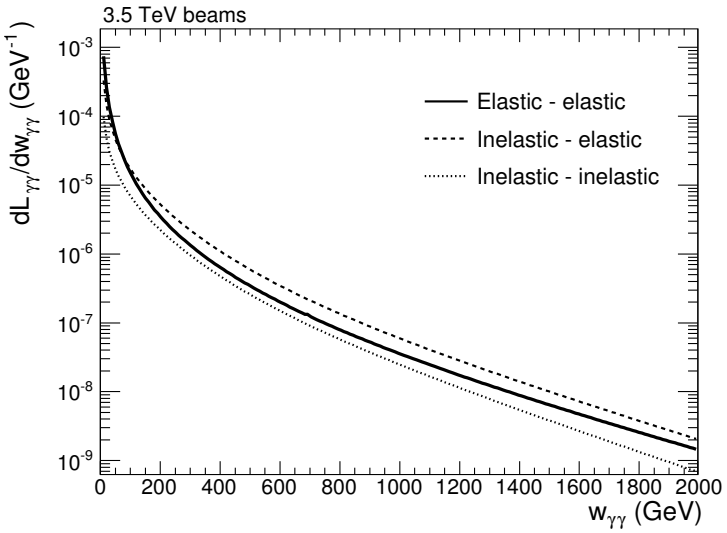

Figure 1.8: Integrated photon flux as given by the equivalent photon approximation, for the elastic, the single- and the double-dissociative proton case. The elastic contribution is simulated using a maximal momentum transfer $Q^2_{\text{max}} = 2$ GeV^2, while the dissociative cases use $Q^2_{\text{max}} = 300$ GeV^2. Figure extracted from [38].

prediction of the central process, and a partial or full suppression of the rapidity gaps to be observed in these processes. For instance, strong interactions can occur between the partonic and central states, or between the two beam remnants, thus modifying the dynamics of the outgoing partons and potentially creating showers of secondary particles inside the gaps regions. These corrections are commonly referred to *rescattering effects*.

On the contrary, the low virtualities exchanged in elastic scatterings are equivalent to a large impact parameter where the central system is expected to be produced at rest. For instance in the elastic two-photon production of lepton pairs described above, this corresponds to a central system where both leptons are emitted back to back.

Formally, if one returns to the larger Q^2 scales, one can introduce the survival factor S^2 parameter to account for all these prediction tensions in the theoretical computation of the matrix element describing a process. This factor corresponds to a probability, in a given energy range, to observe a rapidity gap in this class of events.

Furthermore, this probability is process-dependant through the allowed energy range the two protons can carry, strongly determining the secondary interaction rate. In the photon-pomeron or two-pomeron exchanges, this formalism is more complex to evaluate (the gluon components being also able to self-interact), and is generalised in

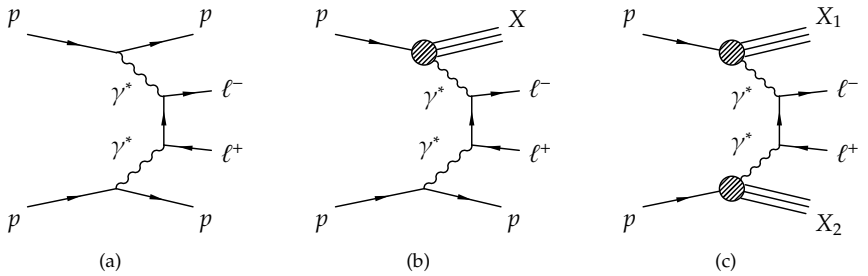

Figure 1.9: Beithe-Heitler-like process describing the exclusive two-photon production of lepton pairs, (a) where the two protons are left intact, *i.e.* elastic events, (b) where one proton dissociates into a low-mass system X, and (c) where both protons dissociate into the hadronic systems X_1 and X_2.

the scope of *Sudakov form factors*. A general description of this theoretical interpretation can be found in [39–42].

Therefore, the overall S^2 needs to be quantified for every single central exclusive reaction, either computed from the complex phenomenology of secondary exchanges, or extracted from the experimental probe of such processes.

1.3 DILEPTON TWO-PHOTON PRODUCTION

In the jungle of proton-proton scatterings, the two-photon production of a lepton pair enables an observation of the most straightforward set of events by the simplicity of its final state (two opposite-charge, high quality leptons produced along with the rapidity gap introduced earlier).

As no additional soft or hard central jets are expected, an almost "empty" central detector is ensured. The only sources of secondary activity are either the highly boosted showers expected in the very forward region (if the proton is fragmented after its interaction), or the multiple interactions to be expected in the high-rate LHC experiments.

This type of events constitutes a "standard candle" to probe and improve the knowledge about the experimental apparatus as well as provide a high statistics class of photon-induced events for further studies.

In recent history it was therefore proposed as a "golden" channel to evaluate the collision rate and machine parameters for any collider able to produce it, such as the LHC described in this thesis. The main reason is the position the elastic contribution (shown in Fig. 1.9a) occupies, being one of the most well-predicted theoretical quantities reachable theoretically in a hadron collider experiment.

However, due to the very low mass of its produced system, the simple EPA defined above cannot be used for its wide virtuality range. Thus, in order to compare

the experimental observations to a theoretical prediction of a cross section for the $pp \to p^{(*)}(\gamma\gamma \to \ell^+\ell^-)p^{(*)}$ process, a Monte Carlo (MC) generator including the full matrix element of the reaction, and developed prior to the HERA physics programme has been intensely used during the last decades: `LPAIR`.

1.3.1 *Full matrix element: the `LPAIR` generator*

Designed during the early 1980s, *i.e.* a decade before the ZEUS and H1 data taking periods at the HERA collider, `LPAIR` [43] is an event generator allowing to simulate the full $\gamma\gamma \to \ell^+\ell^-$ reaction in a fully-embedded piece of code. It uses a full $2 \to 4$ matrix element for this process developed by J. Vermaseren [44] to quote a cross section and generate events in a given subset of the phase space.

This matrix element formalism enables to provide an accurate description of both the elastic and dissociative component of the possible final states. The incoming particles can either be the *ep* couple used at HERA, or *ee*, or *pp*. The outgoing state is therefore defined as the central dilepton system produced, along with the outgoing beam particles. While the *ee* case is leading to a trivial expression of the form factors, the proton-induced reactions can produce three different outcomes (listed in increasing order of Q^2 energy transfers):

- a fully-elastic scattering, as previously described, where the outgoing proton is kept intact (with a small energy loss),
- an intermediate, dissociative behaviour, in which the continuum predicted by inelastic proton structure functions at "large" Q^2 (above $2-3$ GeV^2) is parameterised, along with contributions from the production of low-energy resonances, thus leaving enough phase space for the outgoing proton to fragment,
- a fully-inelastic scattering, where the energy transfer is sufficiently high to use the full partonic content of the proton to extract the photon flux. The outgoing proton is therefore fragmented in the final state.

In this thesis, all three contributions were studied. Nevertheless, the emphasis was set on the latter two components, hereafter referred to *dissociative* contributions, most sensitive to the choice of parameterisation used in the evaluation of the photon flux.

For the elastic (or *coherent*) proton case, the elastic form factors quoted in section 1.2.1 are used to compute an unintegrated photon flux. The dissociative (or inelastic) proton case relies on the introduction of a set of proton structure functions, providing a characterisation of the photon fluxes for the energy range considered. In its default *pp* behaviour, `LPAIR` is relying on the *Suri-Yennie* (SY) parameterisation[2] for this component. It enables to access both the low-photon's virtuality ranges ($Q^2 < 10$ GeV^2) from numerous fits performed in low-mass resonances regions with γp data collected in *ep* collisions, along with a continuum part parameterised at higher virtualities.

[2] A detailed description of these structure functions can be found in [45].

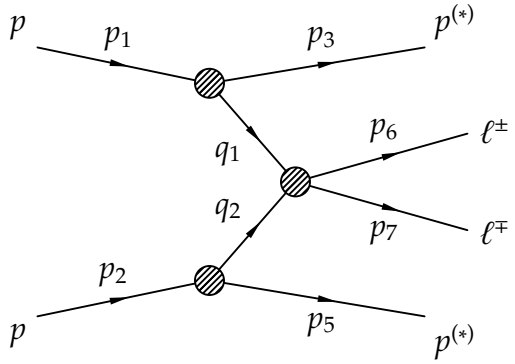

Figure 1.10: LPAIR definition of the kinematic quantities associated to all particles involved in the $\gamma\gamma \to \ell^+\ell^-$ events.

To be modular for the end-user, other choices of structure functions were implemented during the long history of this generator. For instance, the fully-inelastic scattering described above can also be simulated using the PDFs provided by the common PDFLIB library as an input [46].

The full amplitude, following the kinematics of Fig. 1.10, is directly proportional to $1/q_1^2 q_2^2$. Therefore, the very low photon virtualities expected in the elastic limit are expected to give important contributions to the total cross section. This introduces tight computational requirements on numerous parts of the code, thus a carefully selected set of integration variables was implemented. Among these optimisations, one can quote the larger numerical stability reached for the very low-Q^2 values of the phase space once all ($\mathrm{d}Q^2/Q^2$) are replaced by their counterparts $\mathrm{d}(\ln Q^2)$, or a rescaling of several numerically unstable quantities crucial in the full matrix element computation.

The outgoing proton remnants are then separated into their quark-diquark contents, and propagated to a string fragmentation algorithm such as Jetset [47]. This latter step provides, given any proton remnants kinematics, a collection of colourless particles expected in the full final state after several iterations of hadronisation/fragmentation.

This 4-decade old software, despite its rather complicated structure ensuring a high numerical stability, is still providing an accurate description of the elastic phase space in LHC energies. Therefore, a newer version of LPAIR was developed in an attempt to settle the common grounds of this piece of software, while easing its manipulation within the steadily increasing community of C++ developers. As described in Appendix A the structure of this code allows the simulation of multiple exclusive processes, with a matrix element factorised out of the cross section computation and events simulation components.

1.3.2 *The k_T-factorisation approach*

A very widely used way of extracting a proper description of the $pp \to p(\gamma\gamma \to X)p$ process relies on a simplified formulation of its matrix element. The strategy is similar to the ones developed in the previous sections: use the incoming photon fluxes as a kinematic quantity of interest to factorise the full matrix element into simpler building blocks which can be handled individually.

The elastic photon fluxes are expressed as a function of the proton's form factors G_E and G_M, while the inelastic contributions are relying on an unintegrated composition of its structure function (as for the approach used in `LPAIR`, as described above, and unlike the EPA integrating these fluxes over their full x_{Bj} range).

One can define the *k_T-factorisation approach* as the deconvolution through the emitted soft photons' transverse momenta $\mathbf{q}_{\mathrm{T}_{1,2}}^2$. In this scheme developed in details in [48], the two photon virtualities are given by:

$$Q_1^2 \equiv -q_1^2 = \frac{1}{\alpha_1}\left\{\mathbf{q}_{\mathrm{T}1}^2 + \alpha_1(M_X^2 - m_{i,1}^2) + \alpha_1^2 m_{i,1}^2\right\},$$
$$Q_2^2 \equiv -q_2^2 = \frac{1}{\beta_2}\left\{\mathbf{q}_{\mathrm{T}2}^2 + \beta_2(M_Y^2 - m_{i,2}^2) + \beta_2^2 m_{i,2}^2\right\},$$

with $m_{i,1/2}, M_{X/Y}$ the mass of the incoming and outgoing protons (or outgoing proton remnants). The α_i, β_i are the coordinates of these two photon virtualities in the coordinates system formed by a light-like composition of the incoming particles momenta (the so-called *Sudakov decomposition* [49]). Therefore, the virtualities are only expressed through their squared transverse component, the incoming particles' kinematics, and their outgoing remnant masses.

In the k_T-factorisation approach, the total matrix element of the generic $2 \to 4$, two-photon process can hence be approximated by:

$$\begin{aligned}\mathrm{d}\sigma(pp \to p(\gamma\gamma \to \ell\ell)p) = \frac{1}{\pi^2}\int \frac{\mathrm{d}^2\mathbf{q}_{\mathrm{T}1}^2}{\mathbf{q}_{\mathrm{T}1}^2}\frac{\mathrm{d}^2\mathbf{q}_{\mathrm{T}2}^2}{\mathbf{q}_{\mathrm{T}2}^2}\mathcal{F}^{(\mathrm{el,diss})}(x_{\mathrm{Bj}1}, \mathbf{q}_{\mathrm{T}1}^2) \times \\ \times \mathcal{F}^{(\mathrm{el,diss})}(x_{\mathrm{Bj}2}, \mathbf{q}_{\mathrm{T}2}^2) \times \\ \times \mathrm{d}\sigma^*(p_6, p_7, \mathbf{q}_{\mathrm{T}1}, \mathbf{q}_{\mathrm{T}2})\end{aligned} \tag{1.7}$$

with the same kinematics as defined in `LPAIR`, and pictured in Fig. 1.10 (*i.e.* the $p_{6,7}$ are representing the outgoing leptons' 4-momenta). In this scheme, the soft photon emissions leading to an elastic or inelastic treatment of the outgoing protons are expressed through the unintegrated photon fluxes $\mathcal{F}^{(\mathrm{el,diss})}$.

One may again emphasise that this combination is strictly comparable to the EPA formulation as derived in section 1.2.1, with the major difference that it leaves these

photon virtualities unintegrated in the overall flux. Therefore, in the k_T-factorisation, the transverse components of these virtualities are not neglected anymore.

Given these considerations, three matrix elements are extracted for all three possible sub-processes. These can be expressed in terms of a set of variables to be integrated over the whole phase space through a simple piece of software.

Considering the steady evolution of the implicit numerical precision provided by any commercial computer during the last decades, these variables were chosen to reflect physical quantities, such as $\mathbf{q}_{T1,2}$, the two incoming photons' transverse 2-momenta, their rapidity, or the dilepton transverse momentum difference. For the single- and double-dissociative cases, respectively one and two additional variable(s) are added, as for `LPAIR`: the one or two outgoing protons' invariant mass.

Following this recipe, an events generator was developed to provide a simplified alternative for the simulation of the two-photon production of lepton process. As stated, it consists in a full integrator to extract a physical value of the cross sections, given any constraints applied on the total phase space. Like `LPAIR`, its name reflects the process to be simulated, `pptoll` [50]. It also relies on the `VEGAS` stratified sampling algorithm [51] to perform the multi-dimensional integration in an efficient and coherent way.

This code is validated through the comparison of a set of observables accessible in LHC experiments, with `LPAIR`'s predictions. Two subsets of kinematic cuts are chosen to reflect the sensitivity reached in these experiments, namely an lower cut on the single outgoing leptons' transverse momenta at 3 (*soft* cut) and 15 GeV (*hard* cut). Also, two low- and medium-ranged parameterisation of the proton structure functions are introduced in `LPAIR`, and tested against `pptoll`:

- the *Suri-Yennie* structure functions [45] previously introduced, and based on an interpolation of low-virtuality observations ($Q^2 < 2 - 3$ GeV^2) of low-energy γp interactions observed in low-mass resonances regions in a range $\sqrt{s} = 1.11 - 18.03$ GeV, and

- the more recent *Szczurek-Uleshchenko* parameterisation [52] (SU) (also used in the k_T-factorisation approach), including contributions arising from much higher momentum transfers (up to the order of 100 GeV^2), and based on additional fixed targets (SLAC, NMC, E665, BCDMS), or collision (H1) data observations.

The x_{Bj} dependence on F_2 is shown for these two parameterisations at a given value $Q^2 = 2.5$ GeV^2, along with two other fits commonly used in this kinematic range, is shown in Fig. 1.11.

As shown on the upper two plots, despite its advanced age, the SY parameterisation reasonably averages the resonance structure observed at low Q^2, with the exception of low-x_{Bj} values (bottom plot, with a logarithmic scale of x_{Bj}). However, if one computes the x_{Bj} distribution for the $\gamma\gamma \to \ell^+\ell^-$ process using the `LPAIR` generator (as displayed

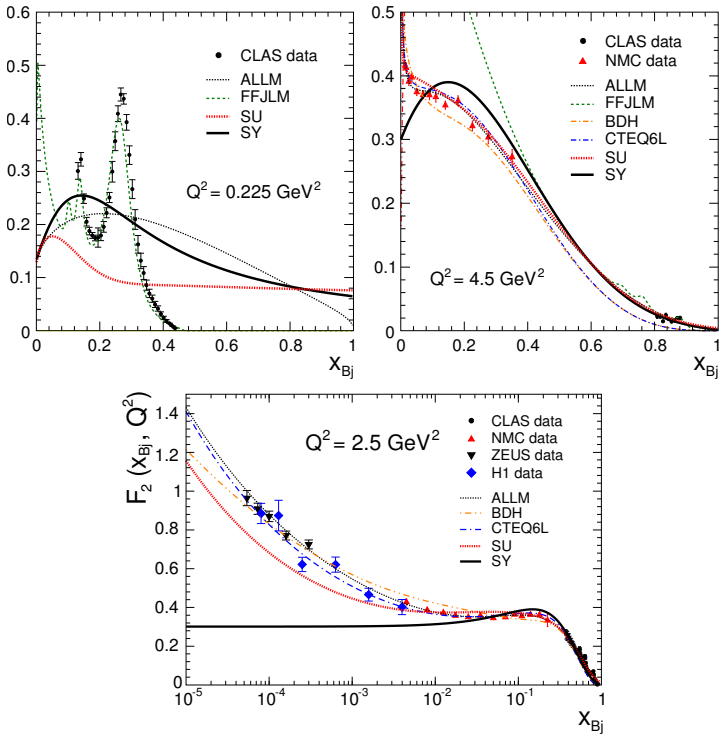

Figure 1.11: Comparison between the parameterisations of F_2 as a function of the x_{Bj} scale for multiple values of Q^2, and for several choices of evolution models. The SY behaviour at low-x_{Bj} is emphasised on the bottom figure, using a logarithmic scale of the x_{Bj} value. Figure extracted from [53].

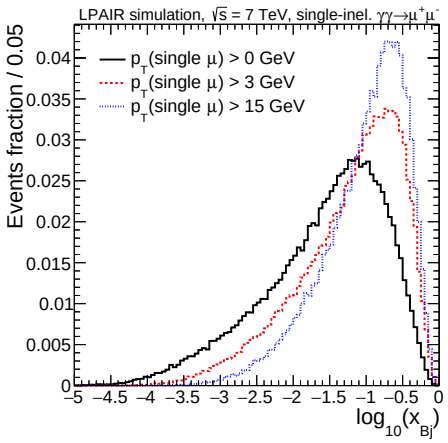

Figure 1.12: Comparison of the x_{Bj} distributions for multiple single lepton transverse momenta, as computed by LPAIR for the single-inelastic $\gamma\gamma \to \mu^+\mu^-$ process at $\sqrt{s} = 7$ TeV. The following cuts are applied on these distributions: $1.07 = m_p + m_{\pi^0} < M_X < 10^3$ GeV, $0 < Q^2 < 10^4$ GeV^2.

in Fig. 1.12), the lower values of this kinematic quantity are found not to stand below $10^{-3} - 10^{-4}$, depending on the lower cut imposed on the outgoing leptons' transverse momentum. One may therefore consider the SY as a good candidate for the modelling of the low-Q^2 ranges of the total dissociative cross section.

A comparison of the generation cross section for the two minimal single muon transverse momenta listed above is shown on table 1.3. The last column corresponds to the cross sections evaluated using a third set of PDFs, the Fiore *et al.* parameterisation [54] (FFJLM), only implemented in `pptoll`. To reflect the behaviour expected in LHC experiments, three fiducial cuts were used in this computation: $\left|\eta(\mu)\right| < 2.5$, $0 < M_X < 10^3$ GeV, and $0 < Q^2 < 10^4$ GeV^2. Above the harder p_{T} cut, one observes a good agreement between both the generators, and for all structure functions. However, at the lower value of this cut (3 GeV), the SY modelling implemented in LPAIR gives a slightly higher yield.

The following differential distributions consider the single-dissociative part of the process, in which one proton remains intact in the forward region and the other is fragmented in the final state.

The modelling dependence is clearly visible in the Q^2 (dissociative proton side) comparison shown in Fig. 1.13. Indeed, the SY is giving a slightly larger contribution to the lower values of this parameter.

However, despite the reasonable agreement observed for the p_{T} distribution, the single lepton kinematics comparison in Fig. 1.14 starts to display some tensions between

	Generator level cross section (pb)			
Generator	LPAIR		pptoll	
Struct. Function	SY	SU	SU	FFJLM
$p_T(\mu^\pm) > 3$ GeV	11.77	9.87	10.82	10.28
$p_T(\mu^\pm) > 15$ GeV	0.33	0.30	0.300	0.302

Table 1.3: Summary of generation cross sections (in pb) at $\sqrt{s} = 7$ TeV of the single-inelastic $\gamma\gamma \to \mu^+\mu^-$ process, for both the LPAIR and pptoll MC generators. Three structure functions are used, along with two lower values of the single muon transverse momentum. Table extracted from [48].

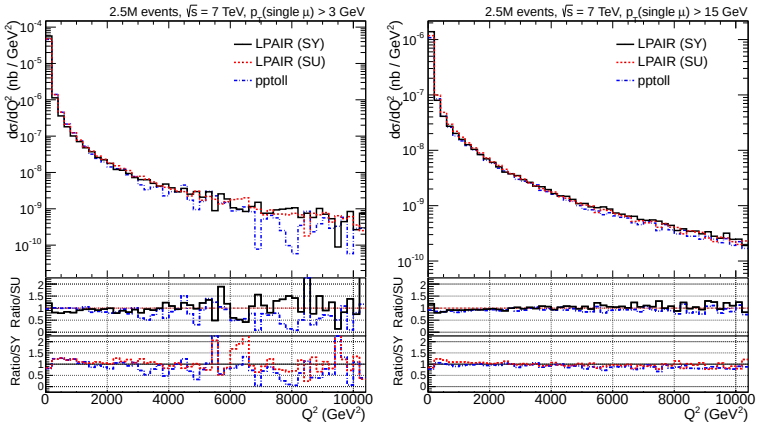

Figure 1.13: Comparison between the k_T-factorisation (pptoll) and the full matrix element (LPAIR) approaches for the photon virtuality Q^2 in the single-inelastic $\gamma\gamma \to \mu^+\mu^-$ process at $\sqrt{s} = 7$ TeV. The left (right) figure is for a lower single lepton transverse momentum cut of 3 GeV (15 GeV). Figures extracted from [48].

the two approaches. For instance, the single lepton η is shown to be incompatible between LPAIR and the k_T factorisation scheme, being sensitive to the choice of PDFs involved in the computation of the inelastic form factor. A fine experimental study of this distribution can therefore be triggered as a test of the dissociative modelling.

Still, if one returns to the dilepton system variables (for instance the dilepton invariant mass and transverse momentum, along with the acoplanarity $1 - |\Delta\phi/\pi|$ shown in Fig. 1.15), the agreement is mostly recovered in the full range.

Nevertheless, if the same F_2 parameterisations are used in both LPAIR and pptoll (such as the SU), this formulation of the total production cross section is providing a comparable description in the high-$p_T(\ell\ell)$ region of the total phase space. However, if the SY description is adequate for small Q^2 region (approximately $Q^2 < 10$ GeV^2), its extension to higher ranges is expected to give less sensitive results than the SU

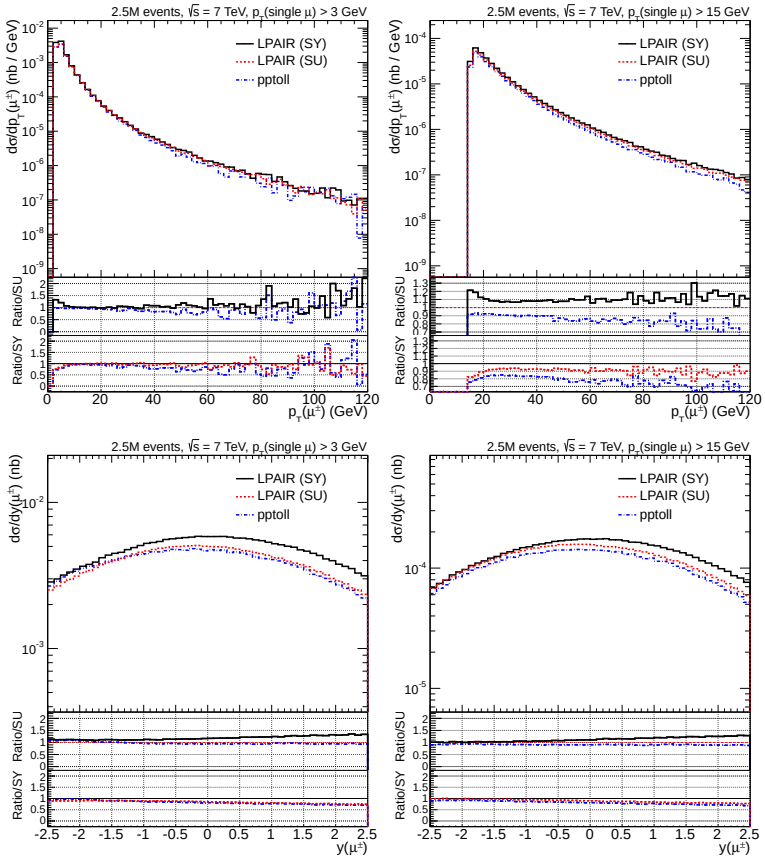

Figure 1.14: Comparison between the k_T-factorisation (`pptoll`) and the full matrix element (`LPAIR`) approaches for different single lepton kinematic distributions of interest in the single-inelastic $\gamma\gamma \to \mu^+\mu^-$ process at $\sqrt{s} = 7$ TeV. From top to bottom: single lepton transverse momentum, and rapidity. The left (right) figures are for a lower single lepton transverse momentum cut of 3 GeV (15 GeV). Figures extracted from [48].

parameterisation, which relies on F_2 and undergoes a special partonic treatment (through the DGLAP evolution equations, as described in details in [52, 53]).

Therefore, given its strong correlation to the overall Q^2 transfer in the system, the $p_T(\ell\ell)$ distribution provides a good test bench for the effects of the parameterisations to the observable final state. This correlation is shown in Fig. 1.16 for both the single- and double-dissociative proton scenarios.

Meanwhile, the overall compatibility observed between the two computations techniques allows the usage of the k_T-factorisation approach to treat the two-photon

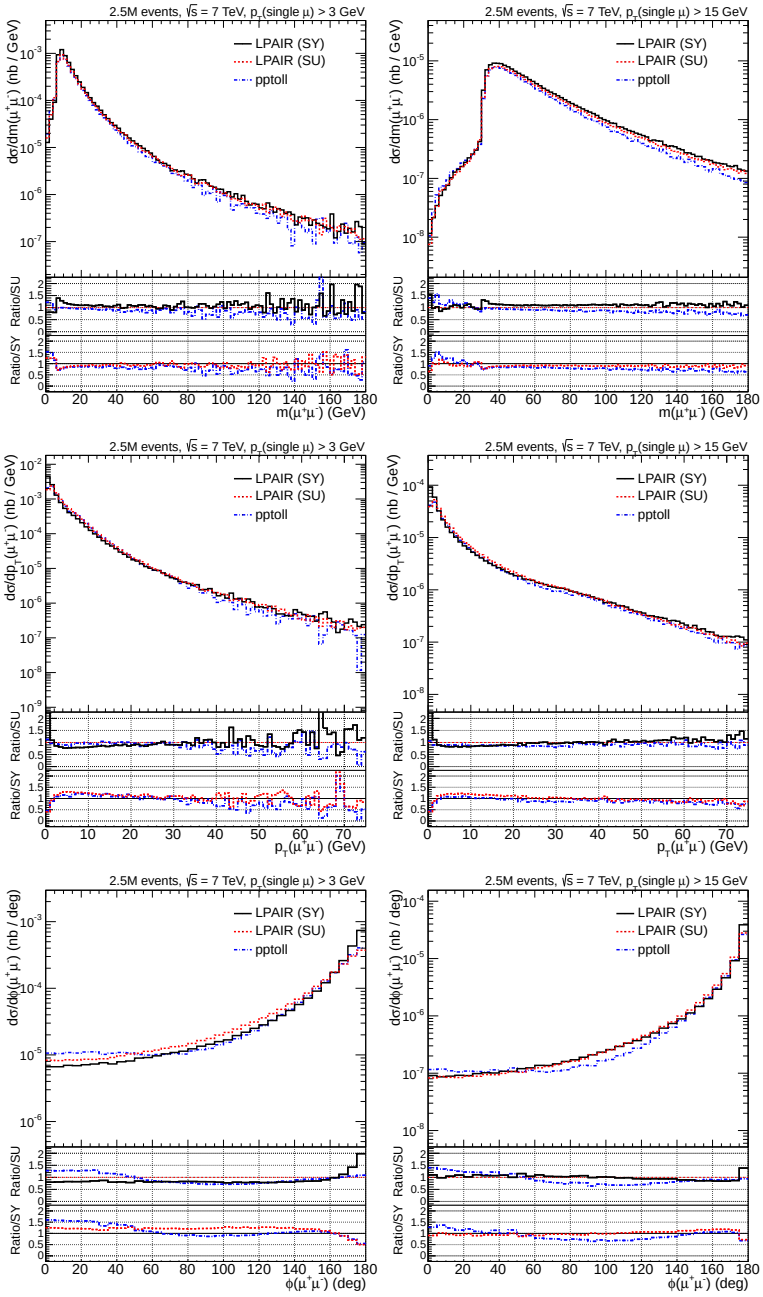

Figure 1.15: Comparison between the k_T-factorisation (`pptoll`) and the full matrix element (`LPAIR`) approaches for different lepton pair kinematic distributions of interest in the single-inelastic $\gamma\gamma \to \mu^+\mu^-$ process at $\sqrt{s} = 7$ TeV. From top to bottom: invariant mass, transverse momentum, and azimuthal angle difference in the transverse plane. The left (right) figures are for a lower single lepton transverse momentum cut of 3 GeV (15 GeV). Figures extracted from [48].

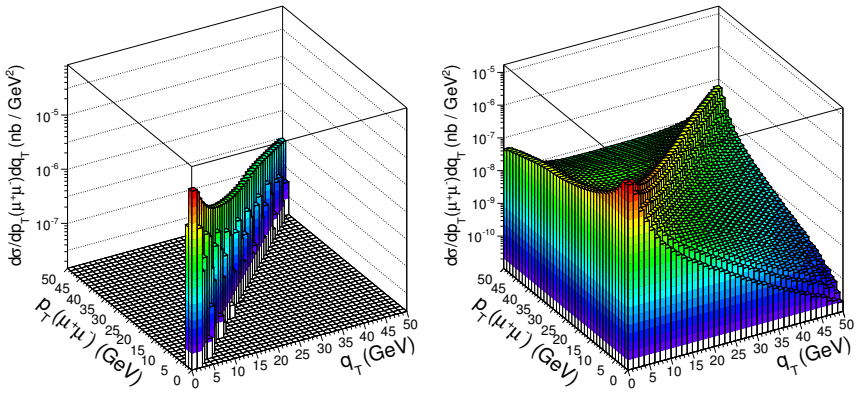

Figure 1.16: Correlation between the transverse momentum of the outgoing leptons pair and the transverse photon virtuality $q_T = |\mathbf{q}_T|$ (inelastic proton side) for the single- (left) and double-dissociative (right) cases. Simulations at $\sqrt{s} = 7$ TeV using the k_T factorisation approach implemented in `pptoll`. Figures extracted from [48].

production of a lepton pair. It also provides a good candidate for the implementation of the rescattering corrections and to test experimentally the effect of the two-photon energy scale to the proton structure, as well as for the simulation of other two-photon processes not modelled theoretically yet.

Therefore, if the $\gamma\gamma \to \ell^+\ell^-$ process was the only one studied in details through the k_T-factorisation treatment in this thesis, this technique enables to simulate other inclusive, or two-photon induced processes, giving rise to a broad spectrum of virtualities.

For instance, one can quote exotic predictions such as the two heavy charged exotic Higgs boson already mentioned earlier, and described in [28], or the potential implementation of this formalism in a simulation of the $\gamma\gamma \to VV$ process. This latter scenario would provide the first ever description of the whole $2 \to 4$ process kinematics, since all other predictions by modern generators are exclusively quoted using the integrated photon fluxes provided by the EPA.

Furthermore, it would allow to compute an overall cross section for all components involved in this particular process, including the non-elastic contributions neglected in the EPA.

1.4 TWO-PHOTON PRODUCTION OF GAUGE BOSON PAIRS

As introduced earlier in this chapter, the non-Abelian structure of the electroweak interaction allows the coupling between multiple gauge bosons to contribute to the total cross section of multiple processes involving these initial and final states. In

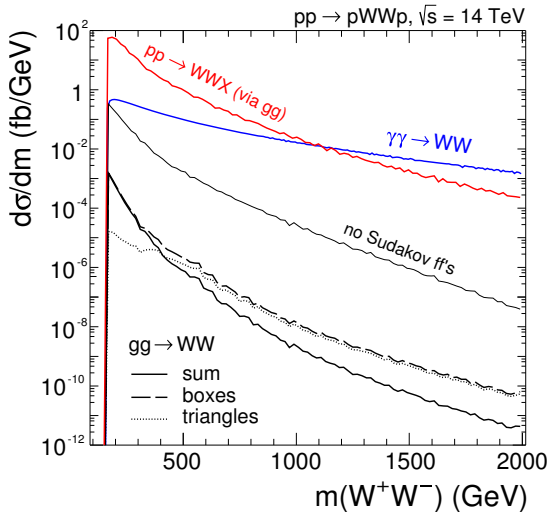

Figure 1.17: Differential cross section contributions to the $W^{\pm}$ pair production in pp collisions at $\sqrt{s}$ = 14 TeV. The inclusive and two-photon production processes are dominant in the whole invariant mass spectrum, while the diffractive contributions (with or without the Sudakov form factor suppression included), stands orders of magnitude below these. Figure extracted from [58].

particular, among this wide class of processes, a restricted set of couplings involving a two-photon initial state was considered: the $\gamma\gamma \to VV$ reactions, where the Vs are vector bosons. Therefore, this collection is composed of:

- the coupling between two photons and two $W^{\pm}$ gauge bosons [55–57], and
- the coupling between two photons and two Z bosons.

One may emphasise that none of these two reactions were observed experimentally prior to the LHC era.

Again, the SM provides the theoretical framework in which the expected absolute and relative magnitudes can be extracted for all sub-processes characterising this exchange.

Considering the first process, the inclusive signal is clearly expected to give its highest contribution through its multiple production channels. As shown in Fig. 1.17, this dominance in a pp collider environment is strictly correlated to the central system energy leading to the pair production. However, while the inclusive production through gluon exchange is expected to contribute the most at the low regime, the high invariant mass range is clearly dominated by the exclusive two-photon process.

The diffractive two-pomeron production, similar to the diagram shown in Fig. 1.6c, ranges orders of magnitude below these two contributions, ensuring the dominance of

the $\gamma\gamma \to W^+W^-$ process in a wide range of exclusive selections. One can also notice the effect of the Sudakov form factor through the large suppression expected in the whole range of energies. For the diffractive contribution, being sensitive to a larger spectrum of pomeron virtualities, this suppression decreases its prediction by $3-4$ orders of magnitude.

While the $\gamma\gamma W^+W^-$ coupling has a finite prediction within this standard model, the quartic $\gamma\gamma ZZ$ coupling is strictly forbidden at tree level, leaving only second-order contributions to the total prediction. This low value of the SM cross section ensures a good probability that any observation in this channel would immediately imply a breakthrough in the scope of the electroweak sector.

1.4.1 *Anomalous gauge couplings*

One may use the effective approach introduced in section 1.1, to enlarge the scope covered by the standard model in the treatment of boson couplings. This anomalous formalism can be set as an extension of the full SM Lagrangian to higher order dimensional terms, as seen in equation (1.1). Therefore, the anomalous Lagrangian density introducing these new operators can be rewritten as an infinite sum of increasing order terms:

$$\mathcal{L}^{\text{eff}}_{\text{BSM}} = \mathcal{L}^{(4)}_{\text{SM}} + \mathcal{L}_5(\Lambda^{-1}) + \mathcal{L}_6(\Lambda^{-2}) + \mathcal{L}_7(\Lambda^{-3}) + \mathcal{L}_8(\Lambda^{-4}) + O(\Lambda^{-5}).$$

Again, one may restrict to the lowest-dimension operators modifying the electroweak sector's density, containing at least one photon interacting term. Furthermore, if a minimally intrusive theoretical assessment such as the conservation of the discrete C, and P symmetries are to be observed, one obtains the following dimension-6 extension:

$$\mathcal{L}_6 = \mathcal{L}^0_6 + \mathcal{L}^C_6 + \mathcal{L}^n_6.$$

In these three additional components involving photons constructed above, only two are predicting a non-zero contribution to the $\gamma\gamma VV$ coupling [59]:

$$\begin{aligned}
\mathcal{L}^0_6 &= -\frac{e^2}{8}\left\{\frac{a^W_0}{\Lambda^2}F_{\mu\nu}F^{\mu\nu}W^{+\alpha}W^-_\alpha + \frac{1}{2\cos^2\Theta_W}\frac{a^Z_0}{\Lambda^2}F_{\mu\nu}F^{\mu\nu}Z^\alpha Z_\alpha\right\} \\
\mathcal{L}^C_6 &= -\frac{e^2}{16}\left\{\frac{a^W_C}{\Lambda^2}F_{\mu\alpha}F^{\mu\beta}(W^{+\alpha}W^-_\beta - W^{-\alpha}W^+_\beta)\right. \\
&\qquad \left. + \frac{1}{\cos^2\Theta_W}\frac{a^Z_C}{\Lambda^2}F_{\mu\alpha}F^{\mu\beta}Z^\alpha Z_\beta\right\},
\end{aligned} \tag{1.8}$$

with Θ_W the weak mixing angle parametrising the relation between the $SU(2)$ and $U(1)$ coupling constants, $W^{\pm\,\alpha}$ the $W^\pm$ boson field, $F_{\mu\nu}$ the electromagnetic field strength

tensor, and $a^V_{0,C}$ (where V is either labelling a $W^\pm$ or a Z gauge boson) the dimensionless anomalous parameters.

A third term, $\mathcal{L}_n$, is only involving one single photon to the coupling, and provides a prediction for the purely anomalous quartic $W^+W^-Z\gamma$ coupling. For the sake of completeness, one may also quote another approach, described in [60], and furthermore imposing the local $U(1)$ and $SU(2)$ symmetries conservation.

In this thesis, one will restrain to the simpler approach above, enabling to quote a direct sensitivity comparison with respect to the former limits set experimentally at LEP-2 [61]. These two terms, giving a non-zero contribution to two-photon interactions with gauge bosons pairs, are thus introducing the two extra parameters/coefficients for each channel of interest, namely $a^W_{0,C}$ for the $\gamma\gamma W^+W^-$ coupling and $a^Z_{0,C}$ for the purely anomalous $\gamma\gamma ZZ$ coupling at tree level. It also introduces the "cut-off scale" Λ which defines the relative energy range at which these anomalous couplings are to become noticeable.

Given these additional terms in the total effective Lagrangian density, the anomalous production cross-section for these processes is given by [62]:

$$\sigma^{\gamma\gamma\to VV}_{\text{BSM}}\left(a^V_0, a^V_C\right) = \sigma^{\gamma\gamma\to VV}_{\text{SM}} + a^V_0\sigma_0 + \left(a^V_0\right)^2\sigma_{00} + a^V_C\sigma_C + \left(a^V_C\right)^2\sigma_{CC} + a^V_0 a^V_C\sigma_{0C}.$$

Therefore, in the two-dimensional anomalous parameters plane, the constant values of the total anomalous cross section are distributed on an elliptic path circling the SM prediction $(a^V_0, a^V_C) = (0,0)$ with value σ_{SM}.

One can also quote a higher-dimensional solution, with its higher degrees of freedom multiplicity. For instance, the dimension-8 operators [63, 64] providing a finite component for the two quartic coupling predictions are attached to the four parameters $f_{M,0-3}$.

Their extended dynamic range allows to include a light Higgs boson to the overall scheme. Therefore, the higher-dimensional solutions are a safer yet more complex approach to the full anomalous gauge couplings picture.

For the sake of simplicity and consistency with respect to the former LEP studies quoted above, the emphasis will be put on the dimension-6 parameters in the experimental studies performed at the LHC, and described in chapter 3. However, a direct relation [59] exists between the dimension-8 and the former dimension-6 parameters. In the $\gamma\gamma W^+W^-$ coupling case, for example, this relation is:

$$\begin{aligned}\frac{a^W_0}{\Lambda^2} &= -\frac{4M^2_W}{g^2}\frac{f_{M,0}}{\Lambda^4} - \frac{8M^2_W}{g'^2}\frac{f_{M,2}}{\Lambda^4},\\ \frac{a^W_C}{\Lambda^2} &= \quad\frac{4M^2_W}{g^2}\frac{f_{M,1}}{\Lambda^4} + \frac{8M^2_W}{g'^2}\frac{f_{M,3}}{\Lambda^4}.\end{aligned}$$

with $g = e/\sin\Theta_W, g' = e/\cos\Theta_W$ the electroweak coupling constants. Hence, the dimension-6 operators can be extracted from any dimension-8 search.

1.4.2 *Unitarity conservation*

A major setback for the additional degrees of freedom attached to the quartic gauge bosons couplings is the introduction of a unitarity violation at high energy scales. This behaviour mainly arises from the new Lagrangian terms through which the $SU(2)$ local symmetry is not preserved in the modified electroweak sector.

In particular, in the two-photon production mechanisms studied in this thesis, this boundary corresponds to $w_{\gamma\gamma} \sim 1$ TeV. Hence, as pictured in Fig. 1.18 for the $\gamma\gamma \to W^+W^-$ process, a violation of unitarity may lead to cross sections beyond any physical value at this energy range.

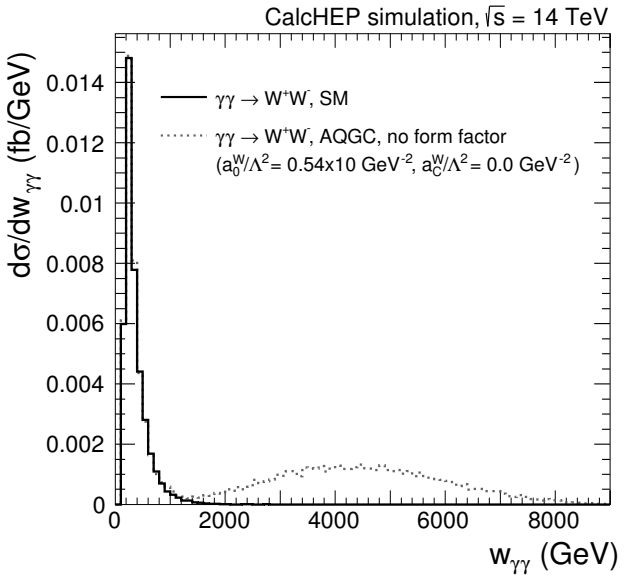

Figure 1.18: Differential cross sections two-photon invariant mass spectra for the $\gamma\gamma \to W^+W^-$ process. The SM prediction is the plain black line, while an AQGC point is quoted as the dashed grey line. One can emphasise the magnitude of the unitarity violation in high two-photon energy scales. Figure extracted from [62].

While the TeV-scale was not reached through the previous attempts performed at LEP, the LHC is expected to probe this region with a sufficient sensitivity. The unitarity

breakings are then a potential showstopper giving rise to diverging cross sections, and should be avoided in any case.

A way to suppress these divergences is to re-scale the couplings according to the two-photon centre of mass energy. For instance, in the dimension-6 case described above, the couplings can be transformed as

$$a_{0,C}^{V} \longmapsto a_{0,C}^{V} \times \left(\frac{1}{1 + w_{\gamma\gamma}^{2}/\Lambda_{\text{cutoff}}^{2}} \right)^{p},$$

where p is introduced as an additional free model parameter to control the high-energy suppression rate. Usually named the *dipole form factor*, its value is conventionally set to 2.

Moreover, Λ_{cutoff} is set in accordance to the two-photon centre of mass energy accessible in all experimental conditions. This parameter gives an upper limit on the theory's (and renormalisation's) validity.

This effective model along with its fine form factor corrections, was developed by T. Pierzchała *et al.* and embedded in two multi-purpose event generators: `CalcHEP` [65] (since its version 2.3), and `MadGraph` [66].

Both these generators are relying on the EPA described in section 1.2.1, thus quote an amplitude for this two-photon induced process using integrated photon fluxes.

2

THE CMS DETECTOR

The *Compact Muon Solenoid* (CMS) detector is one of the two multiple-purposes experiments out of the four present at the CERN *Large Hadron Collider* (LHC). Despite its strong main motivation of probing the electroweak sector of the standard model (especially the so-called "Higgs sector") the physics program has always been broader than this main purpose.

2.1 THE LARGE HADRON COLLIDER

The *Large Hadron Collider* (LHC) is a 27-km circular storage ring built at the border of France and Switzerland, in the suburbs of Geneva. Its host, the *Organisation européenne pour la Recherche Nucléaire* (CERN) is in charge of its construction, operation and maintenance, along with the numerous countries participating to the project.

This accelerator is designed to be filled with protons beams as well as heavy ions, such as lead atoms. The complex accelerator chain upstream enables a progressive raise in the total energy of particles. The original machine design is a proton-proton centre of mass energy of 14 TeV in the original design, corresponding to about 14000 times the mass energy on shell of the proton. During 2010 and 2011 data-taking epochs the energy was set to a lower value of 7 TeV for machine sustainability and development reasons. It was then slightly pushed up to 8 TeV in 2012, to achieve a peak energy of 13 TeV after the first long shut-down in 2013-2014.

Hence, along with the proton-proton (pp) collisions two other operating modes are also made available for the LHC, as lead ions ($Z = 84$) can also be accelerated using a slightly different chain of injectors. This enables the access to larger spectra of studies when probing lead-lead ($PbPb$) collisions, or asymmetric proton-lead (pPb/Pbp) collisions.

Four main experiments are located at four points on the circular tube where the two opposite-direction beams cross. Their name reflects their main fields of study, namely

- LHCb, whose focus extends from the b quark phenomenology and the high-precision flavour physics to the search and study of CP-violation,
- ALICE (A Large Ion Colliding Experiment) studying the quark-gluon plasma states created at the collision of heavy ions,

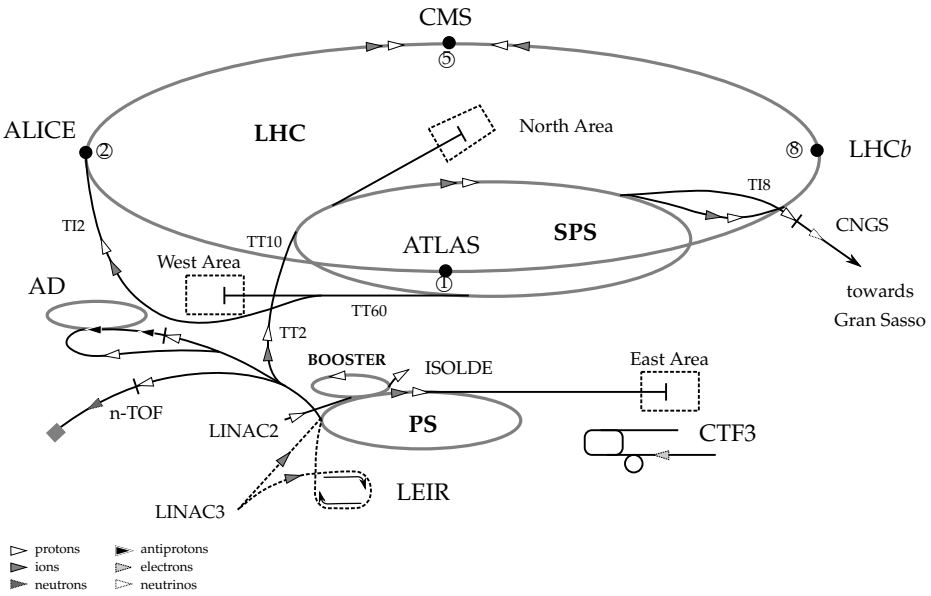

Figure 2.1: The CERN accelerator complex. The CMS experiment lies on top of this figure, at LHC's fifth interaction point, or "Point 5", facing all pre-accelerators and injectors components.

- ATLAS (A Toroidal Large ApparatuS) and CMS (Compact Muon Solenoid) the two general-purposes experiments studying the proton-proton collisions and the proton-lead and lead-lead collisions as well.

In this thesis, the emphasis will be set on the CMS experiment operating with proton-proton collisions, and further information on the other experiments and operating modes can be found elsewhere.

2.1.1 *What is in a beamline?*

In an ideal world, a proper beamline must combine all the following constraints in a very simple set of elements:

- the propagation of all particles of a beam through its full coverage,
- the minimisation of this beam's transverse section,
- the uniform acceleration of all these particles.

The LHC machine ensures all criteria with the use of numerous *optical elements* (or magnets) of different architectures and usages, defined below.

Nevertheless, before their introduction in this LHC accelerator, particles follow a rather complicated chain of acceleration pictured in Fig. 2.1. All the preliminary accelerating stages can be divided into two sub-parts:

LINEAR ACCELERATORS such as the LINAC 1 and 2, increasing individual charged particles' energy through the usage of electromagnetic pulses synchronised with them. At CERN, this LINAC accelerator enables the initial, "at rest", proton beam to reach an energy of 50 MeV before its propagation to all following elements.

CIRCULAR ACCELERATORS such as the BOOSTER, the PS, the SPS or the LHC. This latter technology is injecting energy with the use of eight 400 MHz radio-frequency cavities.

Being circular, the accelerator itself needs to continuously bend the trajectory of the whole particles envelope. It then relies on an important set of dipoles as part of the optical chain of the accelerator for this bending to appear on a large kilometre-range scale.

In addition to the 1232 dipoles, the beams are furthermore focused (spatially "squeezed") to a finite orbit with a narrow spatial extension in the beam transverse plane. This is done with a big set of 992 quadrupoles.

All the magnetic appliances rely on superconducting components that enable to reach high fields with a limited power consumption of 600 GWh yearly.

2.1.2 *Parameters of interest*

Before describing the operation of a beam and its characteristics one may define several quantities of interests commonly used as part of the collider physics *jargon*.

Firstly, as a matter of quantifying the collision (or more generally the interaction) rate, the notion of *luminosity* needs to be introduced. Its definition implies the knowledge of the bunch structure of the beams themselves, as well as their spatial extensions. If one accelerates at a revolution frequency f_{rev} a given amount of bunches i composed by $N_{i,k}$ particles, sharing a common transverse extension $\sigma^*_{x,y}$ at the interaction point, the instantaneous luminosity can be defined as:

$$\mathcal{L} = \frac{f_{\text{rev}}}{4\pi} \frac{1}{\sigma^*_x \sigma^*_y} \sum_{\text{bunch } k} n_{1,k} n_{2,k} \tag{2.1}$$

An interesting feature of this luminosity $\mathcal{L}$ is its direct association to the production rate of any particular process X, given its interaction cross section:

$$\frac{\mathrm{d}N_X}{\mathrm{d}t} = \sigma_X \cdot \mathcal{L}. \tag{2.2}$$

Its conventional unit is a multiple of a $\text{cm}^2 \cdot \text{s}^{-1}$ for the instantaneous luminosity, while the integrated luminosity $L = \int \mathrm{d}t \cdot \mathcal{L}$ is generally expressed as the inverse of a *barn* (10^2 fm^2).

One can hence see that the f_{rev} and $\sigma^*_{x,y}$ are important quantities to handle for a proper operation of the machine at a constant amount of matter injected in the beam pipes. The latter quantities can be redefined as a function of two more commonly used beam parameters, namely the normalised *transverse emittance* ϵ_n and the *betatron amplitude function* β:

$$\sigma^*_x \sigma^*_y = \epsilon_n \beta$$

This "*β-function*" is a function of the *beam path length s*, its circular coordinate defined with respect to an arbitrary point of the accelerator ring. It can furthermore be parameterised as:

$$\beta = \beta(s) = \beta^* \left(1 + \left(\frac{s}{\beta^*}\right)^2\right),$$

with β^* a unit length machine parameter adjusted through the setting of the whole beamline optics [67]. This β^* is therefore defining the collimation level reached at the interaction point. It is also often used to parameterise the spatial extension of the beams in their forward region.

The general luminosity definition (2.1) can hence be rewritten as:

$$\mathcal{L} = \frac{f_{\text{rev}}}{4\pi} \frac{\gamma n_b n_1 n_2}{\epsilon_n \beta},$$

with n_b the number of bunches per beam, and $n_{1,2}$ the number of particles per bunch for each beam circulating in opposite directions.

The full reference for the machine parameters defined in LHC's Run-1 can be found in [68, 69].

Given the complex bunches structure reached at the LHC[1], multiple hard and softer interactions can be encountered in each "event" (bunch crossing) reconstructed in any detector observing each collision. Such additional "events within an event" are commonly called *event pileup*, or *pileup*. This physical increase in the multiplicity of interactions, as many independent observables, can be parameterised using a Poisson distribution. Hence, the probability to observe k primary vertices (bunch crossings) in an event is given by:

$$f(k|\mu) = \frac{\mu^k e^{-k}}{k!},$$

where μ is a positive number defined as the expected value of this distribution, and $k!$ is the factorial of this number k of primary vertices. When characterising this pileup effect, one generally specifies the μ-value observed in a fiducial region of the experiment observing the bunches crossing.

[1] These follow all beam intensities, collimation state, etc. as defined earlier.

2.1.3 *Beamline components simulation*

The simulation of the numerous optical components forming the beamline in an attempt to describe the complete picture of all phenomenon occurring in this region is a complicated matter. Several techniques enable to extract part of this picture while limiting the set of numerical simplifications to ease this computation along complex beamlines.

Nevertheless, it can be simulated by treating each optical element (such as dipoles, quadrupoles, etc.) as a propagator through which each particle in a beam is transiting. Mathematically, one may write a complex electrostatic set of differential equations in a simplified manner:

$$\mathbf{x}(s) = \mathbf{x}(0) \cdot M_{\text{beamline}} = \mathbf{x}(0) \cdot M_1 M_2 \dots M_n, \tag{2.3}$$

where the $\mathbf{x}(s)$ is a n-dimensional point in the phase space picturing the individual particles' kinematic quantities. Furthermore, the M_n factors are the $n \times n$ transport matrices of each beamline element providing a projected set of coordinates for the particle once its kinematics is propagated through the element.

This technique, described in details in [70, 71], was used in several tools listed later in this text, in section 4.4. A more precise description of all requirements for a complete simulation of the beam collisions' forward regions will also be provided in the chapter 4.

2.2 CMS: "CENTRAL" DETECTOR GEOMETRY

As mentioned in the previous section, CMS is one of the general-purposed experiments installed around one of the interaction points of the LHC, the IP5 (for *interaction point 5*). Like many particle colliding experiments formerly or currently in operation, it is built along an onion-like structure with a central *barrel* surrounding the beamline, and two *endcaps* enclosing it to ensure a full sensitive coverage. The full central apparatus is pictured in Fig. 2.2.

From the beam lines outwards, its detection layers are successively the tracker, the electromagnetic and hadronic calorimeters, and muon chambers. Many other sub-components are also providing additional information on any event triggered by the detector.

The reference frame used for a complete geometrical description of the sub-detectors is pseudo-cylindrical, and very commonly used in high energy physics. One can define any object according to three coordinates, namely η, ϕ, and z (see Fig. 2.3). The first one, the unbound *pseudo-rapidity* is defined as

$$\eta = -\ln\left(\tan\frac{\theta}{2}\right),$$

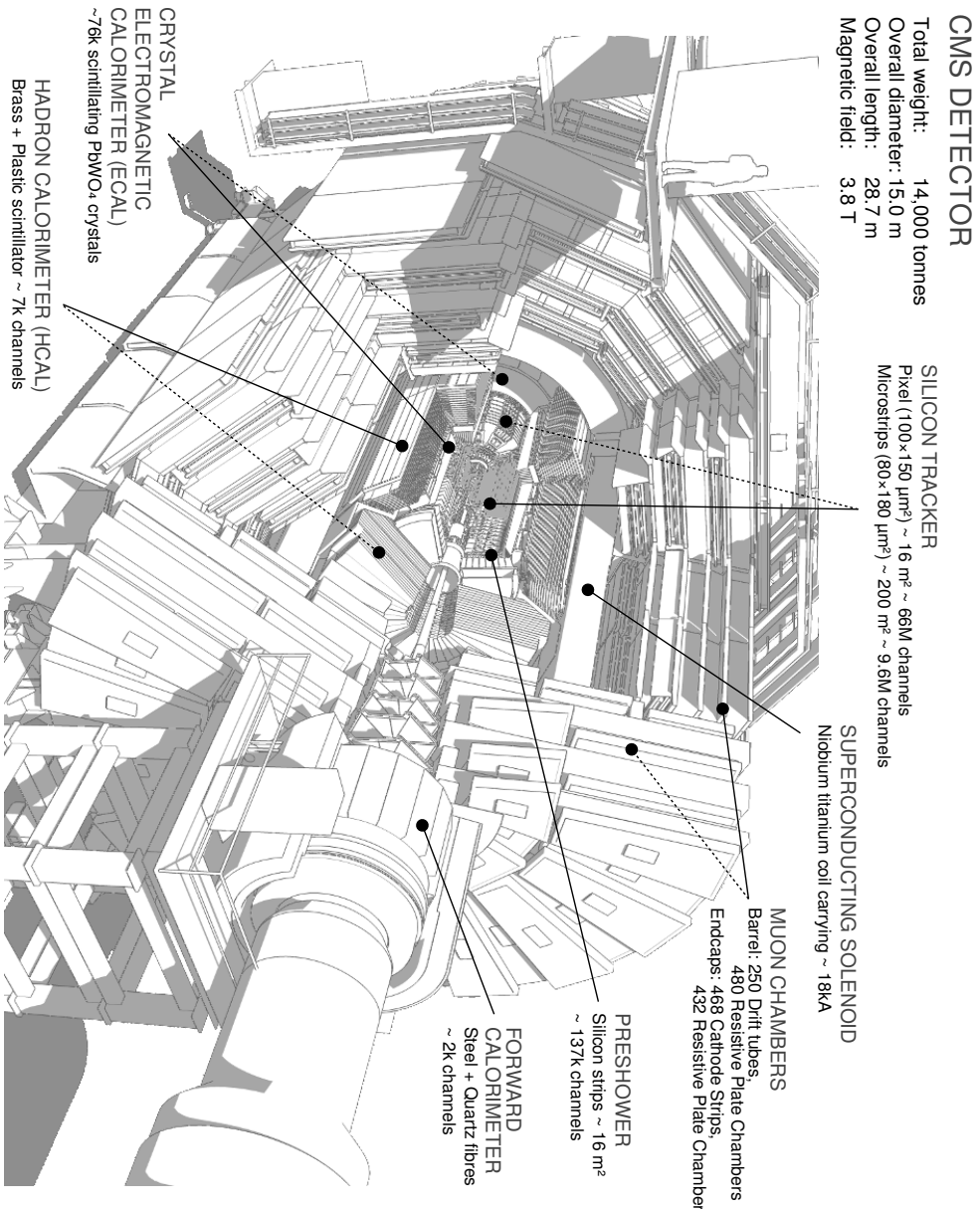

Figure 2.2: 3-dimensional view of the central CMS detector, along with parts of its forward components. The scale is given by the human silhouette standing on the top platform.

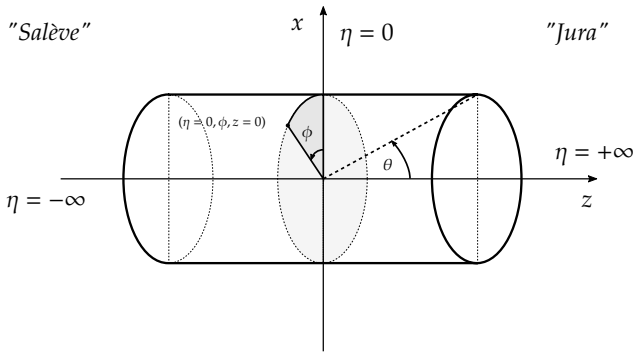

Figure 2.3: CMS pseudo-cylindrical coordinate system.

with θ the polar angle with respect to the beam direction (with its origin defined as pointing upwards). This quantity is hence cancelled in a direction perpendicular to the collider plane, while the $\pm\infty$ values are pointing to the beam lines direction. Furthermore, it is a Lorentz invariant and one can show that in the ultra-relativistic approximation (valid for a negligible mass or a very high energy of the considered object), $\eta \simeq y$, with y the *rapidity* defined as

$$y = \frac{1}{2} \log \frac{E + p_z}{E - p_z}.$$

The second coordinate of interest is the azimuthal angle ϕ defined with respect to the vertical axis pointing upwards. Finally, the third one is the longitudinal axis z. In CMS, the convention is to define its positive coordinates as pointing towards the western Jura mountains facing LHC's Interaction Point 5 (IP5).

In the following parts of this section, a summary of all the different components of this global detector will be given.

2.2.1 *Silicon tracker*

The first layers of detection (closest to the beam line) at the CMS detector naturally involves the tightest requirements on radiation hardness. It must sustain an expected fluence of 1.6×10^{14} 1-MeV equivalent neutrons per squared cm at design instantaneous luminosity [72].

It is divided into a barrel part with a coverage of $|\eta| \lesssim 1$ and the two endcaps ($1 \lesssim |\eta| \lesssim 2.5$). Additionally two layers of sensitive detectors can be quoted for this first component.

The innermost part, the *silicon pixels*, is composed of three cylindrical layers of detection with a very limited material budged. These layers are themselves covered with

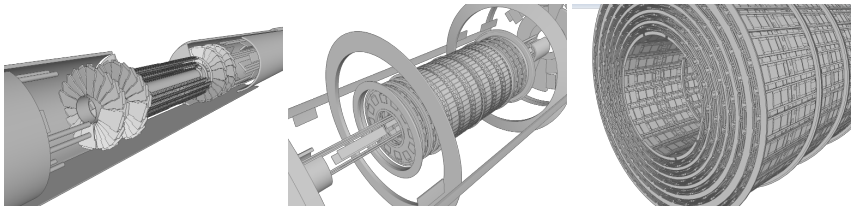

(a) Pixel detector (b) SiStrips TIB/TID (c) SiStrips TOB

Figure 2.4: Silicon tracker components. The first figure is picturing the pixel detector only, while the two others are including the silicon strips detector.

100×150 mm^2 sensitive silicon cells ensuring its high resolution tracking capabilities. A closeup of this sub-part is shown in Fig. 2.4a.

Next to this pixel detector, the *silicon strips* detector enables to achieve a slightly coarser spatial resolution (at the order of a few dozens of μm). Nevertheless, the lower material budget (and cost per module) used there enables to reach a high coverage extending to $|\eta| < 2.5$, given its important modules density: around 10M strips divided in 15k modules covering a total surface (all layers included) of 200 m^2.

The *Université catholique de Louvain* was deeply involved in the construction of this latter part, providing a good fraction of the *petals*, *i.e.* the individual modules making up the endcaps, installed in the high-η regions.

This high granularity allows, combined with the surrounding magnetic field, to reach a tracking momentum resolution within 10% for TeV-scale transverse momenta. The magnetic field itself, reaching a flux density of 3.8 tesla, is generated by a superconducting solenoid driven by a 18 kA current (thus storing an energy of 2.5×10^9 J).

2.2.2 *Calorimeters*

With the requirement to allow a direct detection of electromagnetically interacting particles, the ECAL is the second layer of detectors from the beam line. It consists of 61,200 (barrel) + 14,648 (endcaps) high-density $PbWO_4$ crystals (8.28 g/cm^3) grouped in 36 super-modules (in the barrel) and 4 "dees" (according to their shape, and located in the endcaps). This high density enables the whole detector to remain compact, while retaining a fine granularity.

The goal is to reconstruct with ease and precision the energy of any particle interacting electromagnetically inside its volume.

As many scintillator technology detectors, the individual cell dead time is a critical constant to be kept under control. Therefore, this crystal lead material is chosen to reduce significantly the scintillation decay time, enabling 80% of the total emitted light to be emitted within two LHC bunches crossing (hence, 25 ns).

Its important role in the electrons and photons candidates reconstruction makes it a very powerful sub-component of the whole CMS apparatus. The CMS detector having been designed and built for the Higgs boson search and discovery, the main decay channels of this latter were to be probed with a good performance. Therefore, its high granularity emphasised above allows to reach a $1-4\%$ energy resolution, thus providing a resolution within 1% in the two-photon invariant mass.

Following this ECAL, one finds the *hadronic calorimeter*, or HCAL. Its purpose lies in the measurement of hadron showers through the detection of their components using a succession of passive (brass absorbers) and active (plastic scintillator) layers. It is again splitted into a barrel component, and two forward sub-parts: the endcaps, and the forward calorimeter.

The barrel part has a physical extension constrained by the ECAL and the solenoid's iron return yoke. Nevertheless, it uses this geometrical particularity while relying on an additional sensitive layer set outside this yoke (HO), and using it as an additional layer of absorber.

Along with the barrel, the endcaps ensure a maximal coverage to be reached around the collision point, therefore constraining most of the particles energy to remain inside its volume.

The latter part, the HF [73], is useful for a complete evaluation of the instantaneous luminosity delivered by the LHC machine to the detector. Indeed, its high-η coverage (from $|\eta| = 3$ to 5.2) enables it to be very close to the beamline, with a high expected fluence (the closest part is facing 1 MGy/year). It is therefore sensitive to the passing of particles resulting from forward hadronic interactions.

The principle of operation is relying on the Cerenkov light (see section 4.3.1) emitted by the particles building the shower from a stainless steel absorber. These particles are then directly detected into 1000 km of radiation-hard quartz fibres used as an active part of the detector. Hence, the electronics readout by *photo-multiplier tubes* is kept safe while standing far away from the showers, outside of the high-radiation volumes.

2.2.3 *Muon chambers*

Composed of three different subsystems, the muon chambers allow a precise determination of the main kinematic quantities associated to every muon object recorded in an event. Three layers of detections are used in this sub-component:

DRIFT TUBES (DTs), a one-dimensional netting of wires (anodes) within gas-filled (a mixing of 85% Ar, 15% CO_2) cells. Once a charged particle transits through the netting, charges are knocked out from the gas, and propagated by the surrounding electric field to the anodes wires collecting the signal. The time of arrival of this

signal determines the exact position of the hit, knowing the constant drift speed in the medium.

CATHODE STRIP CHAMBERS (CSCs), very close to the DTs principle of operation, but in which cathode strips are installed perpendicularly to the wires, thus providing another measurement. Indeed, once with each electron extracted from the gas medium is created a positive ion. It is then collected to the cathode strips, thus providing a two-dimensional measurement for each hit, along with the wires information.

RESISTIVE PLATE CHAMBERS (RPCs), composed of two parallel high resistivity plates connected as anode/cathode, and separated with a gas volume (a mixture of 95% $C_2H_2F_4$, 5% iso$-C_4H_{10}$). With each charged particle passing through the gas, electrons/ions pairs are created. An avalanche effect is then generated from the scattered secondary electrons interacting with other gas atoms. This high multiplicity of electrons, amplified by the inner electric field, can then be collected just outside the volume, in strips of conducting metal (copper).

With the three sub-detectors combined, an excellent spatial and time resolution can be achieved on every hit reconstructed in the muon chambers, as seen in section 2.4.2.

2.3 FORWARD DETECTORS

Several sub-detectors are specifically designed to operate in the very forward regions of general-purposes experiments. Within the CMS environment, one can quote the CASTOR (*Centauro And STrange Objects Research*), in the pseudo-rapidity range $-6.6 < \eta < -5.1$, and the ZDC (*Zero-Degree Calorimeter*) installed at a z-distance of ± 140 m on both sides of the interaction point.

Both the detectors are, like the HF described above, Cerenkov sampling calorimeters, being the only technology which can sustain in such a high radiation environment. They rely on a segmentation in their absorbing module thickness, which enables to distinguish between hadronic and electromagnetic showers.

This set of very forward apparatuses, along with the HF, are still considered as embedded in the full CMS detector itself.

In an even further distance stands an independent detector, is located the TOTEM experiment (standing for *TOTal Elastic and diffractive cross section Measurement*) [74], with one of its subcomponents pictured along with the CASTOR apparatus on Fig. 2.5. Its main goal is to probe the area around the beamline in the very forward region.

By observing the rate of deflected particles at a given luminosity, it enables to measure the elastic and inelastic interaction rate at LHC energy ranges. These parameters provide a mean to probe the proton structure functions by studying their differential behaviours.

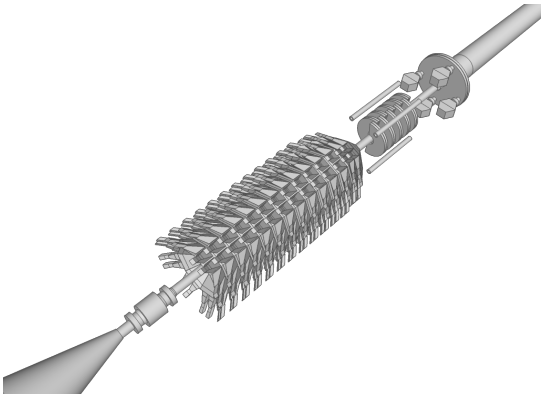

Figure 2.5: 3-dimensional view of CASTOR, closely followed by TOTEM's T1 telescope.

As for the CMS detector, several layers of sensitive detector technologies are used to perform the measurement within TOTEM. For instance, one can quote the two telescopes T1 and T2 located respectively at 9 and 13.5m (hence, inside the HF on one side, and the CASTOR on the other side) around the IP5. These contain tracking devices: in T1, 5 planes of CSCs (as for the CMS muon chambers), along with 20 planes of GEM tracker in T2, with a respective $|\eta|$ coverage of (3.5 – 4.7) and (5.3 – 6.5). Both the telescopes are pictured in Fig. 2.6.

Furthermore, several other sub-components are placed in so-called *Roman pots* located at a short distance from the outgoing beam pockets on both side of the CMS central detector. These *Roman pots* are a class of apparatus enabling to observe the beam at the closest distance of approach (within the range of a few millimetres).

As part of a joint (very) forward physics programme with CMS, the TOTEM Collaboration enabled to provide its big expertise in installation and operation of this *Roman pots* technology. This enabled to share a strong link to convey the FP420 [75] a previous *R&D* project, joint with ATLAS, and develop the CMS-TOTEM Precision Proton Spectrometer fully described in chapter 4.

2.4 DATA COLLECTION AND SELECTION

With five years and a half worth of data collected at various centre of mass energy, the LHC experiments gave a good picture of their capability to sustain a high collision rate with an outstanding operation time. The full data collected so far (as at the end of the year 2015), can be separated in two runs separated by a two-years gap intended to increase the LHC (along with most of upstream machines) capabilities, in addition to the upgrade of several parts of the detectors.

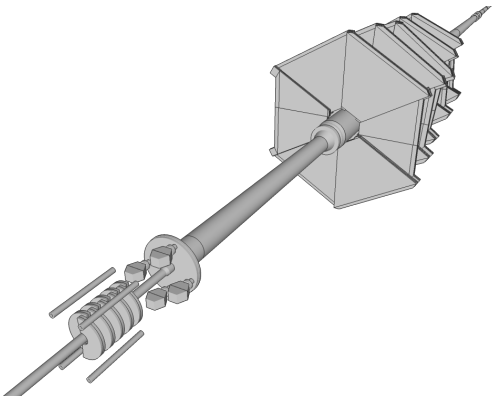

Figure 2.6: An isometric view of TOTEM's T1 and T2 telescopes, as pictured around the beamline. In this view, the CMS central detector is upstream to the two apparatuses.

In Fig. 2.7, one can see the relative size of all data-taking periods defined in both Run-1 (2010–2012) and Run-2 (2015) with respect to the calendar day during each year. This does not include the very short commissioning data taking period in 2009.

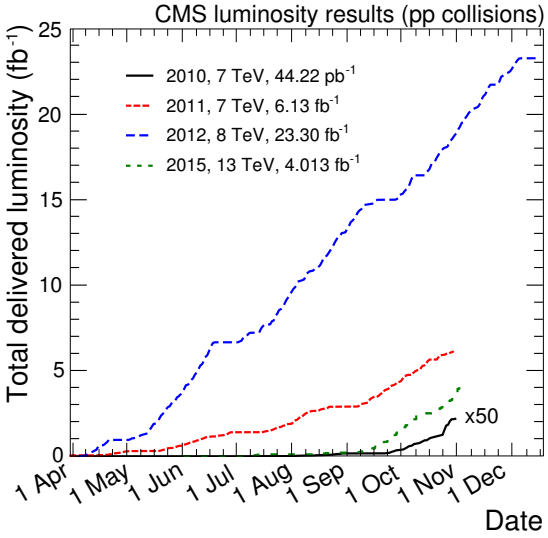

Figure 2.7: Integrated luminosities delivered by the LHC for the 2010–2015 "stable beam" data taking periods in proton-proton collisions at $\sqrt{s}$ = 7, 8 and 15 TeV. Figure built from [76].

Between Run-1 and Run-2, the bunches spacing evolved from 50 ns to 25 ns, or 40 MHz crossing frequency. This allows a slight reduction of the pileup through the

decrease in the mean bunch population, thus the lower collision rates observed in this early Run-2 data collection.

2.4.1 *Events triggering*

In CMS two stages of triggers are required to select events of interest in a deep sea of events observed. Some measured numbers can be quoted to emphasise the need for such a preselection in order to sustain such high rates. For instance, during the 2012 data taking period at $\sqrt{s} = 8$ TeV (adding up an integrated luminosity of about 20 fb^{-1} with an instantaneous luminosity of 8×10^{33} cm^{2}s^{-1}), the proton-to-proton collision rate reached the enormous value of 5×10^8 Hz [77].

Several raw observables can be handled in order to meet the selection requirements, such as the minimal transverse momentum of one or several produced particles, or the invariant mass of a pair, or a minimal number of jets in the final state carrying a minimal energy.

The two selection stages, the *Level 1 trigger* (L1) and the *High Level Trigger* (HLT), select the events given a maximal rate of 100 kHz for the first, and 100 Hz for the second.

The L1 trigger is mainly composed of high frequency, adjustable electronics (ASIC and FPGA modules), running over a minimal set of over-simplified and cleaned observable information. This simplified information is, for instance, the merging of hits in both the calorimeters into *super-clusters* carrying a combined energy deposit, or the retrieval of a limited set of detector information in the event selection, such as the muon system only.

It returns a collection of Boolean bits with a reasonable latency of 3.2 μs once its decision is taken. These bits are then propagated to the second level to let it stop or continue collecting extended sub-detectors information.

After this first "events skimming", one can apply a set of further selections to apply on the remaining ones. This second level, the HLT (*High-Level Trigger*), allows a rate reduction from O(100 kHz) to O(100 Hz) while raising the physics "objects"[2] identification quality. In this part, most of the clustered data is unpacked and processed in a dedicated HLT software component. If the event is observed to pass a predefined set of higher-level constraints, it is directly stored onto the disks for further processing.

2.4.2 *Particles identification and reconstruction*

The computing scheme used in CMS enables any physics analyst to access the maximal information on all stages of reconstruction for all objects in a triggered event.

Among all other LHC experiments, one major feature intensively used by CMS is inherited from the lepton colliders era: the *particle flow*. It allows to enhance the

[2] All types of particles, jets, missing energy, particle flow candidates, ... observable in the full detector are contained in this "object" definition.

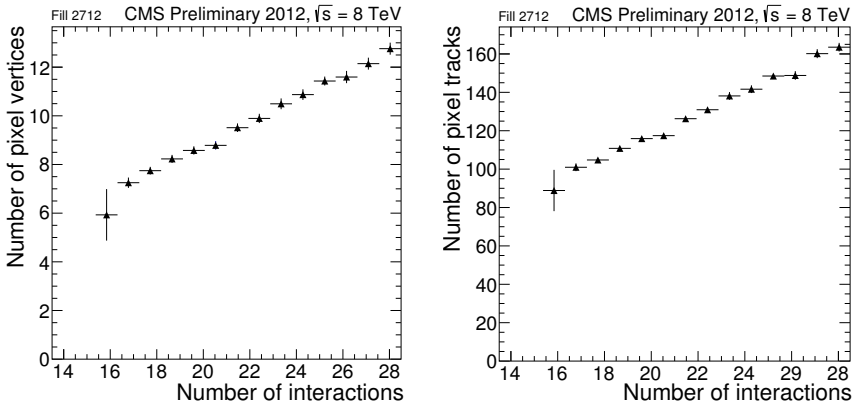

Figure 2.8: Vertexing performances for the pixel detector, as a function of the number of primary interactions in the event. This is extracted from one single LHC fill during the 2012 data-taking period at $\sqrt{s} = 8$ TeV. Figs. from [79].

jets and lighter objects reconstruction by using a pattern recognition tool including all subsystems of the detector as a whole. With this technique, one builds the event by including at each iterations high level objects selected in a decreasing order or confidence. The outcome is an improved efficiency on the more complex identified quantities, such as the hadronic jets or the missing transverse energy, making use of the full information available on clean muons, electrons, etc.

2.4.2.1 *Tracking performances*

As it will be seen in the next chapter, the tracking and vertexing resolutions are crucial in the selection efficiency of exclusive events. Fortunately, with its outstanding reconstruction capabilities [78] in these two matters, the CMS experiment allows to define this exclusivity condition according to track-based quantities.

In Fig. 2.8, the vertexing capabilities are displayed for a single LHC fill at $\sqrt{s} = 8$ TeV. These two figures show respectively the number of vertices observed by this pixel detector, and their tracks multiplicity as a function of the "real" number of primary vertices expected in the event. The latter is reconstructed as the product of the instantaneous luminosity[3] with the two-proton inelastic cross-section.

2.4.2.2 *Muon reconstruction performances*

Being a major hallmark of the CMS detector[4], the reconstructed muons are meant to be the most reliable objects used in all operations. During Run-1 operations, several

[3] This instantaneous luminosity is observed using the HF forward detector described in section 2.2.2.
[4] Leaving aside the fact that it stands for one third of the CMS name.

classes of muon objects were introduced, reflecting objective criteria defined to quantify their quality of reconstruction.

The baseline selection is identifying a muon by the track candidates left either in the tracker or in the outer muon system. If the propagation of a *standalone muon* (visible in the muon system) through the tracker enables to isolate a track, this latter is flagged as a *tracker muon*. Furthermore, if the extrapolation of this tracker muon alone reaches the muon system where a track is to be found, the merged information is labelled as *global muon*. Between the 2011 and 2012 data taking periods, the *particle flow muons* reconstruction algorithm was made the default one for all major offline analyses. The same recipe was used in the analyses performed in Chap. 3.

Once the collection of muon candidates is properly built for each event, several quality selection can be applied on these, such as the track candidates quality or the muon class as described above. Namely, one can quote in increasing order of quality selections, the loose, the soft, and the tight muons.

The latter category was set as a baseline selection for all parts of the analyses described below. It requires the object to be flagged as a global/particle flow muon with a good track quality, either on its tracker track (at least one pixel, and five strips layers hits, a max. 5 mm longitudinal distance and 2 mm transverse impact parameter with respect to the primary vertex), on the muon system track (at least two muon stations hit), or on the combined track (an overall $\chi^2/\text{ndf.} < 10$, at least one hit in the muon chambers).

As seen in Fig. 2.9 for the data collected at $\sqrt{s} = 7$ TeV in 2011, the overall muon reconstruction algorithms are operating within the > 90% efficiency range. An interesting feature is the drop of this efficiency along with the increase of the number of interactions observed in each event (due to the pileup effect, as described hereafter). Unfortunately, this effect reduces furthermore the observation cross section at higher luminosities for any process relying on a tight selection of muons.

2.4.2.3 *Electron reconstruction performances*

As described in section 2.2.2, the high granularity of the whole calorimeter is providing a high resolution on both the electron and photon reconstructed quantities.

The electron reconstruction is performed using two primordial information: a super-cluster SC (an array of ECAL cells above a location-dependant threshold energy), and track candidates as reconstructed in the tracker. The matching between the two collections is done by a Kalman filter in one direction or the other (either a track is extrapolated to the ECAL super-clusters collection or the other way round).

Once a merged set of candidate is built inside an event, a proper selection of the associated physical quantities can be launched to separate real electrons from fakes. In the CMS analyses described in chapter 3, the electron identification criteria used are "cut-based", hence rely on a finite, well-defined set of threshold values to be reached for several quantities. For the sake of completeness, one can quote other multivariate identification techniques of a more complex nature, either relying on the likelihood

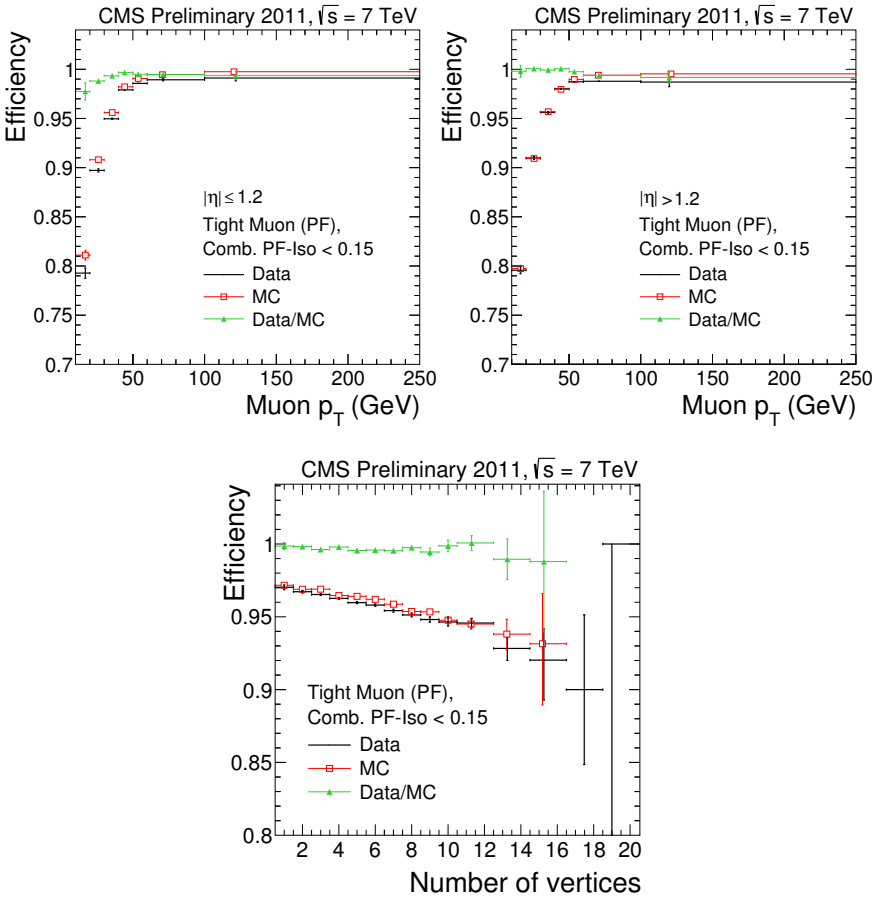

Figure 2.9: Reconstruction performances for particle flow muon objects detected in the barrel, in the endcaps, and inside the whole detector coverage, as a function of the single muon p_T and the number of primary interactions in the event. These efficiencies are computed for the 2011 data-taking period at $\sqrt{s} = 7$ TeV. Figs. from [80].

profile fit over multiple cluster shapes, or tracking variables or building a neural network based on a minimal set of variables.

The full performances of the electron objects reconstruction with the CMS detector have been evaluated at 7 TeV [81] and 8 TeV [82]. The Fig. 2.10 shows the dependence of this efficiency on the transverse momentum of the single electron leg in two η bins.

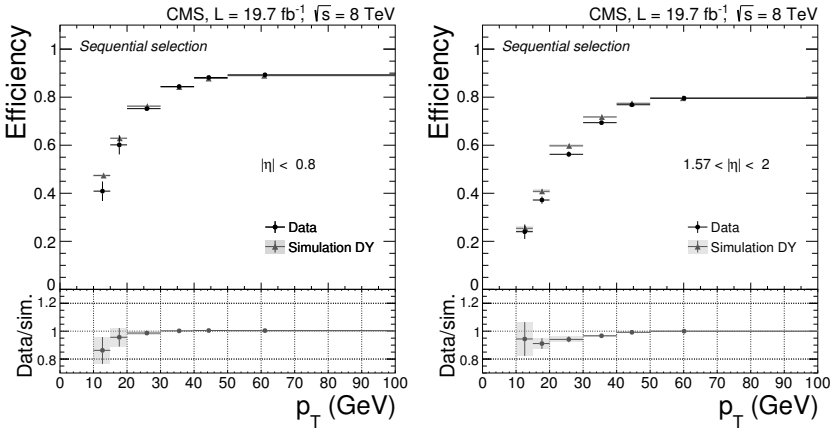

Figure 2.10: Dielectron reconstruction efficiency as a function of the single electron p_T for two pseudo-rapidity bins, as observed in data and simulation (Drell-Yan electron pair production) for the 8 TeV data taking period. Figure extracted from [82].

2.4.3 *Events pileup simulation*

This pileup effect described in section 2.1.2 is to be taken into account in all parts of a proper physics simulation of the detector. Indeed, numerous direct and indirect inefficiencies can be introduced in all sub-parts of the apparatus. For instance:

- a higher charged tracks multiplicity in the inner tracker can cause improper reconstruction due to the higher hits multiplicity,

- a higher energy deposition is expected in all calorimeters, inducing a bigger dead time which can affect photon, electron, or jet energy scales.

In CMS, this effect is simulated by artificially adding to the central event a set of secondary vertices, whose multiplicity is randomly chosen given an input distribution. These additional vertices are extracted from a *minimum bias* [5] events pool collected for each data taking period of interest.

With no prior knowledge of this vertex multiplicity distribution as observed in data, this input distribution is chosen carefully before any simulated event samples definition, and these are furthermore weighted in order to match the observed distribution in data. This computational process is known as *Luminosity re-weighting*, given the direct relation of the pileup conditions to the instantaneous luminosity recorded in collisions.

[5] Minimally triggered data events collected with the full detector, responding to real beam conditions. Several experimental recipes can be used to select the events: CMS is using a set of forward detectors to generate a coincidence ensuring beam presence.

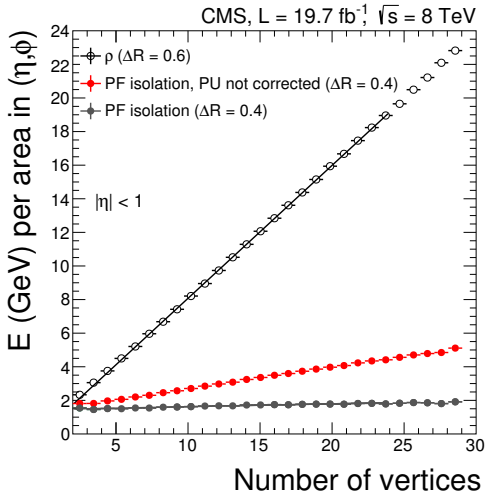

Figure 2.11: Total energy deposited, as a function of the primary vertices multiplicity in the event. Open circles give the median energy density distribution for particles within any $k_T(0.6)$ jet with $p_T^j > 3$ GeV, thus a quantity directly proportional to the energy deposit density. Figure extracted from [82].

One can appreciate the effect of such an effect in the particular case of exclusive events searches, given the importance of a proper tracks and vertex reconstruction in an optimised selection of the signal region. Some examples are given in chap. 3.

3

TWO-PHOTON PHYSICS AT THE LHC

As developed earlier, in chapter 1, the study of two-photon physics processes is a powerful tool to test non-trivial predictions of the SM, and possibly discover new phenomena.

In this view, the CMS experiment at the LHC has been investigating multiple two-photon induced channels, such as the two-photon production of lepton, or gauge bosons (W and Z) pairs described later in this chapter.

This part of the work is based on the two analyses reported by the CMS Collaboration, and detailing the search for two-photon production of $W^{\pm}$ pairs decaying leptonically, performed at $\sqrt{s}$ = 7 TeV (resp. 8 TeV). These two analyses are documented in [83] and [84], respectively.

For the sake of completeness, one can quote three other experimental observations of such two-photon processes at the LHC, and performed using the early Run-1 datasets collected at a two-proton centre of mass energy $\sqrt{s}$ = 7 TeV. In [85] and [86] respectively, the $\gamma\gamma \to \mu^+\mu^-$ and $\gamma\gamma \to e^+e^-$ processes are studied at the CMS experiment. Another study documented in [87] describes the most recent ATLAS results combining both the dimuon and dielectron channels. All three papers quote the observation and quantify the fiducial production cross section for these processes, combining both the elastic and inelastic contributions.

The two earlier CMS analyses being partially embedded in the two searches for the $\gamma\gamma \to W^+W^-$ process described in this chapter, their description will not be covered in this thesis.

3.1 TWO-PHOTON PRODUCTION OF LEPTON PAIRS

This process is characterised by a very clean experimental signature that only involves the detection and reconstruction of simple objects such as leptons and photons. As described later in this section, it is providing an excellent probe to test the fundamental electromagnetic nature of the standard model. The theoretical framework describing its properties is detailed in section 1.3

If one considers the standard model prediction is one of the most precisely described theoretically, this process can be used as a powerful calibration tool for any experimental apparatus in which it can be detected at a reasonable rate.

Indeed, combining this high precision on the purely elastic part of the process with a high observation rate reached at the LHC, one could directly extract the full integrated luminosity delivered by the collider (using Eq. (2.2)). Hence, any study of this process is potentially an additional physics-based method to retrieve this machine parameter useful in all analyses.

This statement was developed in numerous pre-LHC era accelerators, often labelling it a *standard candle* for the evaluation of the integrated luminosity[88].

Later on, this argument was superseded by the excellent performance of the machine-based luminosity[1], reaching the level of 2 – 3% at Run-1 [93]. Nevertheless, this possibility still remains a good additional candidate to be resumed with the setup of a full spectrometer in the forward regions of the CMS experiment, which will provide a direct tagging of such processes (as seen in chapter 4).

If one recalls from the discussion in chapter 1, two variables of interest enable a direct separation between the elastic and the inelastic components of the $\gamma\gamma \to \ell^+\ell^-$ signal: the leptons transverse momentum balance $\Delta p_T(\ell\ell)$, and their angular separation in the transverse plane $\Delta\phi(\ell\ell)$. This separation is shown in Fig. 3.1, in which both the elastic and the inelastic samples are simulated by `LPAIR` and reconstructed through `CMSSW`, the full CMS simulation tool.

In the following parts of this text, the so-called *elastic selection* is introduced as the region defined within the following cuts on the dilepton kinematics:

- a proper balance of the dilepton transverse momenta, constrained experimentally as: $\left|\Delta p_T(\mu,\mu)\right| < 1$ GeV,

- a minimal angular separation in the transverse plane defined by the acoplanarity condition: $1 - \left|\Delta\phi(\mu,\mu)/\pi\right| < 0.1$.

Therefore, the *inelastic selection* is defined as its direct anti-selection.

These two limits were developed in the scope of the earlier search for $\gamma\gamma \to \mu^+\mu^-$ in the CMS detector described in [85]. This latter analysis was using a smaller dataset (about 40 pb^{-1} collected in 2010, thus in early Run-1) in which the pileup contamination was much lower than the two datasets used in this thesis. While the p_T-balance criterion is properly separating the two contributions, the acoplanarity selection is slightly loose. However, the historical values were chosen for consistency in this text.

[1] To name a few, this uncertainty was evaluated using the van der Meer scans technique[89, 90] or, within the CMS environment, extrapolating the pixel detectors capabilities of reconstructing the vertex multiplicities, as listed in [91, 92].

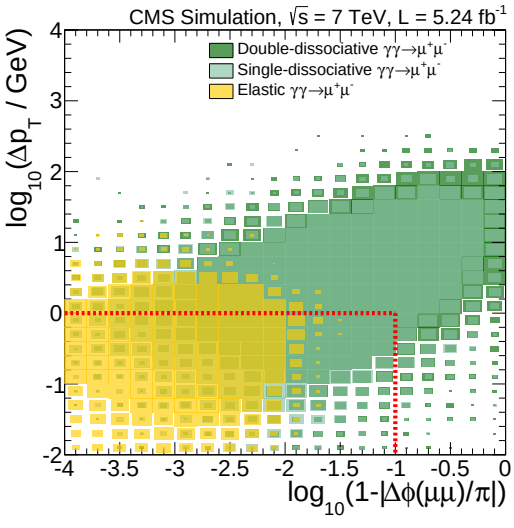

Figure 3.1: Two-dimensional scatter plot at $\sqrt{s} = 7$ TeV for the exclusive $\gamma\gamma \to \mu^+\mu^-$ samples as simulated by LPAIR and reconstructed within the CMS detector. The boxes size is directly proportional to the observed cross section in the region of the phase space. The dashed line quotes the cuts defining the elastic and inelastic selections, as described in the text.

3.1.1 *Exclusivity conditions*

Given the high rate of collisions occurring at each bunch crossing[2] in the LHC environment, the definition of "exclusive events" should be taken with a pinch of salt.

One can shrewdly count on the specific physics behaviour of such a class of events, namely the "colourless" nature of the two-proton interaction. As seen in section 1.2.2, this condition ensures an absence of particles scattering in a relatively big fraction of the detector coverage, commonly known as a rapidity gap.

Hence, this class of events generates a central system clearly isolated from the scattered protons (or remnant jets) in the two forward regions. At CMS, two strategies were used in previous analyses to make use of this property.

The first methodology relies on the information provided by the whole CMS acceptance, including all forward detectors reconstructed quantities. As used in the search for two-photon production of electron pairs[86], the exclusivity condition is requiring a low energy deposition in both the central system, and the array of forward calorimeters described in section 2.3. The latter, being characterised by their high-η coverage, allowed to shed light on this rapidity gap and ensure a direct tagging.

[2] For more information on this phenomenon, see the "pileup effect" defined in section 2.1.2.

The second technique is a track-based condition, using the tracking and vertexing information reconstructed in each event. Given the high performance achieved by CMS to identify such objects, single tracks with a transverse momentum in a range starting at a few hundreds of MeV can be used as seeds to a primary vertex. The vertexing reconstruction algorithm can furthermore operate in a very high tracks multiplicity environment. If one requires that only two tracks are originating from a single primary vertex, and that the two tracks are associated to a higher-level (electron or muon) object, one can define an exclusivity selection ensuring a lower contamination by inclusive production processes. This feature is driven by the harder interaction generally observed in the nuclear breakup of the proton to be faced in an inclusive event. This second exclusivity selection was introduced in the first CMS search for two-photon production of muon pairs[85].

Two statements can be made on these two methods:

- the first assumes a perfect description of the forward apparatuses, and a relative cleanness of the central event within a high-η range, if one takes into account the high occupancy expected per interaction in the forward detectors. It therefore combines the whole detector information into one single event cleanliness decision ;
- the second is relying on the good tracking performances delivered by CMS, along with its good vertexing capabilities, even in a high interaction multiplicities environment.

Hence, with the increase of the mean multiplicity observed in all events, the first method was quickly made difficult if not impossible to sustain. The main reason is the high sensitivity of both the electromagnetic and hadronic calorimeters, including the forward shower counters, to the overall activity to be expected within all parts of the detector. It is therefore by far too restrictive to claim the lack of activity within a high-η range as soon as the two-proton interaction rate increases.

This only leaves with the track-based exclusivity condition, relying on all individual tracks and their associated vertex in the event.

In all experimental results quoted hereafter, this track-based recipe was used as a baseline exclusivity condition: each final state to be reconstructed must remain free of additional tracks arising from its primary vertex.

At this stage, a common baseline selection can be defined for an exclusive dilepton search at the CMS experiment. The dimuon channel was preferably chosen for its higher purity and reconstruction efficiency given all parameters of the detector itself. One can define a common set of minimally constraining requirements to be applied on the data samples collected in 2011 and 2012 at $\sqrt{s} = 7$ and 8 TeV respectively.

First a high-rate trigger path requiring at least two muons, with asymmetric constraints on their minimal transverse momentum is used, *i.e.* where the leading (resp. the trailing) single lepton should be characterised by a transverse energy above 13 or 17 GeV (resp. 8 GeV), depending on the run period considered.

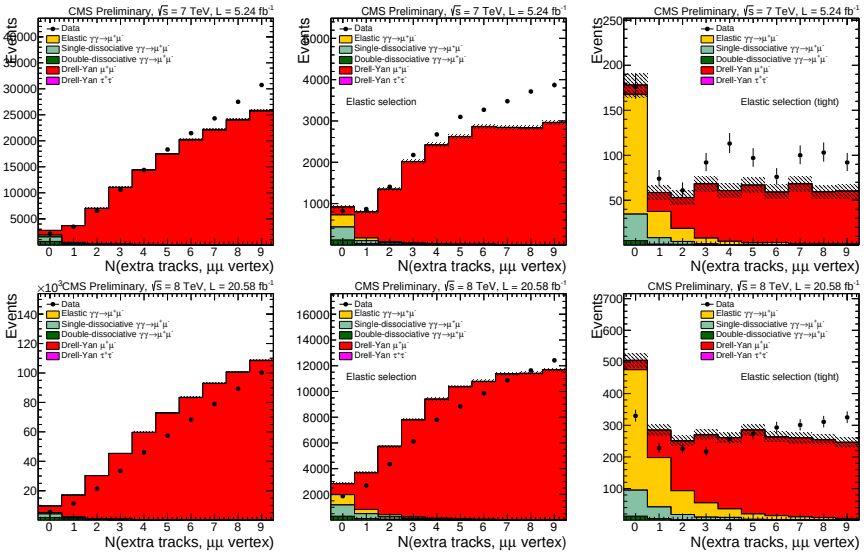

Figure 3.2: Extra tracks multiplicity associated to the dimuon vertices for a centre-of-mass energy $\sqrt{s}$ = 7 TeV (top line), and 8 TeV (bottom line). From left to right, for the raw preselection cuts, the elastic selection, and the tight elastic selection defined in the text.

After the selection of events with at least one lepton pair, a set of quality constraints is applied:

- a common primary vertex associating the inner tracks (or *tracker tracks*) of both the leptons,
- a transverse momentum above 20 GeV for the single muons, hence slightly above the leading lepton cut as selected by the trigger,
- a high purity of the muon track, *i.e.* $\left|\eta(\mu)\right| < 2.4$, at least 8 hits in the tracker, and a *tight identification* flag (as defined in section 2.4.2.2),
- an invariant mass for the dilepton system above all low-mass resonances (thus, $m(\mu\mu) > 20$ GeV), and
- the track-based exclusivity condition defined above (no additional track reconstructed and associated to the primary vertex).

Leaving this last condition open, one can study its behaviour in both the centre of mass energies. The additional tracks multiplicities distributions are shown in Fig. 3.2.

One can already notice that the exclusive selection (the "zero-bin" in these figures) is overestimated by the theoretical predictions (dominated by the elastic, single- and

Sample	Data	Simul.	Data/Simul.
7 TeV	2132	2736 ± 19	0.78 ± 0.02
8 TeV	5514	9956 ± 49	0.55 ± 0.01

Table 3.1: Data/simulation yields observed in the dimuon channel for the exclusive selection defined in the text.

double-dissociative `LPAIR` contributions). This effect is shown numerically in the table 3.1. While a 20% discrepancy observed in the 7 TeV case can be explained from this strong requirement on vertexing/tracking, in which the rather inclusive tunes on reconstruction may operate improperly, it increased significantly at 8 TeV.

This deficit has been studied on multiple fronts for this latter analysis, in order to track its origin. A first effect at the order of 10% comes from an improper simulation of the longitudinal distribution of primary vertices (introduced as a smearing of the vertices z position), thus increasing the observed simulation efficiency. The track reconstruction quality selection, the primary vertices multiplicities, or the dilepton mass region were also varied, and this ratio showed no improvements, nor drops with respect to these variations.

Furthermore, when the full range of the tracks multiplicity on the dilepton vertex is observed as in Fig. 3.3, despite its overall yield agreement over its full range, the observed shape is improperly simulated once the dilepton requirements are introduced. This effect can be explained by the nature of the dominant process on this broad kinematics range (the Drell-Yan inclusive dilepton production).

Indeed, the dominant source of additional tracks in this process primarily arises from the *underlying event* activity[3], while the events pileup accounts for a lower fraction. Unfortunately these effects are still hardly described nowadays, either experimentally or in the theoretical framework of DIS, so that the simulation of the additional tracks in the Drell-Yan sample[4] (relying on a given parameterisation of secondary scatterings) is not finely tuned to this particular kinematics.

This effect is unfortunately particularly visible in the low- and high-multiplicities regions of this distribution (the former defining the region of interest in this analysis). One may also notice the general under-prediction of the central core of this tracks multiplicity, primarily dominated by the QCD production of multi-jets. Given the very high statistics required to pass the first triggering and single lepton selection (this QCD

[3] The secondary interactions faced by the beam remnants, along with the initial- and final-state radiations. A summary of the effects and picture of its parameterisation within modern events generator is given in [94], and its experimental characterisation within CMS can be found in [95].

[4] This Drell-Yan sample has been generated with `POWHEG` [96] and its parton content was fragmented through the *Lund* fragmentation algorithm embedded in `Pythia` [97].

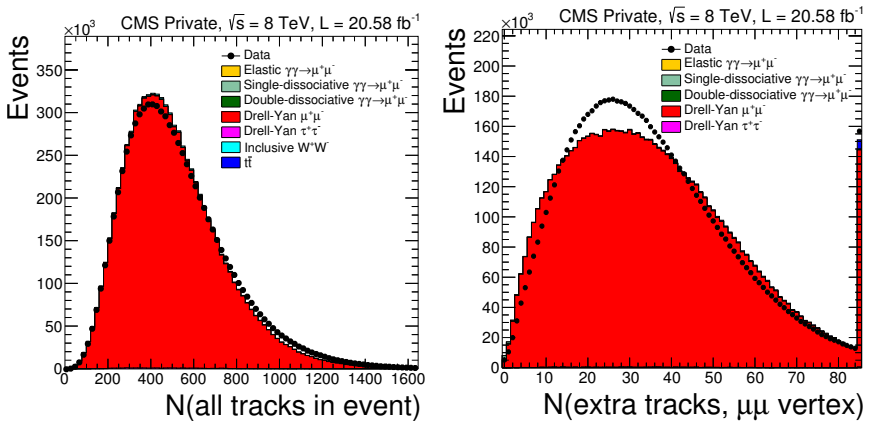

Figure 3.3: Un-zoomed tracks on vertex multiplicity in each event for the 2012 data collected at 8 TeV. Lhs. figure does not require any selection on the central event, while the rhs. figure selects events with two well-reconstructed and identified muons with $m(\mu\mu) > 20$ GeV.

prediction providing a very soft leptons spectrum, below ~ 10 GeV), this process is characterised by a high production cross section, and a low branching ratio to this final state.

To cross-check the stability of this over-estimation of the low track multiplicity region, all the kinematic distributions for additional tracks associated to a dimuon vertex in any triggered event have been studied in details. The vertexing algorithm itself requires a minimal purity of the tracks to include them in its global fit: a normalised $\chi^2 < 20$, a minimal amount of tracker hits (in 2 pixel, and 5 strips layers), and an impact parameter significance below 5.

If one leaves aside the poor theoretical modelling as observed in the transverse momentum spectrum of the additional tracks, the overall agreement is reached in all tracks kinematic distributions once the whole preselection range is selected (as seen in Fig. 3.4 for the dimuon channel).

Given this constant behaviour of the over-estimation of the lower multiplicities of additional tracks on vertex, it was decided to manually correct the observed selection efficiency for the exclusive selection. An overall rescaling factor was applied on all simulated samples contributions falling in this first bin in the $\sqrt{s} = 8$ TeV study. It was extracted from a high-purity sample in which the elastic selection defined in the beginning of this section was furthermore constrained. In this tightened selection, the acoplanarity cut was set at $1 - \left|\Delta\phi(\mu,\mu)/\pi\right| < 10^{-3}$. This very tight selection makes the $\Delta p_{\mathrm{T}}(\mu\mu)$ cut inefficient, thus it is removed in this computation.

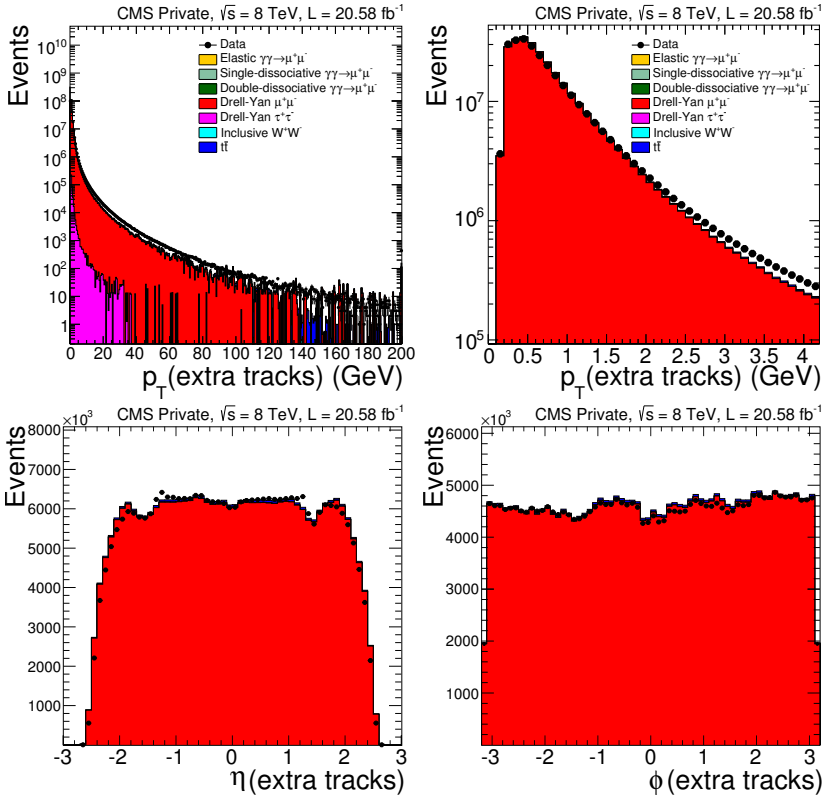

Figure 3.4: Kinematic distributions at $\sqrt{s} = 8$ TeV for all the additional tracks observed on any dimuon vertex present in each selected event in the 2012 analysis. From left to right, and top to bottom: transverse momentum, pseudo-rapidity, and azimuthal angle.

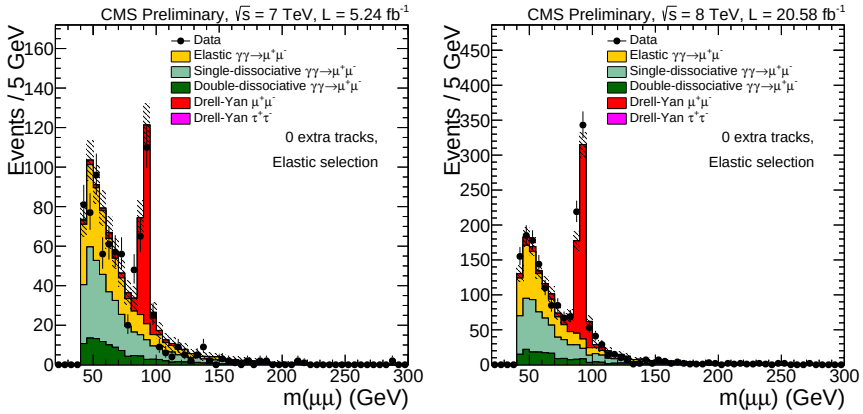

Figure 3.5: Dilepton invariant mass distribution for the exclusive elastic selection at $\sqrt{s} = 7$ and 8 TeV.

The data-to-simulation ratio extracted from this first bin for the whole 2012 sample in the dimuon channel is 0.63 ± 0.04. As an additional cross-check, this very same recipe was applied in the dielectron channel, giving a ratio of 0.63 ± 0.07. Combining both the channels, the total yield is 0.63 ± 0.03, to be applied on all simulated distributions following this exclusive selection in the 8 TeV sample.

An indirect closure test using the nominal elastic selection (*i.e.* $1 - |\delta\phi/\pi| < 0.1$ and $\Delta p_{\mathrm{T}} < 1$ GeV) can be introduced to check the validity of this method. Indeed, as this selection highlights the purely elastic $\gamma\gamma \to \ell^+\ell^-$ production supposedly well described theoretically, one expects to reach a reasonable agreement between the simulated and observed spectra. This is clearly the case as shown in Fig. 3.5 for instance, where the dilepton invariant mass distribution displays the validity of this approach for the 8 TeV data taking period, reaching the same level of agreement as the 7 TeV analysis (in which this rescaling was not applied).

However, if one loosens the acoplanarity/transverse momentum balance requirements, one can study the behaviour of major kinematics variables while maintaining a non-negligible rate of inelastic and dissociative contributions.

3.1.2 *Observation of rescattering effects*

In particular, when inverting this common elastic selection (thus suppressing most of the elastic components) to emphasise the inelastic/dissociative and inclusive contributions, their modelling can be studied in details.

If one returns to the discussion launched in section 1.2, one may recall the large dependence of the overall photon fluxes to the energy transfers Q^2 implied in the reaction. Indeed, even in a matrix element level generator, such as `LPAIR` used to quote

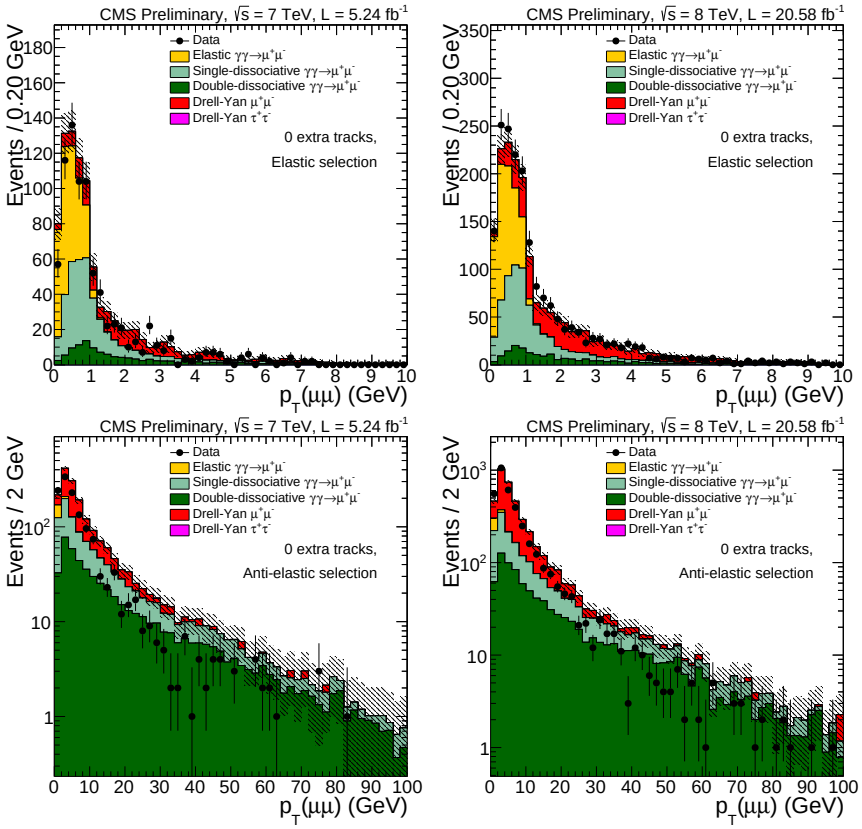

Figure 3.6: Outgoing leptons' transverse momentum distributions at $\sqrt{s} = 7$ and 8 TeV for the elastic selection (topmost figures), and the inelastic selection (bottom-most figures).

the dissociative contributions to this $\gamma\gamma \to \mu^+\mu^-$ process, the F_2 structure function is directly involved in the computation of the unintegrated fluxes.

This MC generator being originally tuned for HERA energies (*i.e.* for lower Q^2 transfers) through the choice of structure functions (in particular, the SY parameterisation introduced in chapter 1), the higher dynamic range reachable at the LHC is not necessarily ensuring a good modelling.

Therefore, given its direct correlation with the Q^2 scale, the dilepton transverse momentum observable is expected to amplify any tension observed in this larger kinematic range. In Fig. 3.6, both the elastic and anti-elastic spectra for this distribution are shown for the two centre of mass energies considered.

As shown, if the elastic selection is properly reproducing the full p_T range, the anti-elastic selection clearly overestimates the higher p_T components. This effect is

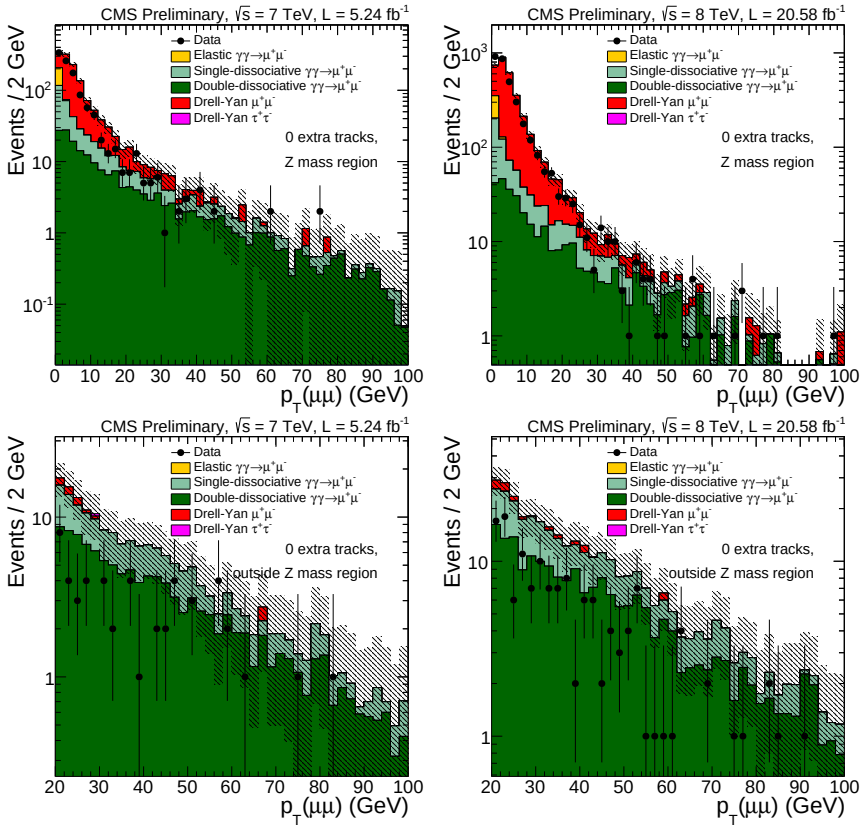

Figure 3.7: Outgoing leptons' transverse momentum distributions at $\sqrt{s} = 7$ and 8 TeV inside (top figures) and outside (bottom figures) the Z peak region.

also observed if this exclusive skim is divided into a Z-enriched and a Z-suppressed regions through a dilepton invariant mass cut. The two regions are shown in Fig. 3.7, with a closeup to the higher-p_{T} regions suppressing most of the elastic $\gamma\gamma \to \ell^+\ell^-$ contributions for the latter.

One can therefore see this effect is related to the inelastic contribution of the total $\gamma\gamma \to \ell^+\ell^-$ prediction, the regions dominated by the inclusive Drell-Yan contribution being reasonably reproduced in data.

Looking at the high momentum limit of this exclusive dilepton pair selection, one may notice the biggest contribution to the total cross section in this region is given by the dissociative components of the $\gamma\gamma \to \ell^+\ell^-$ signal, the elastic contribution being mostly suppressed by the $\sim 1/Q^2$ behaviour of the associated form factors (Eqs. (1.5)).

Furthermore, one may return to the geometrical interpretation of this Q^2 energy transfer, already developed in section 1.2.2. Indeed, a large transfer can be pictured as a short distance scattering in terms of the impact parameter for the two incoming protons/partons building the central system. In particular, the double-dissociative component allows to probe with a very short distance of approach the parton structure of both the incoming protons.

Consequently, given the enhanced parton dynamics triggered by this large virtuality exchange, the survival factor is dropping significantly, in particular in the double-dissociative case where this impact parameter is minimal. One may therefore consider that any theoretical prediction in which this rescattering is not taken into account, is expected to overestimate this dissociative component at high-Q^2 (linked to the high-$p_{\mathrm{T}}(\mu\mu)$ values in this exclusive dilepton case), and in particular for the double dissociative case highly dependent on these effects.

This effect is particularly visible when a tighter selection emphasising the dissociative and inelastic events is applied. The discriminating variable of interest here is the dilepton invariant mass. It was chosen to restrict it to a lower limit $m(\mu\mu) > 120$ GeV. As pictured in Fig. 3.8 for the invariant mass and transverse momentum distributions in the lepton pair system, a relative compatibility can be observed between the data collected both at $\sqrt{s} = 7$ and 8 TeV, and a large suppression of the double-dissociative component of the signal at high energies.

Hence, given the lack of a proper modelling for the high-momentum component of the $\gamma\gamma \to \ell^+\ell^-$ semi-exclusive and dissociative signal, it was decided to rely on a data-driven method to account for the mis-computation of all dissociative parts of this two-photon signal.

The next section introduces another data-driven technique to rescale the fully elastic contribution of any simulated CEP, as a mean to include in this simulation the inelastic and dissociative components.

3.1.3 *Proton dissociation factor*

Since the full final state including both the outgoing protons cannot be observed using only the central detector and its limited η coverage, the observation of a central state may either originate from the fully elastic, or any of the two dissociative contributions allowed in a symmetric pp collider.

Therefore, one may introduce a scaling to apply on each elastic simulated component to be able to compare it with the full range of final states observed in this colliding experiment. One may introduce the F-factor for any of the elastic production channels. It is defined as:

$$F = \left. \frac{n^{\mathrm{data}} - n^{\mathrm{MC}}_{\mathrm{incl.bck.}}}{n^{\mathrm{MC}}_{\mathrm{el.\ proc.}}} \right|_{\mathbf{\Omega}}, \tag{3.1}$$

for any sub-part $\mathbf{\Omega}$ of the full phase space to be investigated.

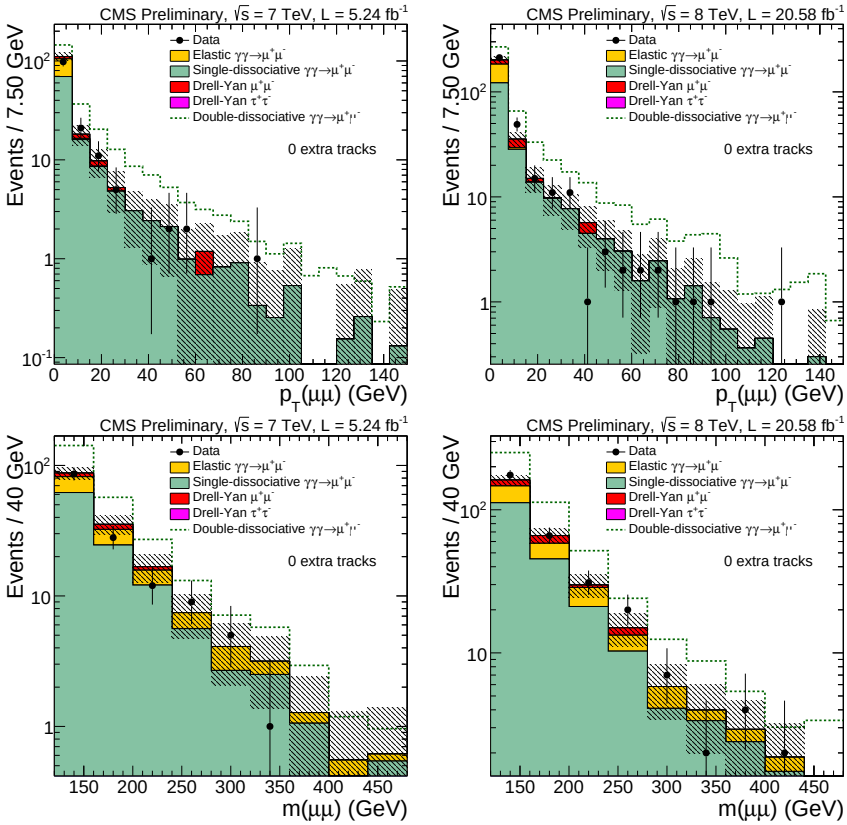

Figure 3.8: Dimuon transverse momentum and invariant mass of the exclusive dilepton selection stage (one dilepton pair with no additional tracks on vertex), in the high-mass region ($m(\mu\mu) > 120$ GeV). The double-dissociation component is the dashed line stacked on top of all other backgrounds sources.

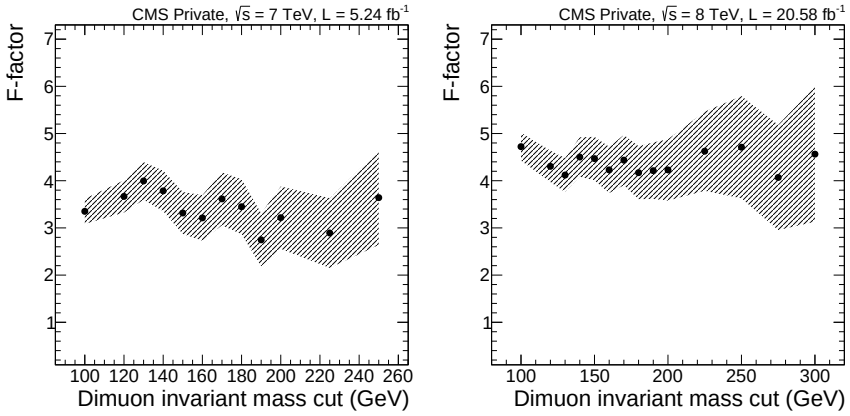

Figure 3.9: Cumulative F-factor distributions for $\sqrt{s} = 7$ and 8 TeV, as a function of the lower dilepton invariant mass cut (above the Z mass peak). The hatched bands represent the statistical error only.

As stated above, one can use the very same high statistics $\gamma\gamma \to \ell^+\ell^-$ process for any $\boldsymbol{\Omega}$ inside the observable detector acceptance. This F can hence be studied with respect to any kinematic quantity of interest, for any of the two centre-of-mass energies observed at the LHC during the last two years of its Run-1.

In Fig. 3.9, this factor is computed on the previous selection for multiple lower values of the dilepton invariant mass, as a test of its stability. It is shown to be rather stable over the full range, even though the statistical error increases with the invariant mass cut.

The major feature of this quantity is that it directly defines, for any selection of interest, an overall rescaling factor to apply on it as a manner to take the inelastic components of this process into account, given any elastic two-photon production process yield.

3.2 ANOMALOUS QUARTIC GAUGE COUPLINGS IN $\gamma\gamma \to W^+W^-$

As reported earlier, this part is mostly based on the two CMS papers[83, 84] underpinned by the two internal CMS notes [98, 99], and quoting the search for exclusive two-photon production of $W^\pm$ pairs decaying leptonically in 2011 and 2012 data at 7 and 8 TeV respectively.

A convenient way of optimising the collected statistics while keeping the many background sources under control is to use the lepton decay of both the gauge bosons, into a pair of lepton-associated (anti)neutrino. This production and decay process is pictured in Fig. 3.10.

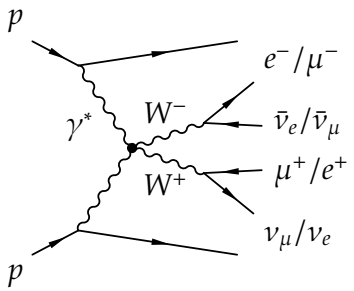

Figure 3.10: Full diagram studied within the search for $\gamma\gamma \to W^+W^-$ events performed at $\sqrt{s} = 7$ and 8 TeV. Both the two $W^\pm$ bosons decay in a pair of leptons and neutrinos. The leptons flavours have been chosen to minimise the background contamination by Drell-Yan.

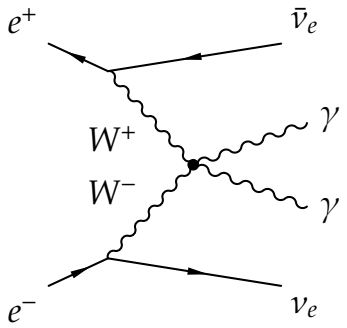

Figure 3.11: Feynman diagram showing the process studied at LEP-2 to search for anomalous quartic $\gamma\gamma W^+W^-$ couplings.

3.2.1 *Previous limits and search strategy*

The best experimental constraints on the two anomalous couplings parameters, namely a_0^W and a_C^W, were set respectively by the OPAL [61] experiment at CERN's *Large Electron-Positron* collider (LEP) and the DØ experiment [100] at the TEVATRON, the Fermilab's $p\bar{p}$ collider. The first limit was set by observing the upper limit at 95% confidence level on the production cross section for the $W^+W^- \to \gamma\gamma$ channel. The process studied, as pictured in Fig. 3.11, involved the two W bosons to arise from the two incoming electron/positron, providing two outgoing photons along with a missing transverse energy compatible with the two outgoing electron neutrinos:

$$-0.02 < a_0^W/\Lambda^2 < 0.02\ \text{GeV}^{-2},$$
$$-0.05 < a_C^W/\Lambda^2 < 0.03\ \text{GeV}^{-2},$$

with no unitarity breaking compensation (corresponding to a dipole factor set to $p = 0$, or a $\Lambda_{\text{cutoff}} \to \infty$). This lack of correction for the unitarity breaking can be easily understood knowing that the kinematic phase space associated to the energies reached at LEP's experiment is more stringent, thus giving a softer momentum to the incoming particles in the quartic gauge coupling.

The selection requires a pair of different-flavoured leptons incoming from one single vertex reconstructed using the tracking system's full information. An electron-muon pair flavour was chosen to keep a high statistics profile with a high reconstruction efficiency. It also enables to avoid the contamination by a vast majority of inclusive Drell-Yan events expected in the same-lepton channel, and clearly shown in the last section.

3.2.2 *First observation of $\gamma\gamma \to W^+W^-$ candidates*

For this search, both the 2011 and 2012 datasets collected at centre of mass energies of 7 and 8 TeV by the CMS detector were used. The first one is based on a 5.05 fb^{-1} statistics, and the second can almost count on a factor four more, *i.e.* 19.7 fb^{-1}. These two values of luminosities are corresponding to the CMS *"golden JSON"* selection of high reconstruction quality objects[5]. Both the analyses are described in details in two internal CMS documents (*analyses notes*): respectively [98] and [99].

Several sources of background are expected to give a contribution in the signal search region defined hereafter. In a decreasing order, one can quote the inclusive Drell-Yan production of tau leptons (in which the two taus decay leptonically to electron-neutrino and muon-neutrino pairs), as well as the inclusive $W^\pm$ pair production (mimicking the signal in its central final state), or the exclusive tau pair production. Among the secondary background, one can quote the diffractive $W^\pm$ pair (described in chapter 1), or the $t\bar{t}$ pair productions.

The SM $\gamma\gamma \to W^+W^-$ signal predictions for both the centre of mass energies are given by `CalcHEP`. The anomalous points are either computed by `CalcHEP` 3.4, or `MadGraph` 5. (at 8 TeV). Both the generators are giving compatible results, as expected by their shared dimension-6 matrix elements, and the EPA (see section 1.2.1) used in the photon flux estimation.

The `CalcHEP` prediction was only used in the 7 TeV part of the analysis, and its implementation by T. Pierzchała *et al.* [62] of the anomalous quartic coupling operators is defining only the four dimension-6 operators involving a two-photon production of $W^\pm$ and Z boson pairs. `MadGraph` was chosen in the 8 TeV analysis for its implementation of both the dimension-6 and 8 couplings developed in [63, 64]. One may then use `Pythia` 6 to force both the gauge bosons to decayed into an in

[5] The two datasets are even larger when considering the so-called *"muon JSONs"* that also contains runs for which one or more sub-detectors are allowed not to operate entirely. In this broader range of runs, the tracker and muon stations were still fully able to record enough information to reconstruct the muon objects. Up to 5.24 fb^{-1} were recorded this way in 2011 at $\sqrt{s} = 7$ TeV, and 20.6 fb^{-1} in 2012 at 8 TeV.

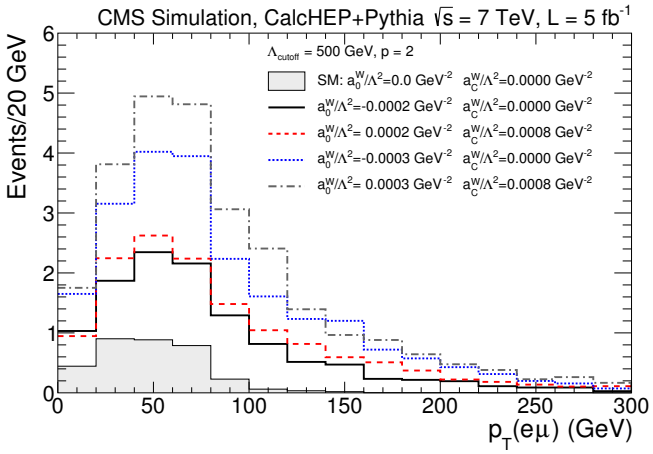

Figure 3.12: Leptons pairs transverse momentum distribution for four points in the dimension-6 AQGC phase space, as propagated within the CMS reconstruction software. The filled surface represents the standard model prediction (with both the anomalous parameters set to 0). A form factor with $\Lambda_{\text{cutoff}} = 500$ GeV is applied for the unitarity conservation of the anomalous samples. All the yields are given at $\sqrt{s} = 7$ TeV for an integrated luminosity of 5 fb^{-1}.

electron-muon pair, along with their associated neutrinos. In Fig. 3.12, the differential `CalcHEP` predictions for the main discriminating variable (the dilepton transverse momentum) is given at 7 TeV for several anomalous points (along with the SM value).

However, the two generators only implement the elastic diffusion of one photon out of the proton case into their full cross section estimation. With no information from the outgoing protons available during the whole Run-1, the events yields defining a re-scaling applied to the purely elastic signal to take into account the single- and double-dissociative cases was extracted through the *F*-factor technique described in section 1.3, for the very equivalent selection cuts applied in the preselection criteria defined below.

Furthermore, the cuts applied on the total dilepton phase space are tuned for the two-*W* production regime. The dimuon invariant mass was therefore cut below twice the on-shell $W^{\pm}$ mass, hence $m(\mu^+\mu^-) > 160$ GeV. As seen in Fig. 3.9, the rescaling factors to be applied on the 7 TeV (resp. 8 TeV) purely elastic samples is 3.23 ± 0.50 (stat.) $\pm$ 0.36 (syst.) (resp. 4.10 ± 0.43 (stat.)).

In computing this *F*-factor, the background events to be subtracted are the DY production of two leptons. These leptons are either muons, or taus with a leptonic decay mode (accounting to 35.2% of all τ decays).

Selection	Remaining events 7 TeV	8 TeV
Trigger and preselection	9086	19253
$m(e\mu) > 20$ GeV	8200	18271
Leptons identification	1222	6393
Exclusivity condition	6	24
$p_T(e\mu) > 30$ GeV	2	13

Table 3.2: Summary of the all individual selection processes ("cut flow" table) leading to the $e\mu$ signal region, and yield of selected data events at $\sqrt{s} = 7$ and 8 TeV.

The baseline selection for this $e\mu$ final state (equivalent to the dimuon sample as defined above) requires an asymmetric dilepton trigger to be fired by a muon and an electron present in the event, with a minimal transverse momentum of 17 GeV (resp. 8 GeV) for the leading (resp. trailing) lepton.

In order to suppress all wrong modelling effects arising at the edge of the trigger cut, an offline cut at $p_T(\ell) > 20$ GeV was also introduced. In addition, the low masses resonances (such as the J/ψ and $\Upsilon(1s, 2s, 3s)$) region of the same-sign dilepton production was filtered out by an invariant mass cut: $m(e\mu) > 20$ GeV. This latter selection enables to suppress the higher fake lepton identification probability enhanced in this region.

The lepton quality was furthermore tightened through a *tight muon* (described above and in section 2.4.2) and a *medium electron* identification criteria.

Both the electron and muons tracks are finally requested to be matched to one single primary vertex with no additional tracks (exclusivity condition).

The complete summary of the selection efficiencies in the two data collections is detailed on table 3.2.

Finally, the last part in the selection is requiring the dilepton system to exceed a given transverse momentum. To understand why both the standard model and anomalous signal predictions are enhanced in a higher value of this quantity (as previously pictured in Fig. 3.12), one must see its direct correlation with the two-outgoing neutrinos (produced from the $W^{\pm}$ decays along with the leptons) energy, pictured in Fig. 3.13. However, given the very high instantaneous luminosity (hence pileup multiplicity) delivered during the two data acquisition periods, it is challenging to rely on this $\not{E}_T$ for one single primary interaction in the event. Therefore, the dilepton transverse momentum remains the best selection variable.

This un-cut transverse momentum distributions at $\sqrt{s} = 7$ and 8 TeV is pictured in Fig. 3.14, with all other cuts as defined above applied. The 7 TeV, lhs. figure, also quotes the prediction for the two anomalous coupling working points $(a_0^W/\Lambda^2, a_C^W/\Lambda^2) = (2 \times 10^{-4}, 0)$ and $(-2 \times 10^{-4}, -8 \times 10^{-4})$.

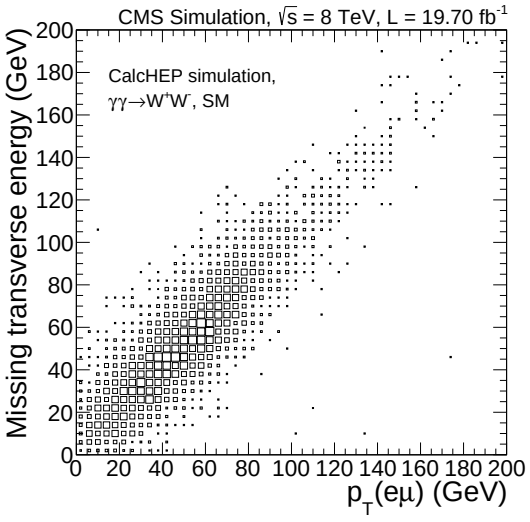

Figure 3.13: Correlation between the dilepton transverse momentum distribution and the missing transverse energy observed in the event for the standard model prediction at $\sqrt{s} = 8$ TeV of the $\gamma\gamma \to W^+W^-$ process decaying leptonically.

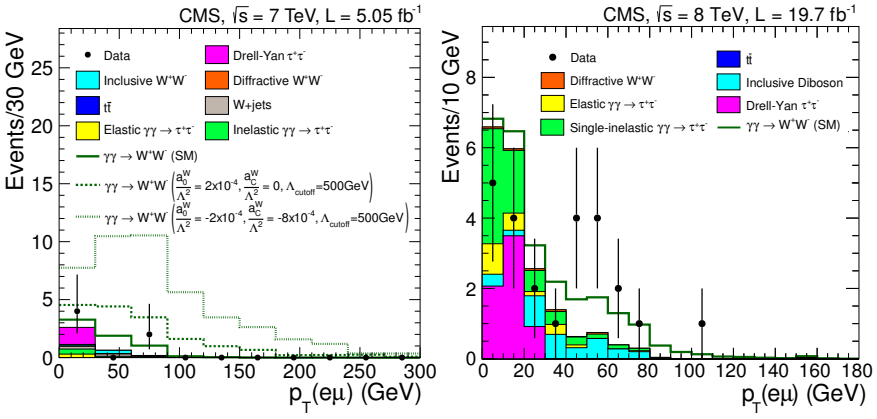

Figure 3.14: Leptons pair transverse momentum distributions, signal region (but this very distribution), for the $\sqrt{s} = 7$ and 8 TeV analyses described in the text.

Two signal selections were introduced in the two analyses. They were either defined to enhance the SM contribution ($p_T(e\mu) > 30$ GeV in both the studies), or to set evidence to the region where the anomalous signals contribute the most. For the 2011 analysis, this latter region was defined as $p_T(e\mu) > 100$ GeV, while the higher-statistics 2012

Region	$\sqrt{s}$	Background	$\gamma\gamma \to W^+W^-$	Data
$\gamma\gamma \to \tau^+\tau^-$	7 TeV	2.6 ± 0.8	0.7	4
	8 TeV	11.3 ± 2.5	1.4	11
DY $\tau\tau$	7 TeV	256.7 ± 10.1	0.3	182
	8 TeV	999.4 ± 27.0	1.5	771
Incl. W^+W^-	7 TeV	46.2 ± 1.7	1.0	43
	8 TeV	228.6 ± 7.8	5.4	214

Table 3.3: Summary of backgrounds and signal contributions in the three sideband regions defined in the text, along with the observed yields in data collected at $\sqrt{s}$ = 7 and 8 TeV.

analysis used a restricted region ($30 < p_{\mathrm{T}}(e\mu) < 130$ GeV) to estimate the fiducial cross section in this range.

As a mean to control the proper modelling of all dominant background components in the signal region, three "natural" sideband regions can be defined using the p_{T} and tracks multiplicity distributions:

- an exclusive $\gamma\gamma \to \tau^+\tau^-$ region, with no extra tracks and $p_{\mathrm{T}}(e\mu) < 30$ GeV, where the low p_{T} value is expected from the τ decays (producing invisible neutrinos in the process),
- an inclusive Drell-Yan ($\tau^+\tau^-$) region, with $1 < n^{\mathrm{extra}}_{\mathrm{tracks}} < 6$ and $p_{\mathrm{T}}(e\mu) < 30$ GeV, and
- an inclusive W^+W^- region, with $1 < n^{\mathrm{extra}}_{\mathrm{tracks}} < 6$ and $p_{\mathrm{T}}(e\mu) > 30$ GeV, where the higher tracks multiplicity is expected from the underlying event arising from this production.

The upper limit on the tracks multiplicity is introduced to reduce the contamination by $t\bar{t}$ and multi-jets backgrounds in these regions.

A relatively good agreement is observed in the three sideband regions, as detailed in table 3.3. The major discrepancy comes from the DY dominated region in which a 25 – 30% excess in the MC prediction is seen. This region is estimated to contain 87% of this inclusive $\tau\tau$ background (as estimated in the 8 TeV analysis). The latter being almost fully suppressed in the signal region, a rescaling of its contribution was propagated there for consistency.

Looking again at the broader picture, all control distributions are showing a reasonable agreement with the theoretical predictions. If one relaxes the track-based exclusivity condition while retaining the lower p_{T} cut of 30 GeV, this extra tracks multiplicity on the dilepton vertex distribution shown in Fig. 3.15 is correctly modelled at both the centre of mass energies.

One may therefore have a first look at the SM signal search window. For this selection, the dilepton invariant mass is shown in Fig. 3.16.

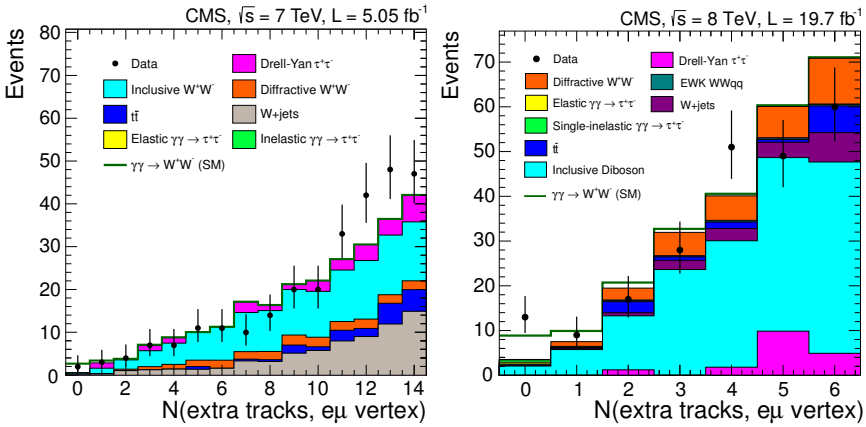

Figure 3.15: Multiplicity of extra tracks on the dilepton vertex, with $p_T(e\mu) > 30$ GeV. The first plot is for $\sqrt{s} = 7$ TeV, while the second is at 8 TeV. The first bin (no extra tracks on dilepton vertex) defines the exclusive signal search region.

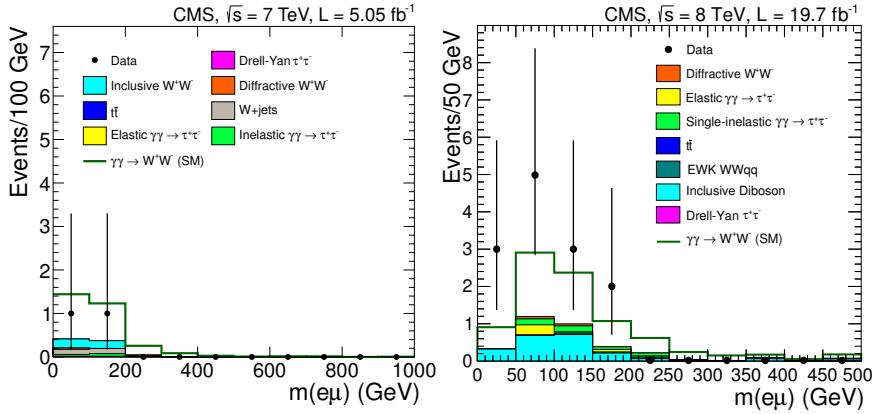

Figure 3.16: Signal region leptons pair invariant mass distributions, for the $\sqrt{s} = 7$ and 8 TeV analyses described in the text.

As seen on table 3.2, two events are passing the $\sqrt{s} = 7$ TeV criteria, and 13 for the 8 TeV analysis. Among the 13 candidates observed at $\sqrt{s} = 8$ TeV, two are displayed on Figs. 3.17 and 3.18. The latter set is zoomed over the dilepton primary vertex, and its surroundings. The very noisy pileup environment can be appreciated from the high tracks multiplicities (green lines), along with the number of primary vertices (yellow dots) seen in the two event displays.

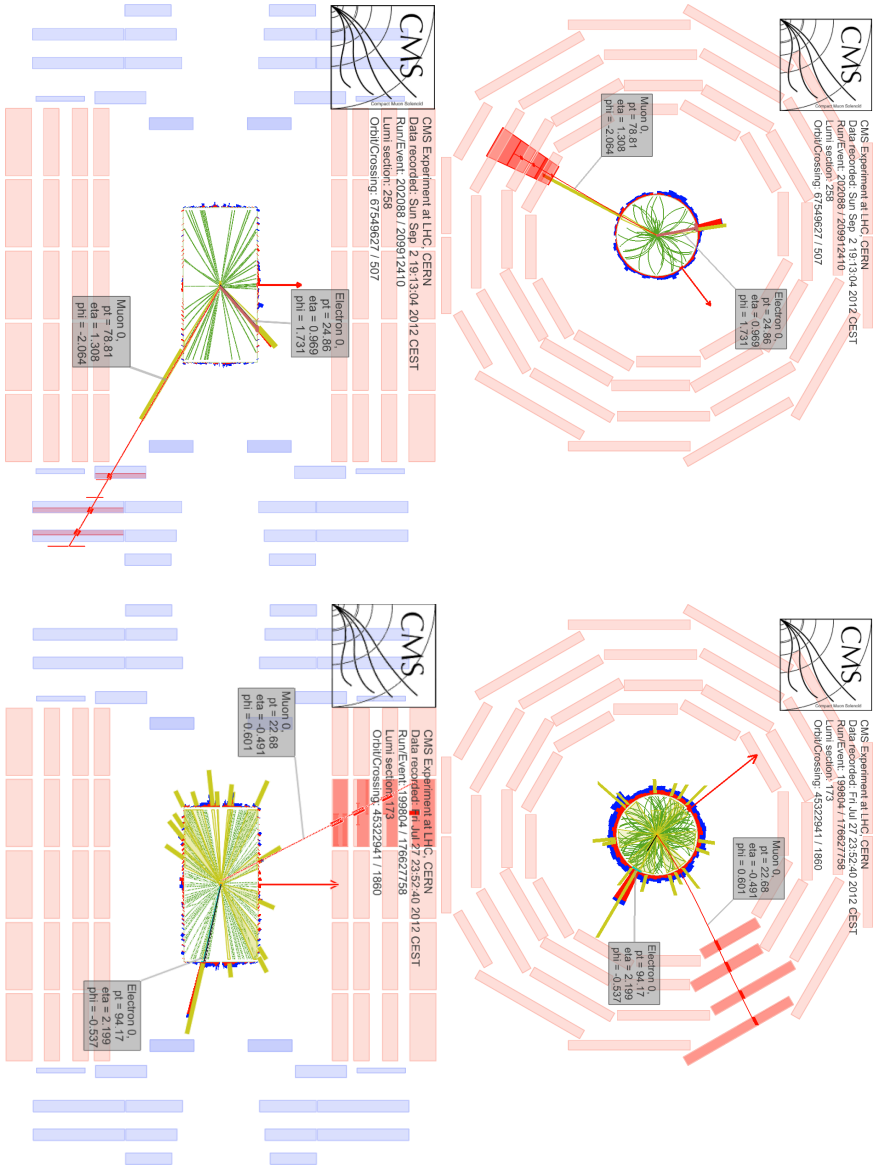

Figure 3.17: Event displays in the $r-z$ and $r-\phi$ planes of two $\gamma\gamma \to W^+W^- \to e\mu\nu\bar{\nu}$ candidates selected in the 2012 data analysis at 8 TeV. The red (resp. blue) lines stand for the muon (resp. electron) track candidates.

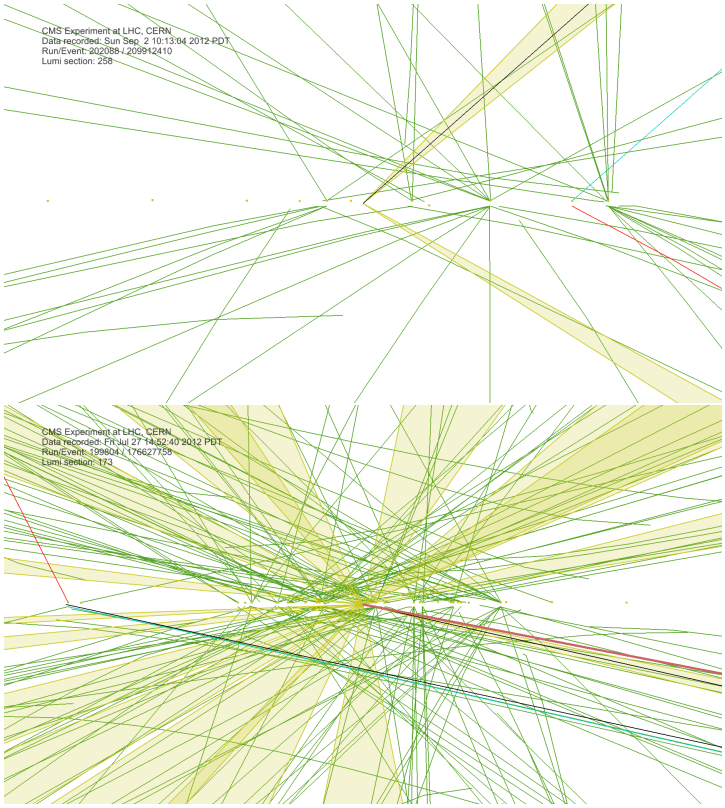

Figure 3.18: Closeup to the primary vertex region of the two event displays shown in Fig. 3.17. The red (resp. blue) lines stand for the muon (resp. electron) track candidates.

Before quoting the total observed cross sections in the two centre of mass energies, on needs to identify all sources of systematic errors decreasing the sensitivity of the two analyses.

The major systematic uncertainty is given by the proton dissociation factor. Its scope is related to the coarser modelling through the EPA of the photon emissions by protons in the $\gamma\gamma \to W^+W^-$ signal search region. To compute it, one needs to combine in quadrature both the statistical error extracted from the F-factor computation seen above (respectively, 15.5% and 9.2% for the two analyses), and the systematic error observed in comparing the `LPAIR` (full matrix element) and `CalcHEP` (EPA) predictions in their $\gamma\gamma \to \ell^+\ell^-$ prediction in the high mass dimuon range ($m(\mu\mu) > 160$ GeV). This latter difference was found to range at the order of 5% at $\sqrt{s} = 7$ and 8 TeV.

The other sources are respectively the pileup dependence for the first analysis (arising from the data/simulation disagreement observed in the elastic selection of $\gamma\gamma \to \mu^+\mu^-$ events), and corrected through this "zero-bin" scaling factor (introducing a lower statistical error of 5%, as it was determined using both the dimuon and dielectron channels).

One can also quote the trigger and single lepton identification uncertainties, extracted from the differences observed between data and simulation in $Z \to \ell^+\ell^-$ control samples, or the overall error on the integrated luminosity, as determined by the accelerator machine parameters scan[93].

All systematic uncertainties sources are listed in the table 3.4. Their combined effect is respectively 19.7 and 12.1% for the two centre of mass energies.

Systematics	Uncertainty (%) 7 TeV	8 TeV
Trigger and leptons ident.	4.2	2.4
Integrated luminosity	2.2	2.6
Proton dissociation factor	16.3	10.5
Vertexing efficiency	1.0	
Pileup dependence	10.0	
Efficiency corr. (excl. condition)		5.0
Total	19.7	12.1

Table 3.4: Summary of all systematic uncertainties on the $e\mu$ selection baselines at both the 7 and 8 TeV centre of mass energies.

As shown in Fig. 3.12 the transverse momentum of the outgoing leptons, as decay products of the $W^\pm$ bosons, represents a good lever arm to probe for anomalous quartic gauge couplings, as the higher energy contributions are suppressed in the standard model prediction, and the total total production cross section is reduced. Hence, at lower sample luminosities a simple event-counting operation can extract a two-dimensional constraint on the anomalous couplings. The observed events numbers at 7 and 8 TeV, along with the predicted background and signal components, are detailed in table 3.5.

Therefore, given all systematic and statistical uncertainties sources on both the signal and background components, one can compute the local significance of the $2 + 13$ candidates observed in the two fully independent datasets.

For the $\sqrt{s} = 7$ TeV part, one can extract a 0.8σ (resp. 1.8σ) observed (resp. expected) excess with respect to the background-only hypothesis. The 8 TeV data, with their 13 candidates, are slightly more meaningful. They reach an observed (resp. expected) excess of 3.6σ (resp. 2.3σ) above the background hypothesis. Combining

	Kinematic region		
	$p_T(e\mu) > 30$ GeV		$p_T(e\mu) > 100$ GeV
$\sqrt{s}$	7 TeV	8 TeV	7 TeV
Exp. signal	2.2 ± 0.4	5.3 ± 0.1	0.14 ± 0.02
Exp. background	0.84 ± 0.15	3.5 ± 0.5	
Observed data	2	13	0

Table 3.5: Observed exclusive $\gamma\gamma \to W^+W^-$ candidates for the full dataset collected in 2011 and 2012 by the CMS experiment, along with the theoretical predictions for the two search regions defined in the text.

both significances, one may claim an *evidence* for the two-photon production of $W^\pm$ pairs at 3.7σ, with an expected significance of 2.9σ.

A 95% confidence level limit on the production cross section at 7 TeV is then set using the *Feldman-Cousins* method[101], namely for the quartic gauge couplings signal region where the outgoing lepton pair's transverse momentum is bounded by $p_T(\mu^\pm e^\mp) > 100$ GeV:

$$\sigma_{(7\text{ TeV})}\left(pp \to p^{(*)}(\gamma\gamma \to W_1^+W_2^-)p^{(*)}\right) \times \\ \times \mathcal{B}\left(W_{1,2}^\pm \to e^\pm\nu_e/\mu^\pm\nu_\mu\right) < 1.9 \text{ fb},$$

with a central value of $2.2^{+3.3}_{-2.0}$ fb and a predicted SM cross section of 4.0 ± 0.7 fb.

For the higher-statistics 8 TeV data, 13 candidates were observed at $p_T(\mu e) > 30$ GeV, hence 3.6σ above the background-only prediction. It can be used to extract the total cross section for this process:

$$\sigma_{(8\text{ TeV})}\left(pp \to p^{(*)}(\gamma\gamma \to W_1^+W_2^-)p^{(*)}\right) \times \\ \times \mathcal{B}\left(W_{1,2}^\pm \to e^\pm\nu_e/\mu^\pm\nu_\mu\right) = 12.3^{+5.5}_{-4.4} \text{ fb},$$

with a SM prediction of 6.9 ± 0.6 fb.

Therefore, the two observations are compatible (within uncertainties) with the standard model predictions at the two centre of mass energies.

3.2.3 *New constraints on AQGCs*

Given the upper limit set on the production cross section for the exclusive two-photon production of $W^\pm$ pairs at $\sqrt{s} = 7$ and 8 TeV extracted in the previous section, the parameters space for the W sector of the anomalous quartic gauge couplings can be restricted to a tighter set of constraints.

	Λ_{cutoff}	Form factor 500 GeV			Form factor ∞ (no FF)		
	$\sqrt{s}$	7 TeV	8 TeV	Comb.	7 TeV	8 TeV	Comb.
Dim-6	a_0^W/Λ^2	±1.5	$^{+1.0}_{-1.1}$	$^{0.9}_{-1.0}$	±4.0	±1.2	±1.2
	a_C^W/Λ^2	±5.0	$^{+3.4}_{-4.2}$	$^{3.1}_{-3.7}$	±15	±4.4	±4.2
		$\times 10^{-4}$ GeV^{-2}			$\times 10^{-6}$ GeV^{-2}		
Dim-8	$f_{M,0}/\Lambda^4$	±5.7	$^{+4.2}_{-3.8}$	$^{3.8}_{-3.4}$	±15	±4.6	±4.6
	$f_{M,1}/\Lambda^4$	±19	$^{+13}_{-16}$	$^{12}_{-14}$	±57	±17	±16
	$f_{M,2}/\Lambda^4$	±2.8	$^{+2.1}_{-1.9}$	$^{1.9}_{-1.7}$	±7.6	±2.3	±2.3
	$f_{M,3}/\Lambda^4$	±9.5	$^{+6.4}_{-8.0}$	$^{5.9}_{-7.0}$	±28	±8.3	±8.0
		$\times 10^{-10}$ GeV^{-4}			$\times 10^{-12}$ GeV^{-4}		

Table 3.6: 95% confidence level parameters limits at $\sqrt{s}$ = 7, 8 TeV, and with the two centre of mass energies combined, for the dimension-6 and 8 AQGC operators, and for the two $\gamma\gamma \to W^+W^-$ searches conducted at the CMS experiment.

With the limits extracted on the observed cross sections at 7 and 8 TeV, tight boundaries can be set to the dimension-6 and 8 anomalous parameters described in section 1.4.1. This property arises from the strict relation between the parameters and the overall production cross section of this very process. A scan of the allowed parameters space was therefore performed, with each working point propagated through the CMS simulation and reconstruction algorithms to extract an observation yield.

The result of this parameters scan, along with the observed cross sections quoted above is therefore setting the limits on the anomalous parameters, as displayed in table 3.6. A visual representation of the 95% C.L. constraints is also pictured in Fig. 3.19 for the two dimension-6 parameters. On the left figure, the sensitivity improvement with respect to the previous OPAL constraints at LEP can be directly appreciated once this ellipse is drawn along with the 7 TeV only result.

On the right figure, one can see a closeup of the limits at both the centre of mass energies, along with the combined 7 + 8 TeV results. The one-dimensional limits are also pictured on this second figure. They correspond to the case where one of the anomalous parameter is varied while the other is constrained to 0, its SM value. Thus, their dynamic range is slightly tighter than the two-dimensional limits, as shown on this figure.

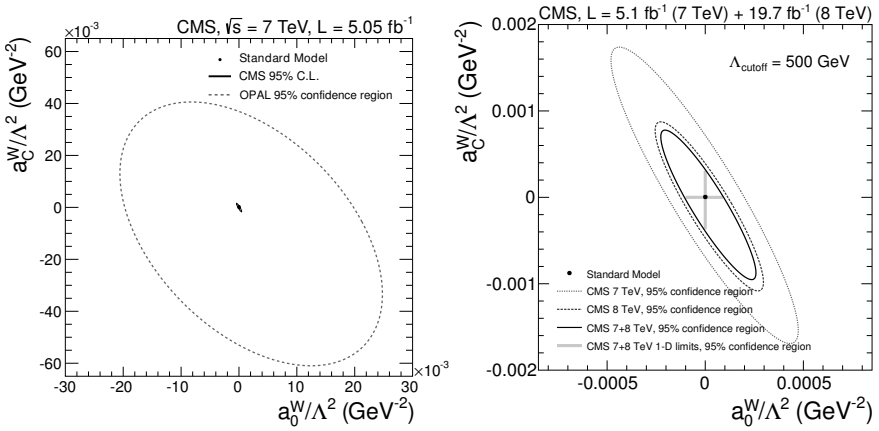

Figure 3.19: Limits on two anomalous parameters for the quartic gauge couplings probe, at $\sqrt{s}$ = 7 and 8 TeV, and combination for both centre of mass energies. The lhs. figure shows the improved sensitivity between the former OPAL constraints (light dashed line), and the $\sqrt{s}$ = 7 TeV results (black solid line) On the rhs. figure, the one-dimensional limits (limits on one parameter while cancelling the other one) are also shown with bold grey lines.

For the sake of completeness, one can also quote two purely inclusive analyses leading to an increased sensitivity to the anomalous behaviours with respect to the previous LEP limits.

First, in the beginning of May 2013, the Dø Collaboration (Fermilab) released a search for inclusive dielectron produced along with a photon in $p\bar{p}$ collisions at $\sqrt{s}$ = 1.96 TeV [100]. This enabled to perform a simple resonance-like search, while looking at the invariant mass tails for any shape and yield discrepancy.

Secondly, a set of inclusive analyses were performed in the "Standard model physics" group in CMS, studying anomalous quartic gauge couplings through the experimental determination of several production cross sections sensitive to such anomalies, as for instance the evidences for the $W^{\pm}V\gamma$ [102] and the $Z\gamma$ [103], or the same-sign $W^{\pm}$ pair production [104].

While the second reached the same order of magnitude with respect to the strategy quoted here, the first remained between LEP and LHC sensitivities. A summary of all LHC studies (including the inclusive ones listed above, labelled "$WV\gamma$" and "ss WW" respectively) on anomalous quartic gauge couplings is shown in Fig. 3.20 for the dimension-8 parameters constraints. All the limits in this table are quoted without any unitarity-restoring form factor.

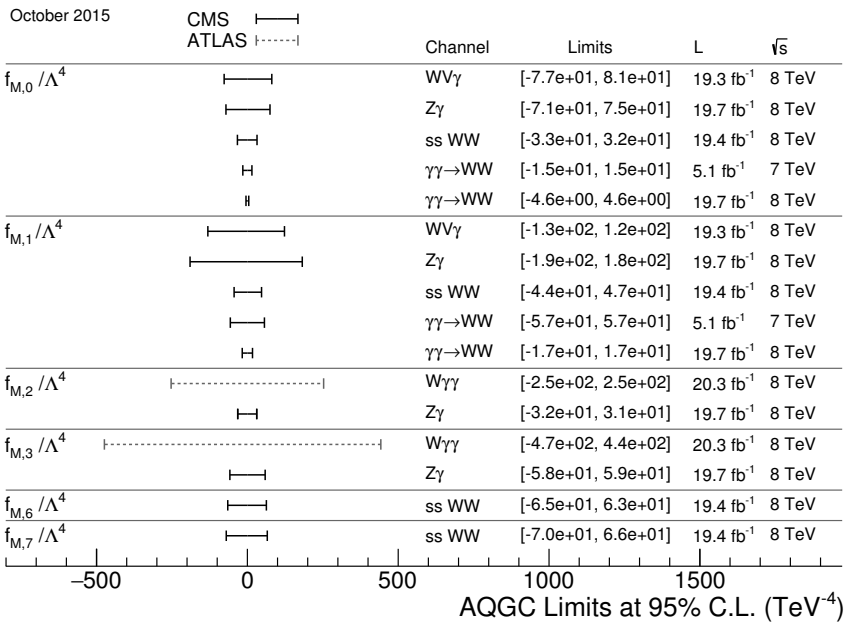

Figure 3.20: Combined 95% C.L. limits on the dimension-8 operators involved in AQGCs, as extracted from LHC analyses in CMS and ATLAS. To enable the comparison, no form factors are applied (*i.e.* $\Lambda_{\text{cutoff}} \to \infty$). Figure from [105].

To summarise, this experimental search for the two-photon production of $W^{\pm}$ gauge boson pairs at the LHC enabled to:

- observe the first ever candidates for this rare interaction, namely 2 + 13 events with an expected background contribution of 0.84 ± 15 and 3.5 ± 0.15 at $\sqrt{s} = 7$ and 8 TeV respectively,
- set limits on the anomalous quartic gauge couplings orders of magnitude more stringent than the former state of the art.

For the last point, one may quote that the limits extracted by this technique were still unequalled by any inclusive or exclusive probe while writing this thesis, thus in the last months of 2015.

3.3 ANOMALOUS QUARTIC GAUGE COUPLINGS IN $\gamma\gamma \to ZZ$

If one looks back to the Eq. (1.8), one can notice two remaining terms to this linear combination of dimension-6 operators. These two terms are providing a finite contribution to the anomalous $\gamma\gamma ZZ$ coupling, for which the fully SM contribution can be neglected.

Indeed, at the leading order this purely neutral exchange is fully suppressed (as an effective neutral coupling, it is strongly suppressed through the GIM mechanism), and the NLO contribution reaches 0.041(1) fb, as evaluated using `MadGraph5-MC@NLO` [106]. As described in section 1.2, several BSM frameworks predict such a neutral coupling to be reachable at LHC energy scales. In an analysis note released within the CMS Collaboration, [107], the exploratory search for the anomalous couplings is described in details.

3.3.1 *Motivations for $\gamma\gamma ZZ$ couplings studies*

As seen in [23], the only contributions involving a light Higgs boson along with this quartic tree-level $\gamma\gamma ZZ$ coupling are involving on dimension-8 operators at least. If one neglects the Higgs interactions, one can still count on dimension-6 operators directly equivalent to the dimension-6 scheme developed to probe the $\gamma\gamma W^+W^-$ coupling.

The actual limits on the anomalous behaviour are still provided by the LEP-2 combination performed a decade ago [108], and a large sensitivity to this process through the two-photon production mechanism is expected at the LHC [62].

In its high multiplicity of decays channels, the Z boson provides several final states which can be observed at the LHC for the $\gamma\gamma \to ZZ$ process. For instance, considering the notation $\gamma\gamma \to Z_1 Z_2$:

- $Z_1 \to \ell^+\ell^-$, $Z_2 \to \ell'^+\ell'^-$,
- $Z_1 \to \ell^+\ell^-$, $Z_2 \to \nu_{\ell'}\bar{\nu}_{\ell'}$,
- $Z_1 \to \nu_{\ell'}\bar{\nu}_{\ell'}$, $Z_2 \to \nu_{\ell'}\bar{\nu}_{\ell'}$,

and if the hadronic decay modes are included:

- $Z_1 \to \ell^+\ell^-$, $Z_2 \to \mathrm{jj}$,
- $Z_1 \to \nu_\ell\bar{\nu}_\ell$, $Z_2 \to \mathrm{jj}$,
- $Z_1 \to \mathrm{jj}$, $Z_2 \to \mathrm{jj}$

Since the exclusivity condition implies the central system to remain with a low tracking activity, the jets final state is expected to provide a low signal-to-noise ratio. Indeed, for a proper jet reconstruction in the central detector, a higher tracks occupancy is to be observed, thus making it difficult to rely on the overall track multiplicity on each vertex of interest. This is particularly expected in a high pileup environment as observed in the high luminosity runs at the LHC.

Hence, in an attempt to maximise the output for this study, the leptonic Z decays were the only ones considered there. Furthermore, since the neutral Z decay is occurring on all three neutrinos families, the branching fraction of this channel is three times higher than the fully leptonic decay (four leptons).

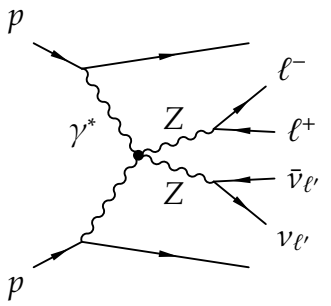

Figure 3.21: Full diagram studied within the search for $\gamma\gamma \to ZZ$ events performed at $\sqrt{s} = 7$ and 8 TeV. One of the two Z bosons decays in a same-flavour lepton pair, while the second decays in the invisible two-neutrino final state.

The decay channel of interest is then $\gamma\gamma \to ZZ \to \ell^+\ell^-\nu_{\ell'}\bar{\nu}_{\ell'}$ pictured in Fig. 3.21, hence two isolated leptons, with a high associated missing energy.

Among the main background sources, one must quote the inclusive W^+W^- and ZZ productions, or *fakes*, namely any particle passing all identification criteria of the selected lepton flavour (which could be another different-flavour lepton).

The first inclusive diboson production process quoted above can provide, in the fully leptonic decay mode of both the W bosons (accounting to 10.7% of all W decays), two opposite-sign leptons along with a large transverse energy of the associated neutrinos. With the lack of knowledge on any of the two outgoing neutrinos, and their mixing in the total $\not{E}_{\mathrm{T}}$, one must suppress it through a tight dilepton invariant mass cut around the Z boson on-shell mass.

The second process is the most spurious source of background, giving rise to the very same final state if no secondary tracks arising from the fragmented proton are reconstructed in the inner tracker. The total cross section for this process within the exclusive selection as defined above is expected to give a contribution at $\sqrt{s} = 8$ TeV of 0.13 fb over the whole mass range, 0.10 fb in the Z mass region ($70 < m(\mu\mu) < 106$ GeV), and is dropping to half its value above a dilepton p_{T} threshold of 50 GeV. Hence, it can safely be neglected as a potential background in the high-p_{T} search region.

3.3.2 *Simulation scheme*

Since the additional terms are already present in the dimension-6 phenomenological Lagrangian quoted above, one could benefit from its implementation already done in `CalcHEP` by Pierzchała *et al.* [62]. It is hence the very same simulation process as the one used for the $\gamma\gamma \to W^+W^-$ studies.

In Fig. 3.22 one can see the tree level anomalous cross sections (without any gauge boson branching fractions applied) expected at $\sqrt{s} = 7$, 8, and 13 TeV for a wide range

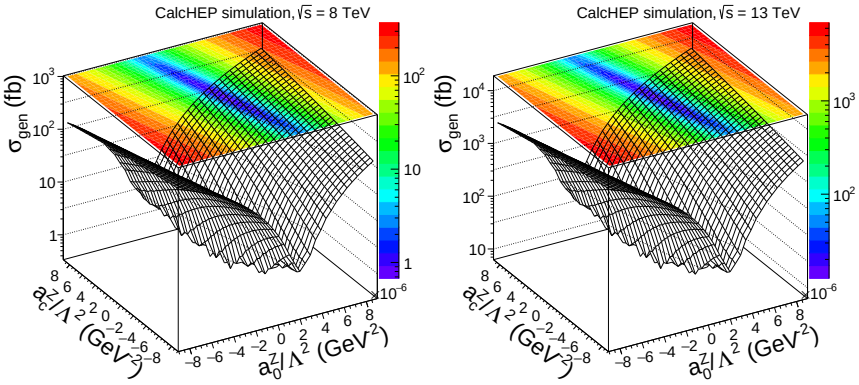

Figure 3.22: Elastic `CalcHEP` predictions at $\sqrt{s} = 8$ and 13 TeV of the generation level cross sections for the $\gamma\gamma \to ZZ$ anomalous quartic gauge couplings. No branching ratio nor form factors are applied on the cross sections (*i.e.* $\Lambda_{\text{cutoff}} \to \infty$). The horizontal axes are quoting the values of the two anomalous parameters in units of 10^{-6} GeV^{-2}.

of dimension-6 couplings. Unlike the $\gamma\gamma \to W^+W^-$ channel, the predictions are fully symmetric with respect to $(a_0^Z, a_C^Z) = (0,0)$, *i.e.* $\sigma(-a_0^Z, -a_C^Z) = \sigma(a_0^Z, a_C^Z)$. Additionally, they only quote the elastic production of the two incoming photons. Therefore, one needs to apply the very same recipe as developed for the $\gamma\gamma \to W^+W^-$ study to rescale the yields and take into account the single- and double-dissociation scenarios to be expected without any forward proton tagging.

Furthermore, no form factors have been included in the predictions. Hence, the physical cross sections are expected to be orders of magnitude lower than the yields, depending on the energy cutoff scale Λ_{cutoff} chosen. In table 3.7, an almost linear correspondence to the cross sections, with and without this form factor included, can be observed.

The anomalous samples were generated by `CalcHEP`, using the same implementation of anomalous triple and quartic gauge couplings as for the W^+W^- analysis described earlier. The leptonic and neutral decays of both the Z bosons were performed by `Pythia` 6, relying on the `CTEQ6` PDF description [109]. Their experimental signatures in the CMS detector have been simulated through `FastSim`, its fast simulation tool described in [110].

All the simulations are reweighted to the pileup distribution observed during the 2012 data taking period at $\sqrt{s} = 8$ TeV, hence with a mean number of primary interactions $\mu = 21$.

Anom. parameter		σ_{prod} (fb)	
a_0^Z/Λ^2	a_C^Z/Λ^2	$\Lambda_{\text{cutoff}} \to \infty$ (no FF)	$\Lambda_{\text{cutoff}} = 500$ GeV
5×10^{-6}	0	0.76	0.12×10^{-3}
1×10^{-5}	0	3.04×10^{3}	0.43×10^{-3}
5×10^{-5}	0	7.58×10^{3}	1.04
0	1×10^{-5}	0.22	5.88×10^{-3}
0	5×10^{-5}	0.54×10^{3}	14.81
0	1×10^{-4}	2.16×10^{3}	59.23

Table 3.7: Production cross section (with no Z decay branching ratio applied) as computed using `CalcHEP` in the $\gamma\gamma \to ZZ$ process, with and without the form factor unitarity restoration technique applied, and for several anomalous parameters values.

As for the $\gamma\gamma \to W^+W^-$ study, the main observable of interest to discriminate the standard model prediction from to any anomalous point is the dilepton transverse momentum. In Fig. 3.23, one sees the effect of the lowest momentum threshold to be required, on the main sources of background contamination. The first figure quotes the full invariant mass spectrum above low-mass resonances, *i.e.* $m(\mu\mu) > 20$ GeV. The latter is furthermore selecting the Z mass region ($70 < m(\mu\mu) < 106$ GeV), where most of the anomalous signals contribution resides.

A F-factor of 4.10, corresponding to the rescaling used in the $\gamma\gamma \to W^+W^-$ analysis, and compatible with the one observed in the mass range of two Z on shell ($2\times M_Z \simeq 180$ GeV), was applied on both the $\gamma\gamma \to W^+W^-$ and anomalous $\gamma\gamma \to ZZ$ elastic samples.

In these two figures, neither the individual background nor the signal contributions are stacked. A total inelastic background prediction is however quoted as a thin black line, combining all the inclusive and inelastic contributions.

The major contribution to the highest values of the $p_T(\mu\mu)$ spectrum is given by the single- and double-dissociative part of the $\gamma\gamma \to \mu^+\mu^-$ signal. However, as already mentioned in section 3.1.3, the modelling of such contribution needs to be handled with care at this two-photon energy range. As a consequence, as shown in the next section, another data-driven technique can be introduced to extract a better description of this region of the phase space.

3.3.3 *Dissociative high-p_T suppression*

Given the deficit of data observed with respect to the theoretical predictions given in a high-$p_T(\ell\ell)$ region already mentioned earlier in this thesis, one may define a technique to re-tune the dominant inelastic contributions to the total two-photon process through the data-driven extraction of the expected yield in this energy range.

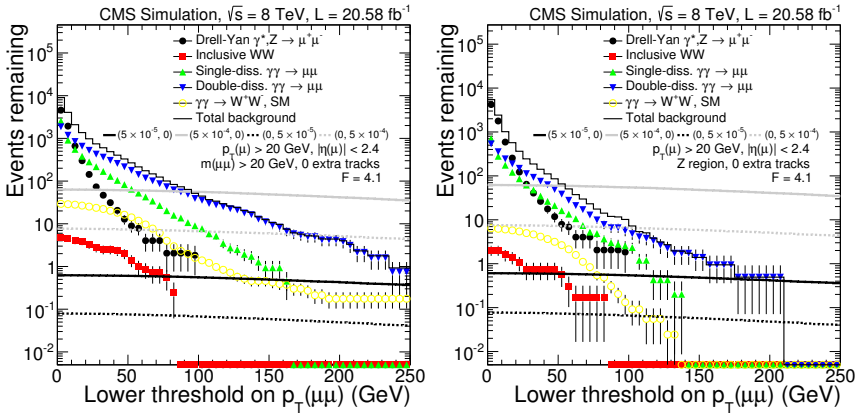

(a) For $m(\mu\mu) > 20$ GeV

(b) For $70 < m(\mu\mu) < 106$ GeV

Figure 3.23: Expected remaining number of signal and main backgrounds events at $\sqrt{s} = 8$ TeV in the signal region, with respect to the dilepton transverse momentum lower cut applied. The dilepton invariant mass range is given under the figures. The $\gamma\gamma \to ZZ$ signal predictions are quoted with the "F-factor" re-scaling as extracted in the $\gamma\gamma \to W^+W^-$ analysis.

In order to quantify this yield, it was chosen to rely on two sideband regions around the signal invariant mass selection, hence the lower $50 < m(\mu\mu) < 70$ GeV and the upper $m(\mu\mu) > 106$ GeV domains.

For the two regions, one can introduce an inelastic data subset as:

$$n^{\text{data}}_{\text{inel}} = n^{\text{data}} - n^{\text{MC}}_{\text{el. } \gamma\gamma\to\ell^+\ell^-} - n^{\text{MC}}_{\text{incl.bck.}},$$

hence subtracting from the observed data in this range the simulated yields for both the fully exclusive $\gamma\gamma \to \ell^+\ell^-$ contribution, and the inclusive background sources.

One can therefore extrapolate the behaviour of this quantity in both the sideband regions defined above, using a template (exponential) fit performed over a variable of interest. Following the strategy defined in this study, this variable was chosen to be the dilepton transverse momentum. It is hence directly linked to the two-photon centre-of-mass energy.

In Fig. 3.24 and table 3.8, the result of the two fits are given, using the $n(p_{\text{T}}) = a \cdot e^{-b \cdot p_{\text{T}}}$ template, with $p_{\text{T}} = p_{\text{T}}(\mu\mu)$.

Then, one may interpolate the Z mass region yield using the arithmetic mean of the two values extracted in the sideband regions. Therefore, this latter operation is less sensitive to any mis-modelling of the dominant inclusive source of background for this quantity in this mass range, *i.e.* the Drell-Yan production of muon pairs, being evaluated using a selection where its component is reduced.

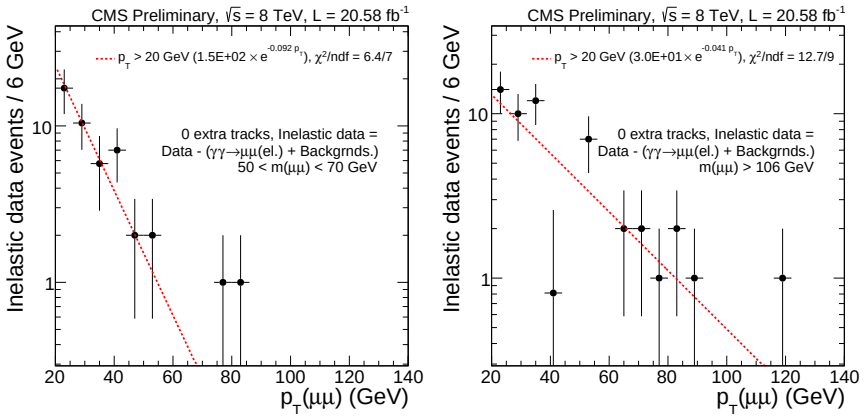

Figure 3.24: Fits to the dilepton transverse momentum for two regimes and for two invariant mass regions (below, and above the Z mass region).

Mass range	b ($\times 10^{-2}$ GeV^{-1})
$45-70$ GeV	9.182 ± 1.881
>106 GeV	4.105 ± 1.128

Table 3.8: Fit parameters for the 0 extra tracks exclusive region, as a function of the dimuon invariant mass range.

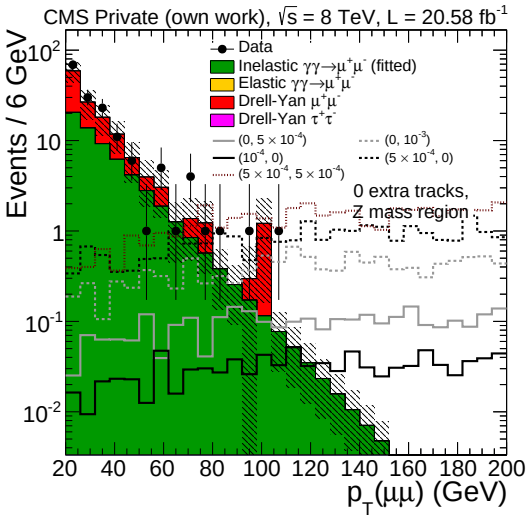

Figure 3.25: Dilepton transverse momentum distribution inside the Z mass region. The main background sources are given by the stacked histograms, with the dissociative $\gamma\gamma \to \ell^+\ell^-$ contribution as extracted from the sideband fits described in the text.

The overall slope in the signal region is hence: $b_Z = (0.066 \pm 0.021)\ \text{GeV}^{-1}$, where the error is statistical only. With the knowledge of this negative exponential slope, one may finally use this inelastic data distribution to extract the constant factor a in this region, and provide a data-driven prediction of the dissociative components of the $\gamma\gamma \to \ell^+\ell^-$ process in the Z mass region.

The validity of this approach is pictured in Fig. 3.25, again in this very same invariant mass range. On this figure, all exclusive, fitted semi-exclusive, and fully inclusive contributions are quoted along with the predictions of several anomalous $\gamma\gamma \to ZZ$ points.

3.3.4 *Limits at* $\sqrt{s} = 8$ TeV

Defining a lower bound to be set on this dilepton transverse momentum, one can extract a relative signal-to-noise expectation for the anomalous points used as a benchmark. Two values of this boundary are considered in this study, 100 and 150 GeV. The predictions for the inelastic background and two arbitrary anomalous signal points providing yields at the same orders of magnitude are given in the table 3.9.

If one extrapolates this study to a broader range of anomalous parameters, one can extract the one-dimensional yield pattern and estimate limits on anomalous couplings from a simple non-observation hypothesis. This behaviour is shown on the one-dimensional scan performed in Fig. 3.26 for both the anomalous parameters

Cut	Background	$(0, 10^{-5}\ \text{GeV}^{-2})$	$(5\times10^{-6}\ \text{GeV}^{-2}, 0)$
$p_T > 100$ GeV	1.15 ± 0.53	3.06 ± 0.13	0.83 ± 0.04
$p_T > 150$ GeV	0.032 ± 0.015	3.053 ± 0.126	0.827 ± 0.035

Table 3.9: Remaining background and signal events for two anomalous $\gamma\gamma \to ZZ$ search regions. The yields for the two anomalous signals are assuming no form factor regularisation (*i.e.* $\Lambda_{\text{cutoff}} \to \infty$).

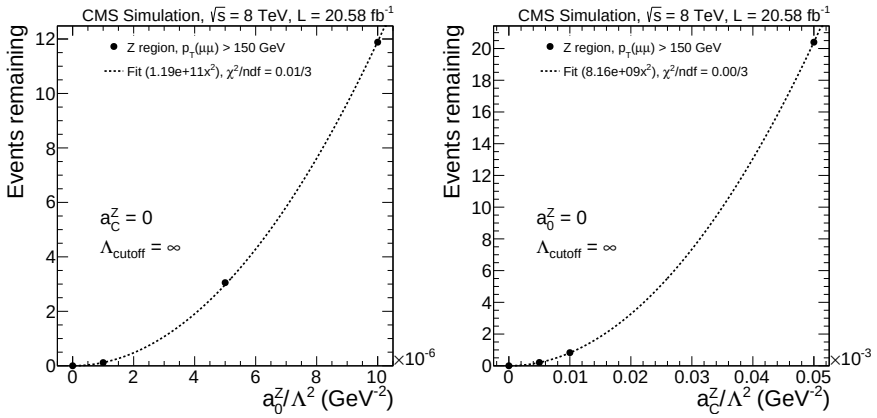

Figure 3.26: Remaining events at $\sqrt{s} = 8$ TeV after the signal selection for several anomalous points. For all these samples, one anomalous parameter is varied while setting the second to 0 (SM value). A parabolic fit is performed on this yield for all dilepton transverse momentum cuts.

providing a non-null contribution to this $\gamma\gamma ZZ$ coupling, for multiple lower bounds to the dilepton transverse momentum.

The parabolic shape of the equi-cross section lines, as shown in Fig. 3.22, enables to fit the predictions with a simple quadratic equation as a function of the $a^Z_{0,C}$ parameters. The fit results, along with their χ^2 goodness-of-fit value, is given on both the figures.

In Fig. 3.27, one can see the remaining data events observed at $\sqrt{s} = 8$ TeV with the CMS experiment. Two two-muon invariant mass ranges are given in this figure: the "full" mass range (above resonances, $m(\mu\mu) > 20$ GeV), and inside the Z mass region. One can see that respectively three and one events are observed in the first and second regions above the looser $p_T(\mu\mu) > 100$ GeV signal cut. In the Z range, the single observed event is characterised by a $p_T(\mu\mu) = 106.55$ GeV, and a $m(\mu\mu) = 90.21$ GeV. A transverse and longitudinal view of this event can be seen in Fig. 3.28.

However, no events are surviving the tighter value of this transverse momentum as introduced earlier, *i.e.* $p_T(\mu\mu) > 150$ GeV, in which most of the background contribu-

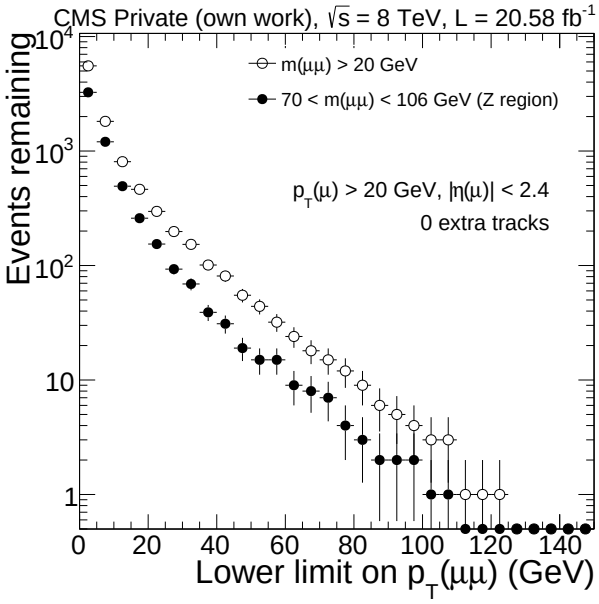

Figure 3.27: Remaining number of data events at $\sqrt{s}$ = 8 TeV, with respect to the dilepton transverse momentum lower cut applied, and for different dilepton invariant mass regions: above the low-mass resonances ($m(\mu\mu) > 20$ GeV, open circles), and in the Z boson mass search region (filled dots).

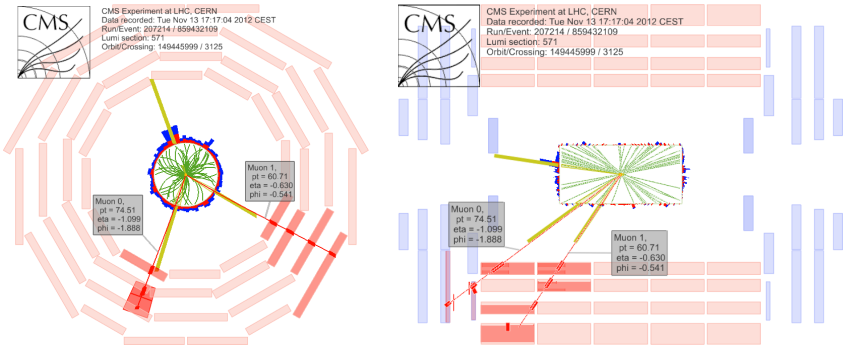

Figure 3.28: Transverse and longitudinal views of the single 2012 event at $\sqrt{s}$ = 8 TeV with two muons within the Z mass range, and with $p_T(\mu\mu) > 100$ GeV.

tions are suppressed.

The two one-dimensional relations between the anomalous couplings and the expected yield can be translated into one-dimensional limits on both the couplings. Using the method developed above to quantify the background contamination, one can simplify this estimation problem in approximating a full suppression of any background event in this tight signal region. Therefore, if one assumes this full suppression, one may expect an upper limit of $\lambda^{\mathrm{up}} = 2.96$, following the Poisson estimate at 95% CL, to be expected using the full statistics processed in this study.

When a form factor restoring the unitarity is applied (using a $\Lambda_{\mathrm{cutoff}} = 500$ GeV scale), the expected upper limits to the anomalous couplings parameters range at the order of 5×10^{-2} GeV^{-2}. With no unitarity regularisation, a better sensitivity can of course be reached, going down to the order of 5×10^{-6} (resp. 5×10^{-5}) GeV^{-2} for the neutral (resp. charged) parameter.

The one-dimensional limits extracted in this study are in good agreement with the expected sensitivities quoted in [62] (where a more complex semi-leptonic decay of the Z boson pair was assumed, *i.e.* $Z_1 \to \ell^+\ell^-, Z_2 \to \mathrm{jj}$). This result is even more promising if one consider that this phenomenological sensitivity analysis was performed without any pileup contamination. The latter is indeed expected to reduce the signals yield by approximately 60% in the Z mass region.

Nevertheless, the limits observed are quoted for the first time at LHC energies in a realistic experimental environment. Furthermore, the only limits for this coupling were already released a decade ago by the experimental probes of the inclusive photon pair production at LEP-2, as mentioned earlier.

Multiple methods can lead in a narrow future to the increase of this sensitivity, as for instance the opening to other decay modes for each Z boson. A large combinatorics would be offered by the hadronic decays of at least one of the gauge bosons into same-flavour jets as an example. Therefore, either the fully hadronic decays (the two bosons decaying into four jets), or the semi-leptonic (two jets, two leptons) channel, would increase by an order of magnitude the total branching fraction observable as a final state.

However, the actual track-based exclusivity condition still remains far too restrictive to open this final state to jets and objects of increased complexity. Indeed, the jet building procedure is highly dependent on the tracking capabilities, and these latter are in turn inversely correlated to the yield of secondary pileup interactions in each bunch crossing. Other selection techniques are hence required to include the higher branching ratio decay modes, and ensure a minimal observation efficiency.

A good candidate for the tagging of exclusive events through observation of the final states protons giving rise to the central system is introduced in the next chapter.

This apparatus will enable to increase in a short pace the overall sensitivity to the high-precision studies of the fundamental couplings of the standard model.

4

THE CMS-TOTEM PRECISION PROTON SPECTROMETER

Deep into the forward regions of CMS, at around 200 m of its interaction point, the installation of a new detection array is expected to occur within the second half of 2016. Divided into a tracking and timing detector components, this forward proton detector, the CMS-Totem Precision Proton Spectrometer [111] (hereafter abbreviated CT-PPS) will enable both the detection of the forward scattered protons, along with a direct determination of the central energy loss (the diphoton invariant mass $w_{\gamma\gamma}$, for the two-photon processes).

This apparatus, pictured in Fig. 4.1, will therefore allow a direct tagging of such central exclusive processes using an over-constrained determination of its central energy with the reconstruction of both the outgoing protons' kinematics [112], thus providing a better handle to central systems X of increased complexity.

As a mean to approach the beam within a short, millimetre-scale distance, the so-called *Roman pots* (RP) class of beam pockets are used. These pots, left outside the primary beam vacuum, may be moved transversely to the beam using a remote-controlled mechanics. This enables to leave the radiation-hard environment faced in the set-up and positioning of the beam inside the machine, while pushing the detectors towards the beam once this latter is declared stable.

With the steady loss of exclusive selection efficiency, using the central tracking, due to the worsening pileup conditions in Run-2, novel techniques of background reductions are needed. Thus the timing detectors described later in this chapter, and designed to fit inside the reduced spatial environment of RPs, will provide a direct way to separate the pileup events from a CEP of interest, as described in this chapter.

4.1 experimental challenges and the proposed CT-PPS detectors

One may quote several ways to increase the observation rate of the central exclusive processes in the proton-proton collider environment of the LHC.

First, by increasing the two-proton centre of mass energy. For instance, if one returns to the search for anomalous quartic gauge couplings in the probe of the $\gamma\gamma \to VV$ reaction, any BSM component (at a given value of the anomalous parameters) of the expected signal component section will rise as well. Hence, from $\sqrt{s} = 7 - 8$ to 13 TeV

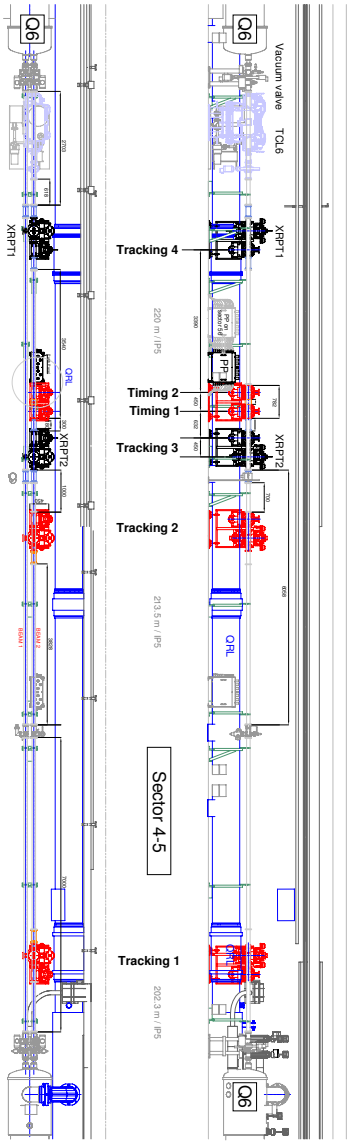

Figure 4.1: Vertical and horizontal layout of the CT-PPS *Roman pots* components in one arm of the very forward region of CMS. The distances are quoted with respect to the centre of the CMS detector (or IP5), not represented in this figure, but pointing towards the bottom direction. Figure extracted from [111].

in the two-proton collision energy, one predicts a clearer separation of any anomalous signal with respect to the expected backgrounds.

However, if the total pp interaction cross section remains stable with the increase of its centre of mass energy[1], the LHC machine parameters will slowly converge towards the design instantaneous luminosity of 10^{34} cm$^2 \cdot$ s^{-1} (or 0.1 μb $\cdot$ s^{-1}), by enlarging the single bunches composition. The price to pay for this instantaneous luminosity increase is the higher rate of collisions observed within the central detector environment, with an expected pileup of $\mu \sim \mathcal{L} \cdot \sigma_{\text{inel}} / f_{\text{rev}} \simeq 40 - 50$.

Since most of the CEP searches are highly dependent to any change in the vertexing and tracking performances of the central detector, and that such quantities are sensitive to the pileup conditions, one may expect the overall selection efficiencies to drop along time, steadily converging towards a system overflown in a saturated environment.

Two direct solutions are to be considered as means to restore an acceptable pileup level and to perform the full search for the central exclusive processes:

- select a collection of high-β^* optics, low-instantaneous luminosity runs which would enable to keep this events pileup under control through a drastic reduction of the available statistics collected within a limited run period,
- use the additional information from the CT-PPS allowing to clear this increasing noise from reconstructed events.

While the first method has been used successfully in dedicated searches[2], the precision studies developed in chapter 3 require large collected samples to ensure an increased sensitivity.

Hence, the second solution is strongly motivated for a direct implementation, as the information added will enable the tagging and reconstruction of the outgoing protons kinematics for any central exclusive system produced.

The precise knowledge of the outgoing protons state will also ensure a better handle to include more complex final states, such as the semileptonic decay of the gauge boson pairs within the central detector. This would involve an observed central system composed of one isolated lepton, joined with two jets, thus significantly increasing the available statistics through the combinatorics of additional decay modes.

Moreover, a loosened tracks multiplicity is required for this semileptonic production, as the vertexing of all tracks composing each jet can be challenging in this environment. Nevertheless, once the two-photon energy is extracted from the outgoing protons energy loss, an exclusivity condition based on this difference can be inserted.

[1] Between 7 and 8 TeV, this total interaction cross section increased from 98.3 ± 0.2 (stat) ± 2.8 (syst) to 101.7 ± 2.9 mb as measured in Run-1 by the TOTEM Collaboration [113, 114].

[2] One may quote, for example, the joint CMS-TOTEM measurement of the charged particles multiplicities in a broad range of pseudorapidities [115], or its early Run-2 measurement by CMS only [116].

Along with the double-tagging technique, one may also consider the single-arm tagging, where only one proton is reconstructed. This latter can provide a higher statistics of two-photon processes, where both the elastic, or the single-dissociative contributions are involved.

Consequently, a new experimental search window can be opened for the study of the photon distribution for the proton, and in particular in its dissociation component. Indeed, as emphasised in [117], this technique will show a good sensitivity to the modelling of photon fluxes.

The principle of operation for the successful tag of an outgoing proton can be described as follows:

- The "LHC clock" provides a standalone starting time delivered to all detectors for events synchronisation.
- One (or multiple) hit is reconstructed in the timing/tracking detector, and all collected information is temporarily stored in a buffer: a timing of arrival, and/or a raw reconstruction of the track according to the hits recorded in the tracking component.
- A Boolean information is sent as quickly as possible to the Level-1 trigger, enabling the central event to proceed directly through the common CMS HLT and storage stages.
- If a coincidence is found between the forward components and the central detector, its information is stored as an extra leaf to the central event.

With this scheme, a dedicated trigger window can be opened for the direct tagging of such exclusive events, and provide a proper rate of events in which the central detector is not even required to observe a given final state.

4.2 SUPPRESSION OF EVENT PILEUP BY PROTON TIMING

If one returns to the search for anomalous couplings in the $\gamma\gamma \to W^+W^-$ process as described in the former chapter, the effect of such a tagging enables to provide new handles to better separate the signal expectations from their important background sources. As seen earlier, the major source of uncertainty increasing with central collision rates is the pileup conditions, severely dragging down the tracks and primary vertex reconstruction in the central system. Therefore, the CT-PPS provides a good mean to reduce the events pileup observed in the central system for many exclusive processes.

Indeed, with a precise timing of the outgoing protons in this forward region, a simple time of flight technique using their arrival time difference can be developed to localise the collision point. This suppression is pictured in Fig. 4.2, with the black dots representing a primary collision vertex reconstructed through the energy deposits

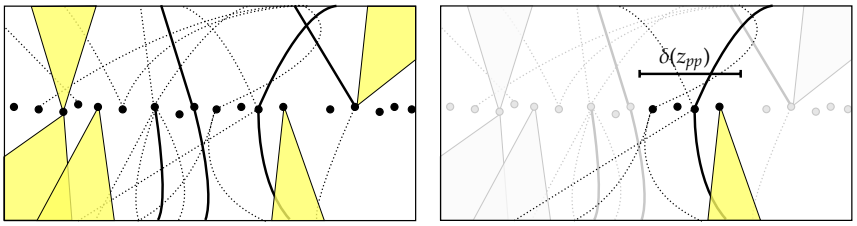

Figure 4.2: Principle of pileup suppression by timing. Lhs. figure displays a generic, high-pileup bunch crossing, without any pileup suppression through the CT-PPS timing detectors. Thick dots represent the primary vertices reconstructed in the event. Rhs. pictures this same event with a search window given by the timing constraint on the longitudinal position.

in each detection layers, the dashed and plain lines are generic and lepton tracks respectively, and the cones are jets.

One can quantify the required timing resolution related to the longitudinal coordinate of the primary vertex giving rise to the central exclusive process, as:

$$z_{pp} = \frac{c}{2}\left(t_F - t_B\right),$$

assuming high-energy, ultra-relativistic protons ($\beta \sim 1$). Hence the resolution on primary vertex' location is directly related to the timing resolution of the whole two-arms spectrometers:

$$\delta(z_{pp}) = \frac{c}{\sqrt{2}}\delta t.$$

On the rhs. of Fig. 4.2, one sees the effect of the suppression of primary vertices reconstructed outside a given longitudinal window (determined by the longitudinal resolution $\delta(z_{pp})$). This window size is therefore a new handle to control the background contamination and signal selection efficiency in exclusive searches.

The standard benchmark to be reached in a normal operation mode has been set to a longitudinal resolution of 2 mm. Hence, a time resolution of about 10 ps has to be sustained by all parts of the timing detectors, including the full readout chain. This resolution was estimated to provide a background events reduction factor of about 25.

In the case studies quoted later, a realistic timing resolution of 30 ps was also considered, compatible with the current limits reached experimentally and leading to a looser pileup suppression (with a $\delta(z_{pp})$ of about 6.4 mm).

4.3 TIMING DETECTORS

Along with the tracking components, the timing detectors will be installed in the very forward region of CMS, inside the so-called RPs.

Among the multiple techniques available to detect the passage of particles through a given medium, the ones relying on the Cerenkov effect typically provide the best timing resolutions. For the CT-PPS operations, two detectors built upon this effect are described here: the Quartic [118], and the GasToF [119, 120].

A complete description of the two detectors will be provided in the following sections.

4.3.1 *Cerenkov effect*

Several effects may be triggered once a high-momentum, charged particle enters a dielectric medium. Among these, the Cerenkov effect is observed as the emission of electromagnetic radiations around its path inside this medium. This radiation is originating from the local disturbance (*i.e.* polarisation) appearing in the wake of the particle. Therefore, a coherent shockwave is produced as a mean to release the energy induced locally.

Hence, this effect can only be observed once the speed of the particle is significantly higher than the speed of light in this medium, *i.e.* the speed of light in vacuum reduced by the refractive index observed in the medium.

In classical physics, this phenomenon may be compared to the "Mach effect", producing a shock wave when a supersonic aircraft is travelling faster than the speed of sound in the atmosphere. Here, at each flight step, the air volume surrounding the plane is propagated to some distance given this speed of sound while the later is slightly further away than this "wave-front". It then follows that an air cone is produced following a direction opposite to the speed of this aircraft.

In the corpuscular description of the Cerenkov effect, the energy emission can geometrically be pictured as a production of photons inside a cone with an opening θ_C such as

$$\cos\theta_C = \frac{1}{\beta n}, \tag{4.1}$$

with $\beta = v/c$ (or v in Natural units) the incoming particle's velocity in units of the vacuum speed of light, and n the medium's refractive index.

The energy spectrum of such a radiation can be expressed using the *Frank-Tamm* formula providing the photons yield in a distance interval dx:

$$\frac{\mathrm{d}^2 N_\gamma}{\mathrm{d}x\mathrm{d}\omega} = \frac{e^2}{\omega^2}\sin^2\theta_C = \frac{e^2}{\omega^2}\left(1 - \frac{1}{\beta^2 n^2(\omega)}\right).$$

Rewriting this equation in the energy domain, one may extract the total Cerenkov energy spectrum:

$$\begin{aligned}\frac{\mathrm{d}E_C}{\mathrm{d}x} &= e^2 \int_0^\infty \mathrm{d}\omega \cdot \omega \left(1 - \frac{1}{\beta^2 n^2(\omega)}\right) \cdot \Theta\left(1 - \frac{1}{\beta n(\omega)}\right) \\ &= e^2 \int_{\omega_{\min}}^\infty \mathrm{d}\omega \cdot \omega \left(1 - \frac{1}{\beta^2 n^2(\omega)}\right)\end{aligned}$$

where the *Heaviside function* $\Theta(x) = 1$ if $x \geq 0$ and 0 if $x < 0$ is taking into account the threshold β value of the incoming primary particle, *i.e.* above which its speed is higher than the speed of light in the medium and this Cerenkov effect can occur.

Hence, given the normalisation factor to the overall integral, both this absolute number of photons, or their energy density emitted per unit length is extremely low with respect to any other energy loss in a medium, such as the ionisation losses or the multiple scattering.

Nevertheless, a crucial property of this Cerenkov effect is its fast production, standing among the fastest processes in a particle-matter interaction. This represents a rather interesting feature for a timing detector where the rising signal speed is directly linked to the timing resolution.

4.3.2 `Quartic`, *the quartz Cerenkov detector*

Selected as a baseline detector for the early operations of the `CT-PPS`, the `Quartic` detector is detecting the particles above a certain momentum threshold through the emission of the Cerenkov radiation arising from its passage through scintillator bars.

As pictured in Fig. 4.3 for two stations like the ones to be installed in the LHC tunnel, one of the interesting features of this detector is the granularity it offers. Indeed, with 4×5 cells (or "bars") through which the outgoing protons can transit in this forward region, a precise determination of its position can be reconstructed.

As quoted above, the signal is formed through the scintillation of a photon shower produced by the passage of the charged proton through the dense medium of the "L"-shaped bars. This geometry allows to insert a long radiator segment collinear to the beam, and provide a two-dimensional segmentation, while maintaining the readout electronics (pictured as the small squared volumes) the farthest away from the beam and its highly energetic secondary particles halo. The granularity is therefore defined by the cross section of each longitudinal part of the radiators. The area designed for the detector installation in the experimental cavern is at 3×3 mm^2 per bar.

These bars are therefore required to comply with optical properties, such as a refractive index allowing each photon produced in the cone to reach a total reflection. Geometrically, this translates into a limit on $\theta_C > \pi/4$, or $n(\lambda) > \sqrt{2}$ (for the whole λ

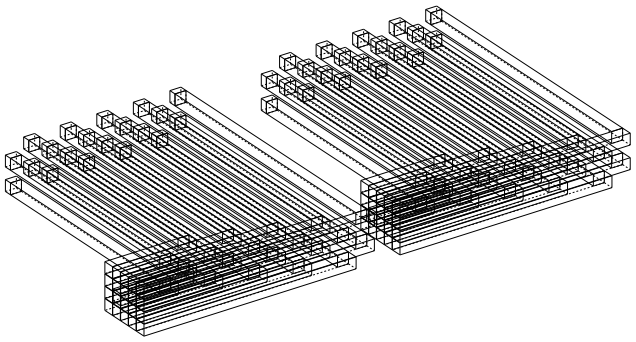

Figure 4.3: Schematic view of two `Quartic` stations containing an array of 4×5 radiator bars each, as developed for the early `CT-PPS` timing operations. The SiPMs readout devices are pictured as the squared volumes at the end of the "L"-bars.

range). Hence, two materials are considered to sustain this criteria, namely quartz and sapphire bars.

For the signal collection under real beam conditions, it was chosen to rely on an array of silicon photomultipliers (SiPMs), enabling to reach a time resolution of about 60 ps per bar, while maintaining a reasonable lifetime under full beam illumination[3].

4.3.3 *The `GasToF` detector*

Following another design, the `GasToF` is also based on the fast detection of the Cerenkov light cone produced by high-momenta particles passing through a radiator volume. It was fully developed, engineered and mechanically conceived in the workshop of the UCLouvain by L. Bonnet *et al.* [119, 120].

Its geometry is simpler than the `Quartic` previously described, as it consists in an "L"-shaped vessel containing a gas acting as a radiator. This gas is therefore required to follow specific optical properties, such as a small refractive index (with $(n-1) = 1 \times 10^{-3} - 4 \times 10^{-3}$). It allows the photons to be radiated inside a cone with a relatively small angular opening. For this operation it was chosen to be the C_4F_{10}, or *perfluorobutane*, commonly used in ring imaging Cerenkov detectors for its compatible optical features. Following Eq. 4.1, and given the refractive index characterising this gas, the Cerenkov cone is contained in an angular range of 2 to 5 degrees with respect to each incoming charged particle.

Once created around the particle path, the largest fraction of this cone is reflected in a perpendicular direction, towards the other extremity of the 'L' shape, with the help of a 45° mirror placed in the corner. Finally, it reaches a photo-multiplier tube (PMT) to

[3] This fluence approximately evaluated to 10^{12} equivalent neutrons per cm^2 for a full Run-2 integrated luminosity $L = 100$ fb^{-1}, as quoted in [121].

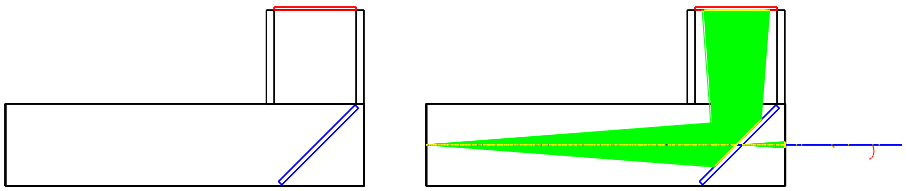

Figure 4.4: Wireframe view of a 20 cm (horiz.) × 10 cm (vert.) long GasToF with a flat mirror as simulated by the Geant4 code. The (red) topmost area at the edge of the vertical part is the MCP-PMT sensitive photo-cathode used to map photon hits distribution. Right figure pictures the GasToF in operation containing a Cerenkov light cone produced by the transition of incoming particles.

transform individual photon hits into an electronic pulse to be collected and processed. The simple geometry of this GasToF is pictured in Fig. 4.4 for a 20 cm optical length detector (*i.e.* the distance between the entrance of the front window and the mirror). The rhs. figure displays an example of a light cone produced by five 6.5 TeV protons hitting the GasToF at the centre of its entrance window.

This configuration is therefore integrating the full mapping of particles to be observed around the beam pocket, onto one single window leading to one single radiator volume, unlike the Quartic design. For a fast charge collection (thus a sharp leading edge of the signal, increasing its timing resolution), one can either rely on a single-anode detector (with only one channel integrating the full sensitive range) or a higher-granularity, multi-channel plate photo-multiplier tube (MCP-PMT). This first possibility being covered elsewhere [38], one can examine and study the MCP option.

Furthermore, the steady increase in beam intensities will involve a higher proton multiplicities in the forward detectors. In order to estimate the exclusive proton multiplicities within an event, either the number of detectors can be increased (for instance, putting several GasToF along the beam direction, or mixing it with the Quartic detector described above), or the clustering capabilities of a multi-channel solution can be taken into account in the estimation of the full event timing.

4.3.4 *GasToF operation mode*

For a proper conversion between the arrival of a photon cone and a collection of analogue signals (one for each channel) to be digitised and propagated to a data acquisition system, one relies on the principle of operation of this MCP-PMT sensitive detector.

The first layer encountered by each photon hit is a bialkali photocathode, converting this energy deposit into the emission of a limited amount of charge carriers. The following stage is the amplification of this emitted charge into a noticeable electronic signal. This operation is performed by the multi-channel plate part of the apparatus,

a collection of thin glass layers perforated by a high density of holes. Plunged into a high local electric field, each hole provides a medium where the amplification is possible between each extremity. This technique enables the output signal to reach a gain varying from 10^3 to a few 10^6, depending on the bias voltage applied on the MCP sub-part, from very low input charges.

The MCP-PMT solution described in the scope of this thesis and in the full CT-PPS *R&D* case study is the the 8×8 channels *Planacon® XP85112* [122]. The bias voltage-dependent gain for this apparatus is pictured in Fig. 4.5b.

Therefore, each photon collected at the end of this detector has a finite probability to be converted into a photo-electron, mainly determined by the embedded scintillator component. The chemical composition for a bialkali window as used here enables to reach a high sensitivity at visible light spectra, with a rather low dark current[4] rate, constrained at the order of 2 nA at $V_{\text{bias}} \simeq 2.4$ kV or 10^5 gain.

All these effects being taken into account, one can combine the overall detection efficiency into one single observable, the *quantum efficiency* (QE). It is defined as the total probability of converting a single photon into a photo-electron through this scintillation process, given any photon energy (or wavelength). The effect of this quantum efficiency is simulated by a convolution through this photon energy:

$$n_{\text{pe}} = n_\gamma(\lambda_\gamma) \otimes \mathbf{QE}(\lambda_\gamma).$$

This total quantum efficiency is pictured in Fig. 4.5a for the MCP-PMT model previously quoted, and used in the *R&D* prototype developed in 2015 at UCLouvain. As seen on this figure, the sensitive energy range of such an device is at the order of $200 - 600$ nm, corresponding to single photon energies of $2 - 6$ eV, compatible with the single photon energy ranges expected from a Cerenkov radiation.

Given its larger volume and a relatively low photoelectrons yield per incoming proton, the multi-channel GasToF will therefore enable to distinguish multiple protons entering through the front window, as mentioned earlier. Indeed, with a photoelectrons yield per proton evaluated[5] around 7, and spread on an average of 40% of the full PMT granularity, two collinear protons separated in time by 50 ps can be properly distinguished in the readout.

4.3.5 *Cerenkov timing detectors readout*

The full acquisition for both the timing detectors needs to undergo strong constraints to be able to operate efficiently during the CT-PPS data taking periods. These are either for the important hits acquisition rate to be sustained, the timing resolution requirements, and the very fast preprocessing and response time to provide the full information to

[4] The dark current is an electronic noise to be observed in a photon detector when no single photon enters its sensitive volume. It can be viewed as a continuous background to be subtracted from any measurement.

[5] This number is evaluated for the "short" (RP), 12 cm optical length version of the detector at a high gas pressure of 2 atmosphere.

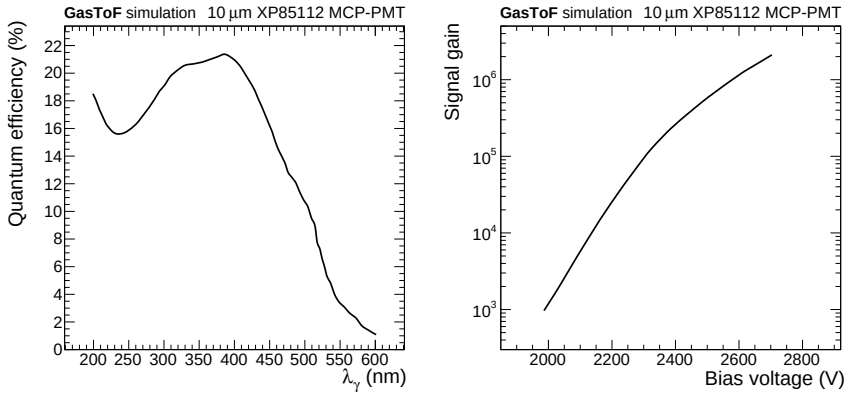

(a) Quantum efficiency, function of the incoming photon's wavelength.

(b) Overall signal gain, function of the bias voltage applied on the cathode.

Figure 4.5: Typical *Planacon® XP85112* MCP-PMT operation parameters, as implemented in the simulation code described in the text. Quantities are extracted from [122].

the central CMS triggering system.

The amplifier and discriminator components are embedded into one single component, the NINO module [123, 124]. It was originally designed for the multigap resisitive plate chambers used in the ALICE experiment. A schematics of its logical sub-parts is shown in Figure 4.6 for one single channel.

One can emphasise the input preamplifier followed by the four amplification stages enabling a high bandwidth while retaining a low individual gain.

An interesting feature of this module is the direct relation observed between the input charge and the output pulse width. This width is shown to vary rapidly for small pulses while the variation decreases for larger signals, is pictured in Fig. 4.7. Thus, after calibration, the photons multiplicity in each event can be reconstructed from this latter observable.

For the offline collection, the 2×32 channels embedded in this NINO board are furthermore digitised and propagated through ASICs to the full CMS readout system, as pictured in Fig. 4.8. The intrinsic time resolution of this full module was measured to be below $8 - 10$ ps rms.

The final digitisation is performed by a HPTDC[6] chip with a 25 ps time samples binning, and developed at CERN's ECP-MIC division.

As an mean to match the packets definition to CMS data structure, a μTCA.4 [125] implementation of the FED (*Front End Driver*) and FEC (*Front End Controller*)

[6] *High-Precision Time-to-Digital Converter*. This component is described in Appendix B.

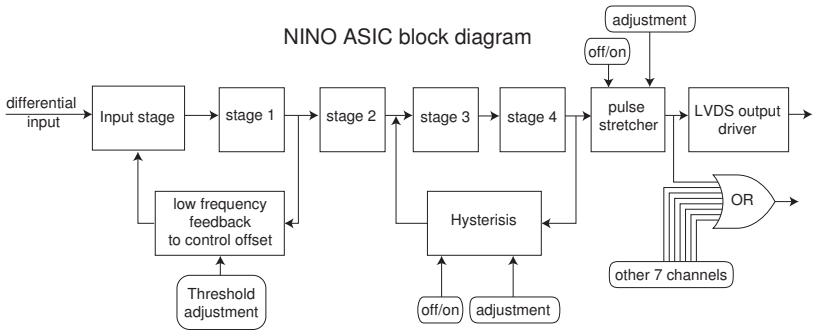

Figure 4.6: Detailed schematics of all logical elements present in one single NINO ASIC channel. Figure extracted from [123].

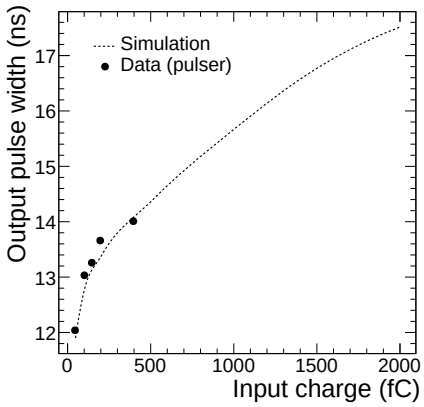

Figure 4.7: Correlation between the input charge provided to the NINO board by a generic pulser, and the output (digital) pulse width. The output of the SPICE simulation is quoted for comparison. Figure extracted from [123].

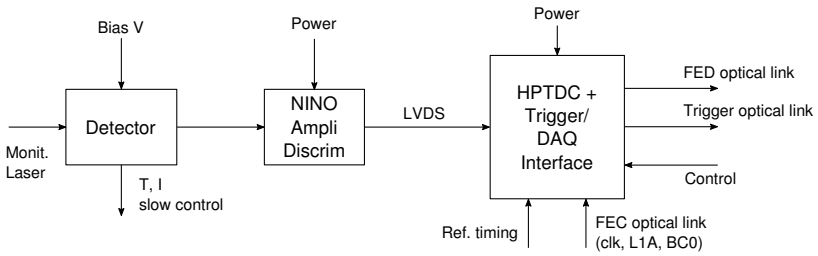

Figure 4.8: The common readout electronics to be used along with the timing detectors. One can emphasise the FEC/FED scheme used to interact with the central CMS acquisition system.

architecture is used the same way as other CMS subdetectors as operated during LHC's Run-2. In this format, time-stamped data samples are packed in a standardised way prior to their propagation to the trigger and common data pipelines, and before the storage on tape.

4.3.6 *General overview*

In summary, both the `GasToF` and the `Quartic` detectors would enable to reach timing resolutions close to the $10-50$ ps benchmarked for a proper `CT-PPS` timing operation.

The former is expected to provide a good resolution, even with single photons. Thanks to its simple geometry and optics, it is designed to sustain a radiation-hard environment, with a fluence at the order of 5×10^{15} cm^{-2} neutron equivalent particles in this region. The active element is therefore standing sufficiently far from the beam orbit. With its low material budget, it will also minimise the multiple scattering effects. The price to pay for this simple geometry is the integration of the full Cerenkov cone onto one single detection array. As seen earlier, this complicates the detector operation with high multiplicities of protons hits per event.

On the other side, the `Quartic` detector allows to ease the solving of this issue through its high granularity (4×5 cells). However, one may expect a lower photons yield on the sensitive area, given the complexity of the inner photons paths inside the medium. Also, the high density of its radiator prevents the multiplicity of detectors to exceed two (at most), given the relatively high fraction of nuclear interactions expected in these bars (between 7.2 and 14.6% for quartz bars).

Therefore, the best solution is possibly to combine both the detectors into the full timing system. This would allow to reach a good signal sensitivity with higher photoelectrons yields, while being able to "track" the possible multiplicity of incoming protons with a good segmentation.

Additionally, the two detectors may share a similar readout electronics with their equivalent signal characteristics. No further development would hence be needed

downstream to implement this strategy.

Finally, other detector technologies were also considered, such as ultra-fast solid state detectors with a fine granularity. Thanks to their relative thinness (at the order of 100 μm per layer), several layers can be stacked in each station. With this technique, the timing resolution of the full detector is approximately improved by the square root of the total number of layers. Hence, a 10 ps time resolution could be achieved by a stack of ten individual layers with a reasonable $\delta t_{\text{single}} \sim 30$ ps. This technology goes beyond the scope of this thesis, and a more detailed description can be found elsewhere [111].

4.4 DETECTOR SIMULATION

The simulation of the full event picture requires a dedicated description of the layers of material the protons might encounter in the forward region. As it will be developed in section 4.4.1 the effects of an interaction faced by the protons in the central system can be propagated towards the forward regions, thus providing an accurate prediction on their path through all optical elements composing the beamline.

Multiple parameters are taken into account to simulate this path, including the potential absorption of the proton in any component of the beam pipe. To quote a few, one finds the central energy loss (often given as a fraction of the incoming momentum, ξ), or the longitudinal and transverse momentum losses in the chain of optical elements.

This section can be divided into two sub-parts, reflecting the whole simulation work being done during the development of this apparatus.

The first one describes the propagation of the protons giving rise to the central system towards the very forward regions of the whole beamlines. The second is related to the `GasToF` simulation scheme, as required for its precise optimisation for a successful operation in these regions.

4.4.1 *Beamline simulation*

The simulation of the full beamline around LHC's Point 5 was performed using `Hector` [126], a tool developed at UCLouvain by J. de Favereau and X. Rouby. It relies on the propagation technique described in section 2.1.3, using the actual optics encountered at all segments of the LHC.

It is the worthy successor of `MAD-X` [127], an older propagation tool still commonly used nowadays. The main core of this code is embedded inside a standalone `C++` package relying on CERN's ROOT framework, thus making it simpler to use for newer generations of experimentalists. This code was used for all `CT-PPS` beamline simulations quoted in this chapter (including the $\gamma\gamma \to W^+W^-$ motivational studies in section 4.2).

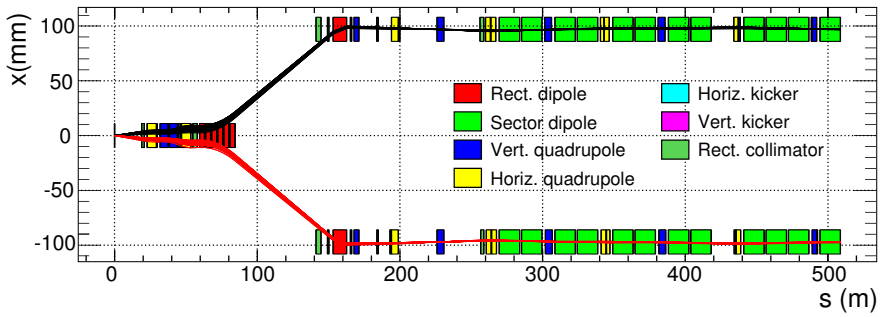

Figure 4.9: Closeup of the beamline elements around the CT-PPS position, as defined in the LHC optics parameterisation used in the Hector simulations. One can distinguish the topmost beam envelope exiting the central detector from the bottom-most incoming particle beam (the black and red lines respectively). Figure extracted from [126].

Given the beam conditions expected in this very forward region of the LHC, one must emphasise that the signal events are surrounded by pileup protons arising from secondary interactions occurring in the central system or around the beamline.

In order to integrate this effect into the simulation, the same recipe as developed by CMS (described in section 2.4.3) was used.

Hence, multiple *minimum bias* events are integrated into each simulated event, following a reasonable distribution corresponding to the observed number of primary interactions at each bunch crossing. These additional particles are then propagated through the beamline elements just like any "real" signal proton.

Two stations are defining the forward detectors acceptance: the tracking and timing stations, located at $z = \pm 204$ and ± 215.5 m from the central detector's interaction point.

If one returns to the beamline propagation equation (2.3), Hector is using a 6-dimensional set of coordinates vectors $\mathbf{x}(s)$ for all particles within a beam: the x, y positions in the transverse plane at a given path length s, their angle with respect to the longitudinal direction $\mathrm{d}x/\mathrm{d}s, \mathrm{d}y/\mathrm{d}s$, their energy E, and their initial angular kick. Therefore, it needs a collection of 6×6 transport matrices to propagate all particles through the collection of optical element composing the beamline.

These are provided by the LHC optics group [128], and can directly be imported into Hector to build its set of matrices. A closeup of these elements in the CT-PPS region as simulated in Hector is shown in Fig. 4.9.

The embedding of this tool within the full CMS reconstruction software then allows to define several regions of interest at which the particles tracks can be counted and their kinematic properties can be extracted. For instance, a hit map of all secondary particles near the Roman pot housing the tracking detector, as generated by this scheme, is

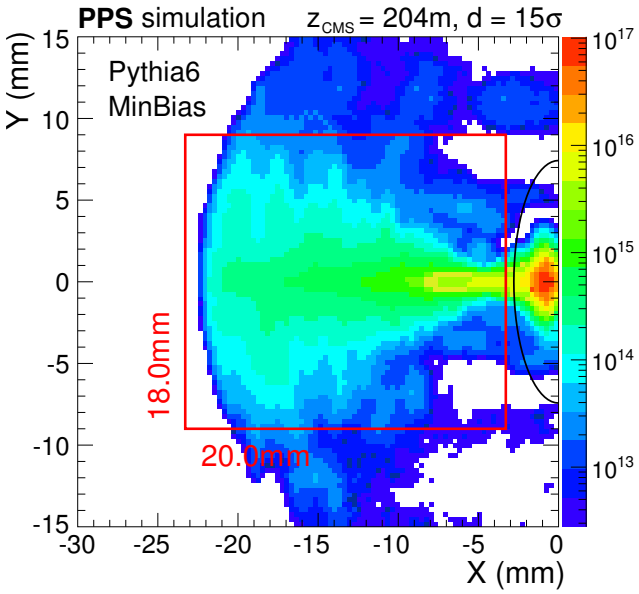

Figure 4.10: Proton fluence expected at $z = 204$ m of the two-proton interaction point, as propagated by a `Hector` simulation using optical properties of the beam lines around CMS. The rectangular line highlights the contour of a baseline 4×5 cells `Quartic` module to be used in *Roman pots* during early Run-2, and the ellipse highlights the 15σ beam contour. Figure extracted from [111]

pictured in Fig. 4.10. The baseline `Quartic` position and dimension has been included in this figure to illustrate the expected fluence at that distance of the beam pocket.

4.4.2 *Cerenkov detectors simulation*

A full simulation of the `GasToF` detector geometry, along with Cerenkov and optical processes description, has been developed for a better understanding of its response under various beam (and more generally run) conditions. This `C++` simulation of `GasToF` is based on a `Geant4` [129] core.

This code was developed following the same guidelines and geometrical conventions as a previously-released ray-tracing code by T. Pierzchała and N. Schul [38], while relying on the optical processes as directly simulated in `Geant4`.

Its operation relies on a propagation of *optical photons* through the various material layers providing their boundary conditions. In this approach, each particle is propagated through all layers of material. After each iteration, the probability for each track to decay/scatter/exchange energy-momentum/... (and reflect/transmit/... in the

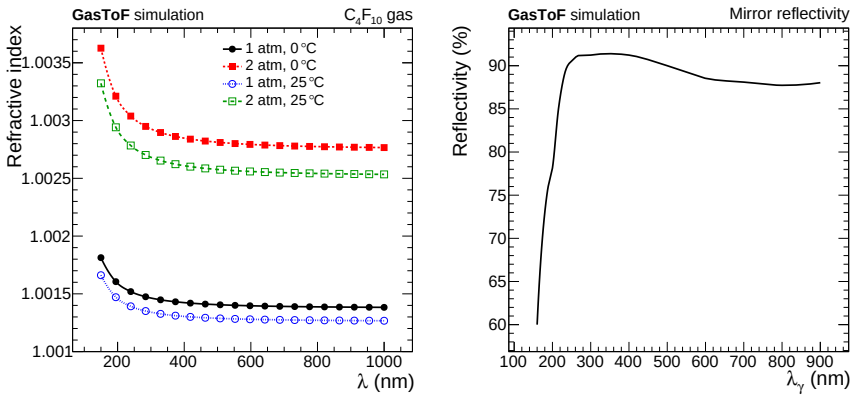

(a) C_4F_{10} gas refractive index (b) Mirror reflectivity

Figure 4.11: Optical properties of materials used in `GasToF` simulation, as functions of incoming photons' wavelength.

particular case of optical photons) is computed and treated as an iterative weight.

The C_4F_{10} refractive index value used in the simulation is pictured as a function of photons' wavelength λ in Fig. 4.11a. One can see that for a gas like this C_4F_{10}, widely used for its optical properties useful in the Cerenkov processes, both the temperature and pressure provide handles to control the opening of this light cone. Therefore, either an increase of the temperature or a decrease of the pressure will give a lower refractive index, thus a decrease of the opening angle θ_C, and vice versa.

One can also see from (4.1), that this cone opening angle increases with incoming particle's kinetic energy, thus providing a connection between the signal shape and the incoming kinematics.

For all simulations quoted here for the baseline detector[7], a fixed set of simple (but realistic) conditions was defined. The primary mirror is for instance expected to be a metallic ultraviolet magnesium fluoride mirror with a reflectivity shown in Fig. 4.11b. As seen on this figure, it allows a good operating mode in an high range of photon energy (between $\sim$ 160 and 900 nm).

4.4.3 `GasToF` *geometry study*

Given the observed fluence in the region at which this timing detector will be installed, a fine study of the detector geometry is required. Recalling the expected fluence as pictured in Fig. 4.10, one may emphasise the low spatial uniformity of the vast majority

[7] This also corresponds to the one used in the 2015 test beam at SPS described later in section 4.5.

of particles produced around the beam. This poor uniformity is introducing a set of technical issues to be foreseen in both the timing and tracking detectors.

In this study, two versions of this detector were considered as baselines for a future installation around the LHC beamlines. These two geometries are designed to fit either in a Roman pot, therefore inside a limited available space, or inside a moveable beam pipe (MBP ; also named *Hamburg beam pipe* [130], recalling its first installation in a large-scale experiment) version.

The first (resp. second) version, hereafter called *short* (resp. *long*) version, is characterised by its longitudinal optical length. This distance is computed between the front window (the entrance point of each proton in the vessel), and the mirror position. For the short version, this optical length was chosen to reflect the 14.5 cm inner radius of the actual RPs used for the `Quartic` operations around IP5. Hence, a realistic length of 12 cm was simulated. For the latter version fitting in a MBP, a slightly longer distance of 20 cm is selected.

Beside the space available for a proper installation of this detector, several strong constraints also affect its overall geometry. To quote a few, one may emphasise the radiation hardness to be sustained by the vessel[8] and the readout electronics, and the very in-homogeneous spatial distribution of the Cerenkov cone produced inside the vessel.

The latter criteria directly arises from geometrical arguments, knowing the expected signal and pileup protons hits maps in this region. Indeed, as described above, in the region considered for the installation of both the timing and tracking detectors (204 – 215.5 m distance from the interaction point), the expected proton spatial distribution will be restricted to a small part of the active region.

Hence, it is required to optimise the light path to be followed by the Cerenkov cone inside the detector, using several techniques. These were studied intensively for several parameters by M. Renaud in the scope of his Diploma thesis [131]. One can quote, for instance:

- the geometry of the primary mirror, as a best candidate to correct the in-homogeneity of the incoming beam location,
- the modification of the internal photon paths (addition of internal mirrors), enabling secondary photons leaving the cone envelope to reach the detection area,
- the influence of the C_4F_{10} pressure, defining the overall photons yield per beam particle transiting through the vessel.

At first, for the sake of simplicity, one can simulate the case in which a single proton is shot at the middle of the front window.. A direct comparison of the photons yields

[8] As extrapolated from the TOTEM measurements using the *Roman pots* installed in this region, the expected fluence (neutron equivalent particles) reaches 5×10^{15} cm^{-2} for an integrated luminosity of 100 fb^{-1}.

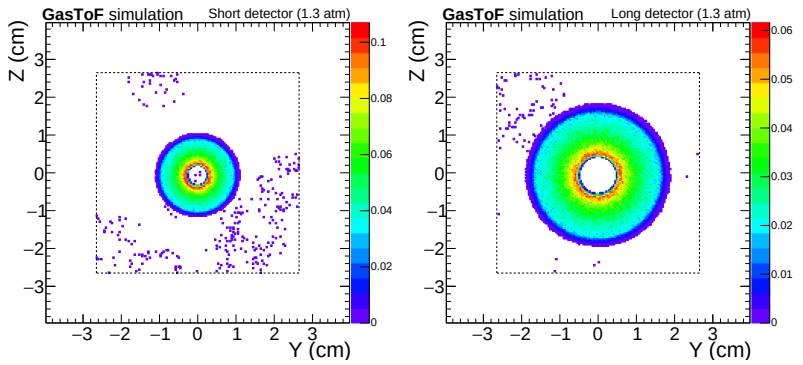

Figure 4.12: Effect of the vessel length on the yield per proton of photons collected on the photo-cathode. These simulations are assuming a 6.5 TeV proton hitting the centre of the front window, and a realistic set of mirror optical properties. The dashed lines represent the sensitive region edges.

expected for the two longitudinal lengths is pictured in Fig. 4.12. One can notice that the longer is the longitudinal optical length, the broader is the cone opening to be detected on the sensitive part of the detector.

Another interesting feature is the relative stability of this yield with respect to the rotation of the primary mirror. This behaviour, expected if one assume a smaller cone opening than the sensitive area, is shown in Fig. 4.13.

As pictured in Fig. 4.14, the C_4F_{10} pressure is another parameter affecting the cone opening for all Cerenkov photons to be produced along the beam particle path, given its influence to the refractive index of the medium. The default internal absolute pressure is set to 1.3 bar, hence not too far from the atmospheric pressure (this property minimises the risks of gas leaks if one assumes realistic soldering and material resistance).

4.4.4 `GasToF` *mirror shape*

The central proton case described above is however by far too simple to characterise the overall detection efficiency in an environment such as the `CT-PPS`, the protons being more likely to arrive at the edge of the sensitive area.

When propagated to the position of this `GasToF` module, one can therefore extract the expected signal shape to be observed in all 64 channels of the PMT. In order to enhance the collection rate, the wall closest to the beam is set to be reflective, with the same properties as the primary mirror.

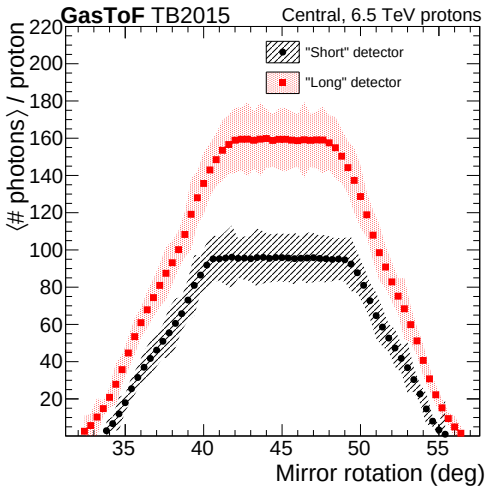

Figure 4.13: Photon hits yield for different values of the mirror angle (with respect to the incoming protons direction) of the GasToF longitudinal optical length as simulated by Geant4, if one 6.5 TeV proton hits the detector at the centre of its entrance window. The C_4F_{10} gas pressure is assumed to be 1 atm in this simulation.

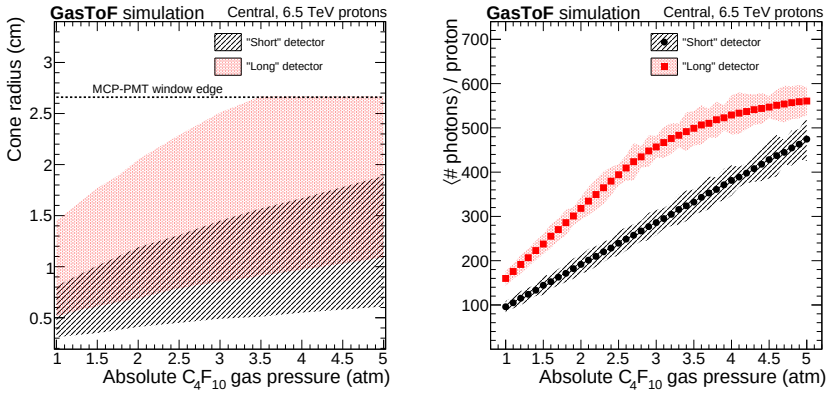

Figure 4.14: Effect of the C_4F_{10} pressure on the cone opening, thus on the yield of photons collected on the photo-cathode. These simulations are assuming a 6.5 TeV proton hitting the barycentre of the front window, and a realistic set of mirror optical properties.

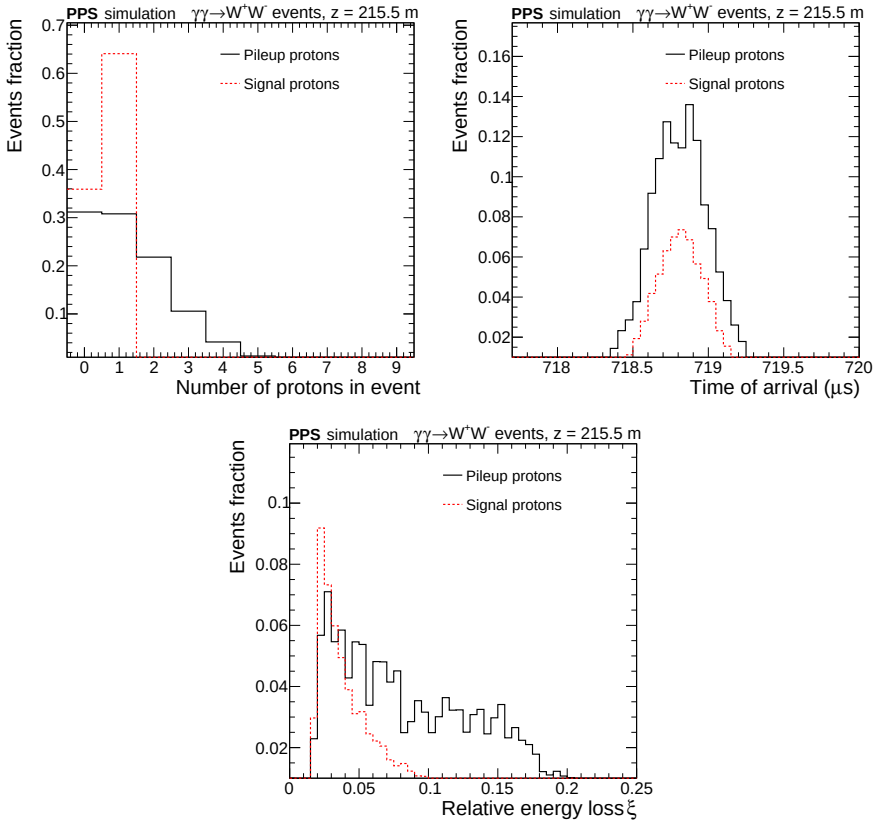

Figure 4.15: Forward protons composition per event at $z = 215.5$ m for 2×10^4 simulated events of a $\gamma\gamma \to W^+W^-$ central system. In such events, the scattered protons (dashed lines) creating the central event are propagated through the beamline along with pileup protons (solid lines).

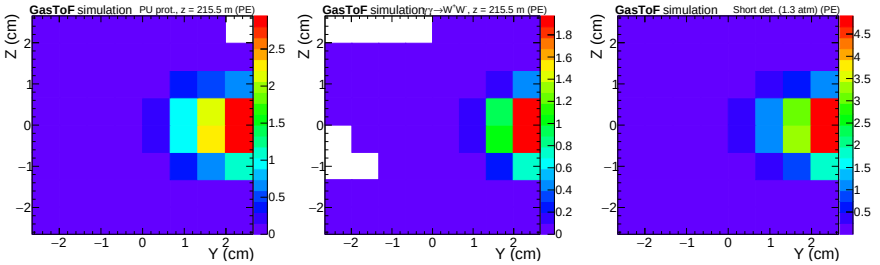

Figure 4.16: Simulated photo-electron hit maps per event for the short "RP" `GasToF` dimensions as described in the text, with an inner C_4F_{10} pressure of 1.3 atm. The first two figures are detailing the incoming particle type (pileup/background, or signal proton), are both are combined in the third figure.

In Fig. 4.16, the mean photo-electron yields per MCP-PMT cell and per event are shown for both the $\gamma\gamma \to W^+W^-$ signal and the background protons entering the sensitive region of the detector. As pictured, the two contributions can hardly be discriminated using a "naive" analysis based on the shape of hits clusters.

Therefore, one may introduce a further study of the mirror shape to maximise the background suppression using a purely geometrical argument. The flat mirror option was hence joined with a convex mirror possibility, thus spreading the reflected photon paths towards the full sensitive coverage of the PMT.

With a given set of curvature parameters listed in [131], the maximal/minimal occupancy cells can be brought together towards a factor 14, removing the corner cells difficult to reach by the photon paths, and the average photo-electron per PMT cell can be reduced to a fraction of a hit, as seen in Fig. 4.17.

One can see that the geometrical properties of both the pileup and signal protons arrival patterns are combined to the output distribution, thus providing a better handle to discriminate them through the extension of the hits cluster. In the perspective of its integration into the spectrometer, this feature would provide a proper selection process to give at the readout stage a "pileup likelihood" weight to each event.

With this technique, the relative modularity of this detector allows to reach a reasonable events reconstruction. This supposes the prior knowledge of the events shape as expected at the entrance of the detector, and function of the machine parameters.

4.5 TEST BEAM AT SPS

A serie of test beams was performed at CERN's *Super Proton Synchrotron* (SPS) during the Summer and early Fall of 2015. It enabled to include two major timing detectors designs, as well as a tracking station, into one single running operation with a common set of beam conditions.

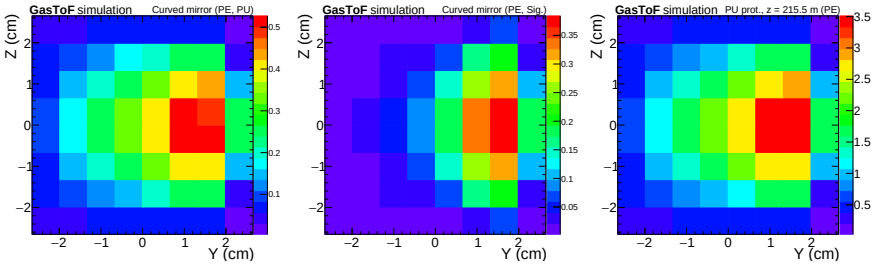

Figure 4.17: Effect of the mirror curvature on the event shape as seen by the photo-cathode. The first two figures are detailing the incoming particle type (pileup/background, or signal proton), are both are combined in the third figure. Extracted from [131].

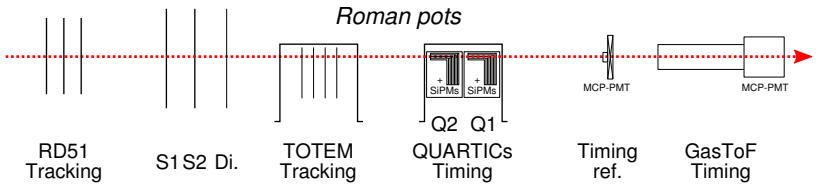

Figure 4.18: Detectors layout for the end of 2015 test beams at CERN's SPS.

As shown in Fig. 4.18, the tracking stations were all located upstream the timing detectors, since the `Quartic` budget is expected to trigger a noticeable amount of nuclear interactions, potentially harming the thin layer of depleted silicium composing the trackers.

In an attempt to maintain the events synchronisation between both the sub-components, and allow a direct matching in the offline reconstruction and analysis, the timing detectors triggering scheme was developed to be dependant on the tracking "trigger-out" information. This tracking detectors triggering part enabled some flexibility to define the start of each event, being able to select any combination of all upstream detectors to be used in the global coincidence:

- `S1`, `S2`, two fast scintillators with a physical overlap of 2×2 cm^2,
- `Di.`, a one-plane, high granularity TOTEM diamond timing detector proposed for its upgrade [132].

A full description of the data acquisition scheme used during this test beam can be found in the section B.1 of the appendices.

Despite the short timescale between the test beam and the submission of this document, a few preliminary results will be quoted on the timing distributions as observed by the `GasToF` detector and its full acquisition system, once illuminated in a proton beam.

4.5.1 *Beam conditions*

The beamline itself, H8, is one of the 7 lines extracted from the SPS. The protons composing the beam are accelerated in the very same way as the LHC beams, in a chain pictured in Fig. 2.1.

Once reaching the SPS, the beam has an energy in a range of 400 – 450 GeV. These packets of protons are then periodically extracted from the storage ring and propagated to three primary targets, upstream to several linear chain pictured in Fig. B.4, and propagated to collide a primary T4 target made of beryllium. The secondary beam arising from this target to reach the experimental area is characterised by a reduced momentum of 180 GeV.

The timing structure is the same as the SPS one: bursts containing at most 2×10^8 particles, are extracted every 14 – 48 seconds from the SPS. This timing is shown in Fig. B.5a in Appendix B.1 for one run taken during the September test beam.

The events triggering is provided by the coincidence of several fast scintillators upstream the tracking and timing detectors. Their arrival time distribution is determined by the SPS super-cycle (the shortest period for a cycling beam sequence).

4.5.2 `GasToF` *timing capabilities*

As a beam particle reaches the scintillator, thus triggering an event through the logical coincidence of the detectors quoted above, a hits search window is opened around this trigger. Hence, if one signal is extracted inside this time window from any channel connected to the DAQ, it is collected by the TDC and stored as a two timestamps, referring to the leading and trailing edges. These quantities are defined with respect to this window.

A first preliminary study can be performed on the timing distribution of all hits. For instance, one can see in Fig. 4.19 the frequencies spectra for all leading edges observed in a given time window, combining all 32 inner channels composing the central disk[9].

One can immediately see the high frequency peak at 43.51 ± 1.91 kHz, and correlate it with the revolution frequency of the beam inside the accelerator itself. If one considers a burst of particles with a momentum p, the revolution frequency in a circular accelerator with a circumference L is:

$$f = \frac{v}{L} = \frac{c}{L}\left(1 + \left(\frac{mc}{p}\right)^2\right)^{-1/2} .$$

[9] The division of the full 64 channels coverage in two groups of 32 channels (the outer ring, and the central disk) is pictured in Fig. B.6.

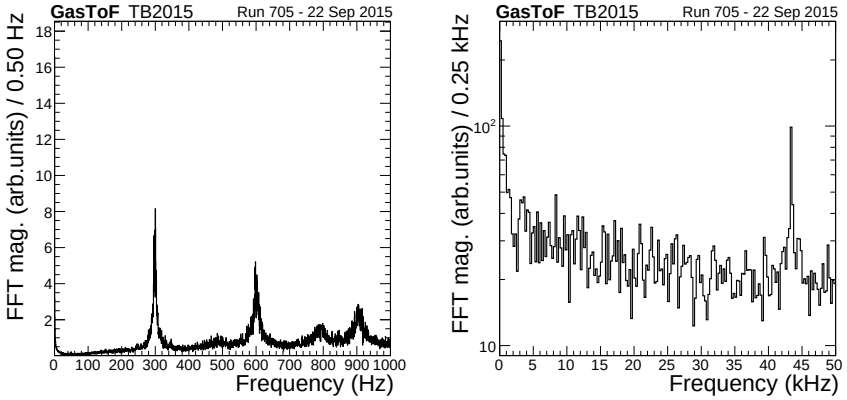

(a) Low frequency domain (b) High frequency domain

Figure 4.19: Frequency spectrum for leading edges observed in central GasToF channels during the Sep 2015 test beam at SPS.

Knowing the mean momentum for the proton beam, $p = 180$ GeV, and $m = m_p$, one can hence reconstruct the SPS length out of this peak position:

$$L_{\text{SPS}}^{\text{reco}} = (6.890 \pm 0.302) \times 10^3 \text{ m},$$

compatible with the actual SPS length, $L_{\text{SPS}} = 6.912$ km.

The runs collected during this test beam are still analysed at the time of this thesis writing. The full timing capabilities of both the GasToF and Quartic prototypes used there will be released in a dedicated note to appear in a short pace.

4.6 MEASUREMENTS OF $\gamma\gamma \to W^+W^-$ WITH THE CT-PPS

With its installation in the cavern during the second half of 2016, the CT-PPS will enable to increase the sensitivity of several searches formerly performed with the central detector only. Among such processes, one may evaluate the overall gain to be expected from this additional information in the search for $\gamma\gamma \to W^+W^-$ events as described in the former chapter. This study was performed in [111].

With the new beam conditions introduced at LHC's early Run-2, the exploratory search for $\gamma\gamma \to W^+W^-$ reactions was performed at a proton-proton centre of mass energy of $\sqrt{s} = 13$ TeV. The total statistics corresponds to an integrated luminosity of 100 fb^{-1}, as an expected baseline for the whole Run-2 acquisition period.

The two-W system was also probed in its fully-leptonic decay, as in the central CMS analysis quoted in chapter 3. The central selection is left unchanged: an isolated,

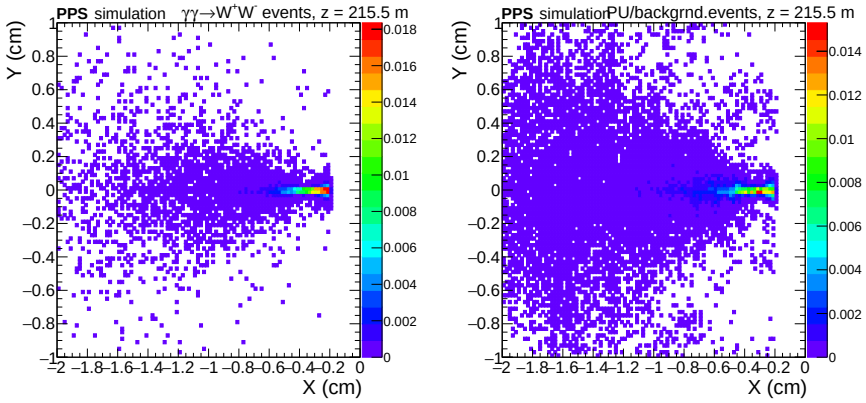

(a) Signal protons (b) Pileup and background protons

Figure 4.20: Expected density of scattered protons at $z = 215.5$ m when a $\gamma\gamma \to W^+W^-$ event is produced in the central system. The absolute yield is given per event.

opposite-charge electron-muon pair, where the two leptons are originating from the same primary vertex (as reconstructed with the central CMS vertexing algorithms), is to be observed at a single lepton's minimal transverse momentum/energy of 20 GeV. Furthermore, they are required to fall in the central acceptance, thus within $|\eta(e,\mu)|< 2.4$, and satisfy a tight muon/medium electron identification.

The simulated signal samples (both the SM and anomalous predictions) quoted in the next sections are generated using `FPMC`, the *Forward Physics Monte Carlo generator* [133]. This latter is quoting the same amplitude as the `CalcHEP` implementation used in chapter 3. Both the $W^{\pm}$ are decayed into an electron, a muon and the two associated neutrinos through `Herwig` [134]. The outgoing protons are propagated to the forward detectors through the whole beamline chain, using the technique described in section 4.4.1.

In Fig. 4.20, the distribution of both the SM signal and pileup components is given at a fixed $z = 215.5$ m, roughly corresponding to the timing detectors location.

One can furthermore include in the simulation the timing information as reconstructed by the two timing stations. In particular, the physical parameter of interest is the time difference between the two detections. This quantity allows to reconstruct the position of the primary vertex along the z axis using a time of flight method, as described in section 4.2 and shown in Fig. 4.21. The precision reached by this technique is determined primarily by the timing resolution of each single timing detector.

In both the signal and background components shown in this figure, this resolution is assumed to reach the 10 ps foreseen by the `CT-PPS` in its current technical design.

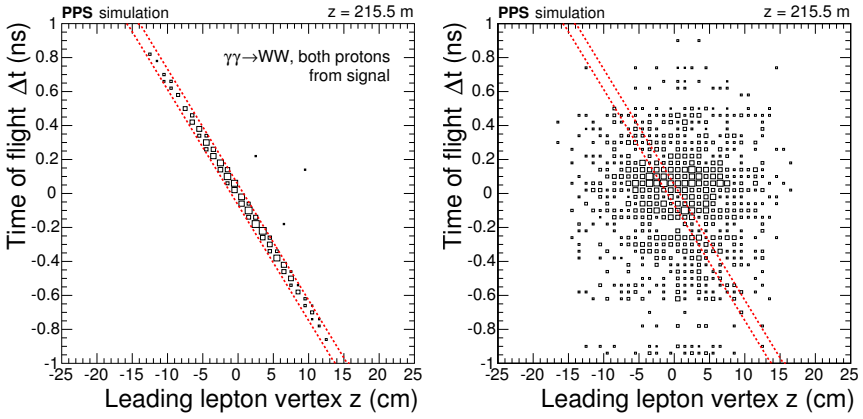

Figure 4.21: Correlation between the proton time of flight as observed in the forward region for a 10 ps resolution timing detector, and the vertex z position for the leading lepton in the event. This distribution is given for the SM $\gamma\gamma \to W^+W^-$ signal and its main source of background (inclusive W^+W^-). No selection is performed on the central system. Figures extracted from [111].

If one returns to the analysis developed in chapter 3, one may recall that the major source of background to be expected in the signal region is the inclusive $W^{\pm}$ pair production, producing a similar final state as observed by the central detector. On the rhs. Fig. 4.21, it is shown to be highly reduced while combining both the central z position of the leading lepton vertex, and the proton time of flight into a well-defined search window (dashed lines).

Depending on the timing resolution reached by the combined timing detectors, this first new handle enables to reduce the main inclusive background by a factor of 5 (resp. 10) with a timing resolution of 30 ps (resp. 10 ps).

It also allows to loosen the exclusivity condition defined in the purely central study described earlier, while allowing additional tracks to be associated to the dilepton system. In this study, the upper multiplicity was therefore restricted to 10 extra tracks.

In addition to the proton time of flight and transverse position, several other fundamental observables listed above are also accessible with the spectrometer installed in the very forward region.

For instance, a direct relation between the energy lost in the central system and the final particle transverse position can be observed at a given distance from the interaction point. In Fig. 4.22, this correlation between the energy loss in the central system and the horizontal deviation in the beam transverse plane at a given z = 215.5 m

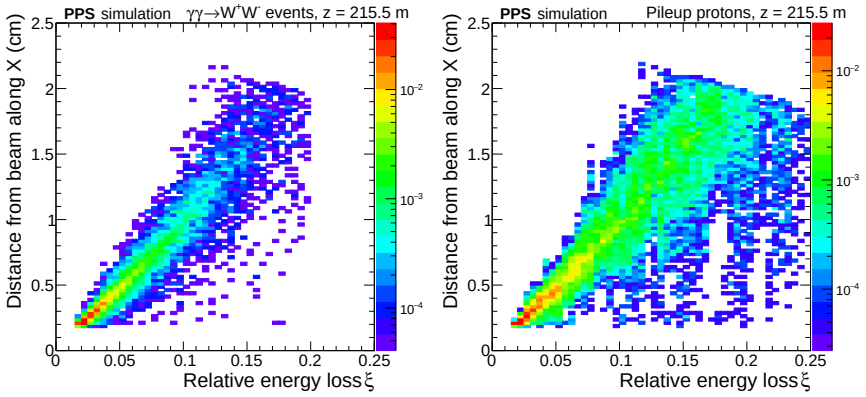

Figure 4.22: Effect of the relative energy loss ξ on the proton horizontal deviation with respect to the nominal beam position. Lhs. figure is for the $\gamma\gamma \to W^+W^-$ signal protons, rhs. figure is for the simulated pileup protons.

is pictured for both the $\gamma\gamma \to W^+W^-$ signal proton and the surrounding pileup event, using the simulation scheme described earlier.

Consequently, a tagging and tracking capability introduced in this region would enable not only to "see" the outgoing protons defining a central exclusive production, but also characterise with a given resolution its total energy lost in the central system.

In a two-photon reaction such as the $\gamma\gamma \to W^+W^-$ process studied here, this loss is therefore linked to the centre of mass energy of the two-photon system. Indeed, using the proton tag one can reconstruct $w_{\gamma\gamma} = \sqrt{\xi_1\xi_2} \cdot \sqrt{s}$ as a "missing mass". This quantity can hence be over-constrained by both the observables reconstructed in the central system (for instance, one can compare it to the dilepton invariant mass in the case of an elastic two-photon production of lepton pairs) and the ones arising from the forward spectrometer. The background rejection power of such a quantity in the $\gamma\gamma \to W^+W^-$ study at $\sqrt{s}$ = 13 TeV at is shown on the lhs. of Fig. 4.23.

Another characteristics of this detection principle is the dependence of the overall signal-to-noise ratio to the detector position itself. This property is linked to the fraction of the total cross section which can enter the timing detector acceptance, as shown on the rhs. part of Fig. 4.23. Indeed, the closer the detector can approach the beam, the better is its coverage of the full allowed kinematic.

The requirements listed above are combined into an expected yield of 3 SM $\gamma\gamma \to W^+W^-$ candidates (including the fully leptonic decay branching fraction) to be observed (using all the kinematic information available) with 100 fb^{-1} of data collected at 13 TeV. It was also evaluated for two anomalous points at the edge of the one-dimensional Run-1 sensitivity, setting a_0^W/Λ^2 or a_C^W/Λ^2 to 5×10^{-6} GeV^{-2} while

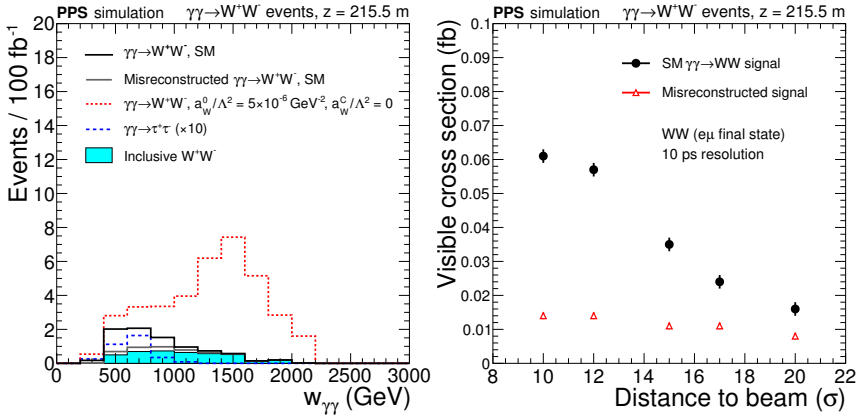

Figure 4.23: Missing mass distribution as reconstructed by the central+forward detectors, and SM $\gamma\gamma \to W^+W^-$ signal-to-background performances with respect to the timing detector distance of approach (with an assumed resolution of 10 ps). Figures extracted from [111].

leaving the other at 0, to give an overall yield at the order of $10 - 30$ events.

The performance of this full selection can be extrapolated to provide upper limits on the observation cross section of this process within the CT-PPS acceptance, hence on both the anomalous parameters. As shown in Fig. 4.24, the expected sensitivity increase reaches two orders of magnitude with respect to the fully central analysis performed at Run-1.

Multiple final states of increased complexities may also be used to furthermore constrain the limits. For instance, one direct combinatorics increase induced by this loosened track-based exclusivity selection can be opened through the semileptonic decay of the $W^\pm$ gauge boson pairs.

4.7 OUTLOOK FOR CT-PPS PHYSICS POTENTIALS

In addition to the large increase in the sensitivity to anomalous $\gamma\gamma W^+W^-$ couplings quoted above, a broad range of two-photon processes will also be reachable experimentally using this forward spectrometer. One can divide the list of potential studies in which the CT-PPS would allow an increased sensitivity following the classification of exclusive processes developed in section 1.2.

In particular, for the two-photon processes emphasised in this thesis, one can quote the exclusive $\gamma\gamma \to W^+W^-$ production described above, or the increased sensitivity expected in the observation of purely neutral final states, such as the $\gamma\gamma \to ZZ$ reaction described in chapter 3 or the study of the $\gamma\gamma \to \gamma\gamma$ couplings in the searches

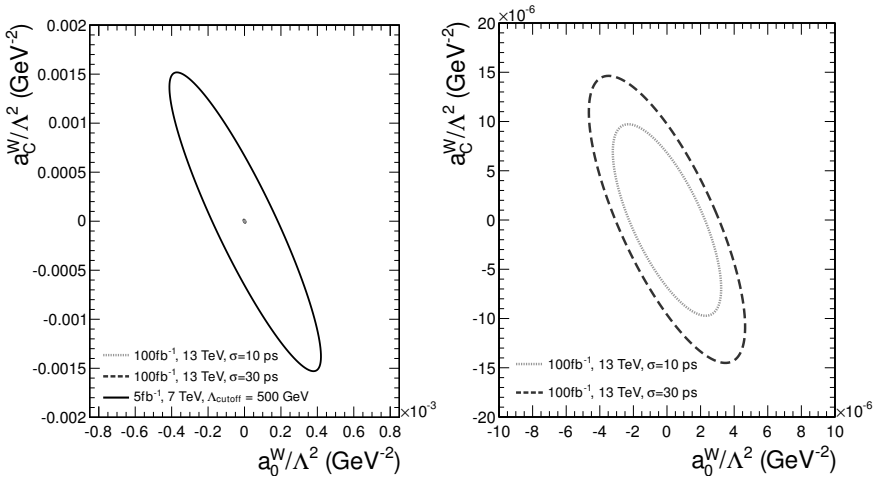

Figure 4.24: Left: Comparison between the observed limits in 2011 data at $\sqrt{s} = 7$ TeV (plain black line), and the expected limits for two scenarios of a measurement at 13 TeV using the CT-PPS spectrometer. Right: Closeup of the effect of the two timing resolution scenarios. Short-dashed line gives the prediction for an optimistic 10 ps timing resolution, while the long-dashed line uses a more reasonable resolution of 30 ps. Figures extracted from [111].

for exotic particles (such as the graviton, or Higgs bosons for instance) and interactions.

Also, for the double pomeron exchange mechanism, an increased selection efficiency in the exclusive di-jets production, described in details in [111] is to be predicted through the addition of this apparatus. Among the precision studies allowed in this channel, one can quote a novel approach to probe the Higgs bosons couplings to heavy or light quark pairs, or an experimental measurement of the pomeron exchange properties leading to a better description of its coupling to proton components. In particular this study would be performed in a region of transition between non-perturbative and perturbative QCD, and for the first time with the measurement of the scattered proton.

In other processes, one can for instance expect an increased sensitivity to any electroweak resonances photoproduction searches through the full determination of the central system energy using both the proton energy losses ξ_i, with $M_X = \sqrt{\xi_1 \xi_2 s}$ the central system energy. The CT-PPS mass acceptance for the baseline solution being restricted to $M_X \gtrsim 300$ GeV, the intermediate resonance offered by the Z production is restricted to boosted events.

Last but not least, the single tagging capabilities of this detector will introduce an innovative way of probing the inelastic and dissociative regimes of central exclusive processes. For instance, if one returns to the two-photon production of lepton pairs

described in details in this thesis, the single-dissociative contributions will potentially be selected through the requirement for one single forward proton tagging, the other one being dissociated in the final state.

CONCLUSIONS AND PERSPECTIVES

In the scope of this work, several aspects of the study of exclusive two-photon processes at a proton-proton collider were developed.

At first, an overall picture of the commonly used theoretical frameworks to characterise these interactions was given. Assuming that the outgoing protons are not observed experimentally, three final states need to be considered in each of these processes: the elastic, and the dissociation of one or both the protons in the final state.

This allowed to introduce the formalism of proton structure and parton density functions and their contribution to the dissociative final state to be observed within a collision experiment. Two of these parameterisations of the proton structure function were studied in accordance in the $\gamma\gamma \to \ell^+\ell^-$ process: the *Suri-Yennie* and the *Szczurek-Uleshchenko*. While the low-Q^2 energy transfer through virtual photons is better modelled by the first, the second (with its DGLAP treatment of the parton evolution) is fitting towards the experimental data at high-Q^2.

A novel approach in the field of two-photon physics was also introduced. It provides a finite prediction to both the elastic and inelastic contributions of the $\gamma\gamma \to \ell^+\ell^-$ process through the k_T-factorisation technique. This approach enables the photon fluxes to be separated from the hard two-photon process in the numerical integration of its matrix element.

In the scope of this development, we integrated the full matrix element in a simulation tool, `pptoll`. This software provides both the total generation cross section, along with an events generator enabling a direct comparison with other approaches, inside any range of kinematic cuts.

In a second part, the observations of such two-photon processes were reported at LHC energies within the CMS experiment. Two final states were probed: the dominant "standard candle" $\gamma\gamma \to \ell^+\ell^-$ (especially its muon component), and the next-to-dominant $\gamma\gamma \to W^+W^-$ process, with a full dileptonic decay of both the Ws.

This was made possible through the outstanding tracking and vertexing capabilities of the CMS detector, allowing to define a track-based condition constraining the phase space and reject a good fraction of all inclusive backgrounds resulting in the same final state. This condition is ensuring the central system of interest (as observed in the extremely noisy environment of a hadrons collider), to be clearly separated from any additional track on its primary vertex.

Moreover, we investigated the current discrepancy between the simulated and observed vertex tracks multiplicity, and furthermore deteriorated with the increase of this centre of mass energy. This discrepancy, implying an improper modelling of the

exclusivity selection in the overall simulation scheme, was shown to be independent from the pileup conditions, and our study of the vertexing and tracking variables allowed us to rely on a data-driven efficiency rescaling of this region of interest.

The high statistics collected at $\sqrt{s} = 7$ and 8 TeV by the CMS experiment, in which two isolated muons are detected allowed to extract a big sample of such $\gamma\gamma \to \mu^+\mu^-$ events to study its behaviour in different region of its phase space. Among these studies, we estimated an overall rescaling to apply on a purely elastic contribution, to account for the inelastic components. Given a phase space of interest, we computed this "*F*-factor" from the dilepton process observation in this very same kinematics.

It was estimated for two leptons with $p_{\mathrm{T}}(\text{single } \ell) > 20$ GeV, $|\eta(\text{single } \ell)| < 2.4$, and $m(\ell\ell) > 160$ GeV to 3.23 ± 0.5 (stat.) (resp. 4.10 ± 0.43 (stat.)) at $\sqrt{s} = 7$ TeV (resp. 8 TeV, combining both the dielectron and dimuon channels).

A search for two-photon production of $W^{\pm}$ gauge boson pairs was then performed at these two proton-proton centre of mass energies. The primary goal for this study was to shed light on anomalous behaviours of the $\gamma\gamma VV$ coupling as defined in the framework of *anomalous quartic gauge couplings* (AQGCs).

Restricting the analysis to the lepton decay of both the *W*s, the selected final state is a pair of opposite-sign, different flavour leptons with the same fiducial cuts as defined above for the dilepton process.

In the signal region (dilepton invariant mass above 20 GeV, pair transverse momentum above 30 GeV), 2 (resp. 13) events were observed at $\sqrt{s} = 7$ TeV (resp. 8 TeV), with an expected background of 0.84 ± 15 (resp. 3.5 ± 0.5) events. Both these observations are consistent with the Standard model couplings prediction, with a combined significance over the background-only hypothesis of 3.7σ. One may emphasise that this observation was the first one ever performed experimentally.

This upper limit on the production cross section was then translated in constraints on the dimension-6 and 8 AQGC parameters (the latter can be found in chap. 3):

$$-1.0 \times 10^{-4} < \left(a_0^W/\Lambda^2\right) < 1.0 \times 10^{-4}\ \mathrm{GeV}^{-2},$$
$$-3.7 \times 10^{-4} < \left(a_C^W/\Lambda^2\right) < 3.1 \times 10^{-4}\ \mathrm{GeV}^{-2},$$

with a form factor ensuring the unitarity of these predictions ($\Lambda_{\mathrm{cutoff}} = 500$ GeV, $p = 2$), or

$$\left|a_0^W/\Lambda^2\right| < 1.2 \times 10^{-6}\ \mathrm{GeV}^{-2},$$
$$\left|a_C^W/\Lambda^2\right| < 4.2 \times 10^{-6}\ \mathrm{GeV}^{-2},$$

without any form factor. These limits are respectively 2 and 3 orders of magnitude more stringent than the previous attempts at LEP, and remain the tightest nowadays while including the modern inclusive approaches.

Furthermore, we studied the two-photon production of Z boson pairs using the full 2012 dataset collected at $\sqrt{s} = 8$ TeV, with one Z boson decaying fully leptonically into dimuons and the other into an invisible neutrino-antineutrino pair. The major source of background for this high-virtuality exclusive study being the semi-exclusive and fully-inelastic two-photon production of lepton pairs, we introduced a data-driven method to parameterise the contamination to be expected for this contribution.

Selecting a signal region in which the lepton pair is produced within the Z mass range, and with a transverse momentum sufficiently high to suppress the background components, an upper limit on the anomalous behaviours of the quartic $\gamma\gamma ZZ$ coupling was estimated for this technique. These limits are predicted to be two orders of magnitude more stringent than any previous attempt.

Finally, as a way to increase the overall sensitivity to these processes, and mitigate the steady worsening of the central event clarity due to secondary proton-proton interactions (or pileup), the CMS-TOTEM *Precision Proton Spectrometer* was described.

Expected to be installed in the second half of 2016 in the very forward region of the CMS interaction point, this set of timing and tracking detectors will allow to tag and reconstruct the outgoing proton kinematics, thus ensuring a full description of the whole event within a collision. The update of this search for $\gamma\gamma \to W^+W^-$ in the perspective of increasing its sensitivity to AQGCs was presented, following a Run-2 scenario in which 100 fb^{-1} of data would be collected at a centre of mass energy $\sqrt{s} = 13$ TeV.

Among the possible timing detectors, the `GasToF` *R&D* project was studied. As a Cerenkov detector, it can rely on both a fast signal creation, ensuring a picosecond-scale time resolution, along with an operability in radiation-hard environments. Recently tested along with a full data acquisition chain at a test beam in CERN's SPS, it will show promising results which could lead towards its installation in the spectrometer, either as a short version for the Roman pots, or in a larger scale for fitting in the moveable beam pipes scenario. For this test beam, we were involved in the design and construction of the of both on the electronics readout chain for the `GasToF`, and on the data acquisition software parts.

Appendices

A

CEPGEN: A GENERIC $PP \to PXP$ GENERATOR

Over the last three decades, a piece of code was able to provide a reasonable agreement with an ever-increasing amount of data collected in various colliding experiments. Unfortunately, its structure got harder and harder to maintain, hence an updated version of this code was released.

A.1 MOTIVATIONS

LPAIR is a MC generator allowing to simulate the $\gamma\gamma \to \ell^+\ell^-$ process, while involving the exchange of two photons originating from primary particles (either electrons, or protons), and coupling in a pure QED scheme to these outgoing leptons. It originates from a matrix element level software developed by J. Vermaseren[44] in early 1980s, and propagated by Baranov *et al.* to HERA's H1 (and later ZEUS) simulation software [43][1].

Its major feature is the high care given to all numerical parts inserted into this code. Indeed, most of the total cross-section is concentrated in very low values of the photons' momentum. This kinematic characteristic of the $\gamma\gamma \to \ell^+\ell^-$ process is hence involving a proper integration in regions where the photon propagator, behaving as $1/Q^2$, contributes to very large values. The whole code structure, as well as the full mathematical formulation of the matrix element, has therefore been optimised to ensure its high numerical stability (as seen in section 1.3.1).

The main challenge in releasing an updated version of this code was to ensure this later point all along the program flow, even though a new programming paradigm would change it significantly. C++ was chosen as a base programming language, mostly for its steadily growing developers community in HEP.

One may emphasise that the vast majority of this code was written in a train while this task was left as a secondary project. It is hence enabled to thank warmly the Belgian national train company for the quality of its service, making it possible to spend a big amount of time for all cross-checks and code optimisation (see Fig. A.1).

[1] A version of this MC generator can be retrieved at [135].

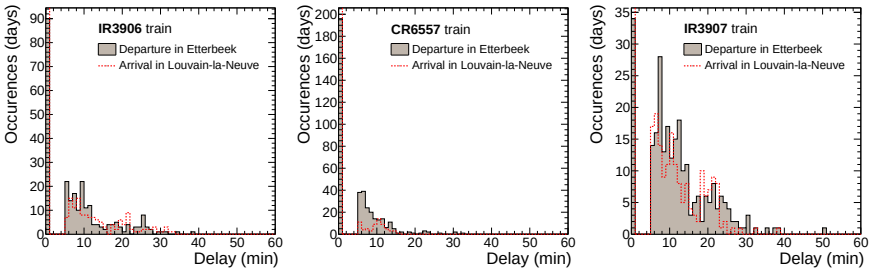

Figure A.1: Distribution of delays for the Belgian trains connecting *Etterbeek* to *Louvain-la-Neuve-Université* stations in a range between the 23rd November 2013 and the 12th February 2015. Delays between 1 and 5 minutes are combined to the first bin (no delay).

A.2 PROGRAM STRUCTURE

Despite its primary goal to act as a modern replacement for `LPAIR`, this code relies on a brand new structure developed in an attempt to transform it into a process-independent software. The full reference manual containing all relations between all objects defined in here can be found in [136].

One can distinguish three main parts in this updated code structure: a multi-dimensional integrator coupled to an events generator, an object containing the matrix element for any process to simulate, and a hadronisation tool for the outgoing state fragmentation.

In technical words, the end user interacts through a central `MCGen` object to integrate over a user-defined region of the phase space the matrix element provided by a `GenericProcess`-inherited object. Optionally, it can also enable the fragmentation of outgoing state particles (for instance, the incoming proton remnants in the case of an inelastic pp collision) through a `GenericHadroniser`-inherited class.

This integration is performed by a C implementation of the *Vegas* algorithm[51] provided by the *GNU Scientific Library*, or GSL[137]. It relies on the importance sampling of random points to propagate to the function to be integrated. These points are selected to be concentrated in regions of the phase space contributing to the largest fractions of the integral to be computed.

To extract these high contribution points, the function is therefore binned according to its dimension multiplicity, and an iterative procedure runs over this n-dimensional histogram to define a sampling distribution for the next pass. For computational purposes, the assumption is made that this integrated distribution can be approximated by a separable function, *i.e.* $f(x_1, \dots x_n) = \prod_{i=1}^{n} f_i(x(i))$.

Therefore, if any, the peaks composing the function to be integrated need to be as separated and well-localised as possible . This method allows to reach a good estimate of the integral while keeping the iterations number very low.

Furthermore, the events generation part relies on this very integration grid, and the *hit-or-miss* rejection method developed by von Neumann [138] enables to generate a collection of unweighted events which can be propagated to any detector simulation algorithm.

Technically, the `GenericProcess` object is required to contain at least these four public methods for the events generator to run successfully:

`void GenericProcess::AddEventContent()`, a method to sets the list of incoming and outgoing particles expected to be produced in the process.

`unsigned int GenericProcess::GetNdim(GenericProcess::ProcessMode)const`, a constant method to retrieve the number of dimensions on which the integrator needs to run. One optional input argument is provided, an integer representation of the outgoing primary particles' kinematics (elastic scattering, or proton dissociation for instance),

`double GenericProcess::ComputeWeight()`, a method providing a double precision floating point weight for each point in the phase space to be considered,

`void GenericProcess::FillKinematics(bool)`, a method to be called to fill the `Parameters::last_event` object if events generation is to be performed. This object is an `Event` class, a set of `Particle` objects, keeping track of their nature, kinematics, and parentage. The optional boolean argument specifies if the outgoing state needs to be symmetrised with respect to the z coordinate.

Furthermore, if the fragmentation of the incoming particles' remnants is requested, a `GenericHadroniser`-inherited object can be run as well. It operates on the `Event` class, extracts the partons to be hadronised given a special tag introduced at the `Event` composition, and generates the complete list of final state particles with their parentage. Currently, two string fragmentation hadronisers are in production:

- `Jetset7Hadroniser` (used as a legacy component to check its backwards compatibility with `LPAIR`) relying on `Jetset` [47], and
- `Pythia6Hadroniser` relying on the `Fortran` versions of `Pythia` [97] (hence, up to its version 6).

The `Herwig` cluster fragmentation algorithm is still under development, and should be added to the baseline code in a short pace.

A simple example is shown in Fig. A.2 for the generation of one hundred $\gamma\gamma \to \mu^+\mu^-$ events, where one of the two incoming protons is fragmented in the final state.

In this minimalistic piece of code, one can immediately pick out three orthogonal parts:

```
#include "includes/MCGen.h"

using namespace CepGen;

int main(int argc, char* argv[]) {

  // First we initialise the generator core
  MCGen mg;

  // ----- Parameters definition
  Parameters* param = mg.parameters;

  // We use the lepton pair photoproduction process
  param->process = new GamGamLL;

  // The outgoing lepton pair is muons
  param->pair = Particle::Muon;

  param->in1pdg = param->in2pdg = Particle::Proton;
  param->in1p = param->in2p = 6500.; // in GeV
  // The first outgoing proton is set to be dissociated, while
  // the second outgoing proton is kept intact
  param->process_mode = GenericProcess::InelasticElastic;
  // Suri-Yennie proton form factors
  param->remnant_mode = GenericProcess::SuriYennie;

  // Single outgoing leptons' kinematic cuts
  param->mineta = -2.5;
  param->maxeta = 2.5;
  param->minpt = 5.; // in GeV

  // We use Pythia6 as the events hadroniser
  param->hadroniser = new Pythia6Hadroniser;

  // ----- Definition and integration over full phase space

  // Cross-section computation for the process
  double xsec, err;
  mg.ComputeXsection(&xsec, &err);

  // ----- Events generation

  // Generation of 100 events
  for (unsigned int i=0; i<100; i++) {
    Event* ev = mg.GenerateOneEvent();
    ev->Dump();
  }
  return 0;
}
```

Figure A.2: A minimal code snippet for the generation and the text display of 100 single-dissociative $\gamma\gamma \to \ell^+\ell^-$ events through CepGen, following the same cuts on the phase space as defined in the text.

```
PROC lpair
MODE 3     # elastic-inelastic
HADR pythia6
IEND 3     # events generation
NGEN 100   # generate 100 events
PMOD 11    # SY structure function
INPP 6500.
INPE 6500.
PAIR 13    # muon pairs
MCUT 2     # cuts on both the muons
PTCT 5.    # minimum single muon pt
ECUT 0.
ETMN -2.5  # single muon eta range
ETMX 2.5
```

Figure A.3: Example of a configuration card to be used for the production of 100 single-dissociative $\gamma\gamma \to \ell^+\ell^-$ events using the LPAIR matrix element with CepGen.

DEFINITION of the process type and kinematics (all these quantities/references are stored in the `Parameters MCGen::parameters` object definition),

COMPUTATION of a total cross section with its associated error in this phase space (the call to a public method `void MCGen::ComputeXsection(double*, double*)`),

GENERATION of unweighted events, done within a loop (performed through the set of `Event* MCGen::GenerateOneEvent()` function calls).

The main user may also use his own configuration file, following the same format as the one fed by the original LPAIR code (a 4-letter key, directly followed by a space and a string/integer/float value). For instance, as a mean to reproduce the very same cross section evaluation and events generation as performed in the minimal working example, one may use the configuration card given in Fig. A.3

A.3 VALIDATION WITH LPAIR

Among the various techniques allowing the validation of this new framework with the former Fortran77 version of LPAIR, it was chosen to evaluate the total generation cross section for a "realistic" set of kinematical constraints. This relatively loose collection of cuts is chosen to reflect the fiducial region observed at any of the LHC experiments, namely:

- $\ell^\pm = \mu^\pm$ as a matter of convention, as this process was studied earlier,
- $p_\mathrm{T}(\text{single } \mu) > 5$ GeV, $|\eta(\text{single } \mu)| < 2.5$, compatible with CMS fiducial region,
- a photon virtuality range $0 < Q^2 < 1 \times 10^4$ GeV^2,

- in the case of dissociated protons, $1.07 < M_X < 10^3$ GeV.

In Fig. A.4, this comparison for the total generation cross section $\gamma\gamma \to \mu^+\mu^-$ signal is performed as a function of the single outgoing leptons' transverse momentum. The three outgoing proton states are considered here: the elastic-elastic, the elastic-inelastic, and the inelastic-inelastic components. The "DESY " version of the `LPAIR` code was used for the first two sub-processes, while the updated "CDF " version was used for the latter, being the only one including this component.

A.3.1 $\gamma\gamma \to \ell^+\ell^-$ *distributions*

Given the program structure as described above, one can then generate in a simple way any set of events in any part of the phase space.

The results are in good agreement, as pictured in Fig. A.5 for three differential cross-section distributions: the outgoing leptons' invariant mass, the vector sum of their transverse momentum, and their acoplanarity (or angle opening in the transverse plane). The rhs. figures display the `CepGen`/`LPAIR` ratio for these distributions.

Given this reasonable agreement observed for the $\gamma\gamma \to \ell^+\ell^-$ process, the simulation of additional central exclusive processes can be considered using this generic simulation tool.

A.4 PROCESSES SIMULATED (AND SOON TO BE ...)

Several processes of interests are foreseen to be integrated in a near future within this simulation scheme. One can quote, for instance, the two-photon production of charged Higgs boson pairs[28] (where the scalar nature of outgoing particles gives a relatively easy matrix element to simulate), or the more complex two-photon production of $W^\pm$ or Z gauge boson pairs, using the formalism recently introduced in [139].

For this later case, one can count on the fruitful and promising collaboration built around the study of the k_T-factorisation method described earlier. This latter was established with experts from PAN Kraków (Poland), and numerous results are to be expected in a short pace.

In addition to these two-photon processes, the diffractive meson photoproduction is soon to be integrated into `CepGen`. This implementation is based on `DIFFVM` [140], developed in the late 1990s for the HERA (and especially H1) *ep* physics programme. In a near future, the diffractive *pp* production of these light mesons will therefore be properly simulated for the LHC programme.

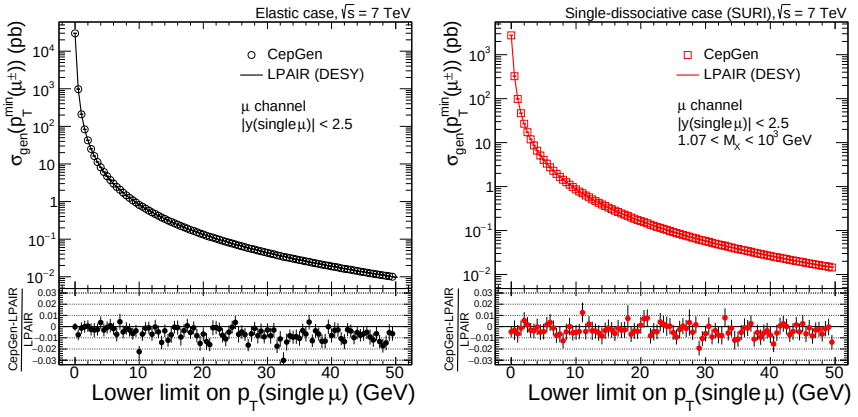

(a) Elastic process

(b) Single-inelastic process

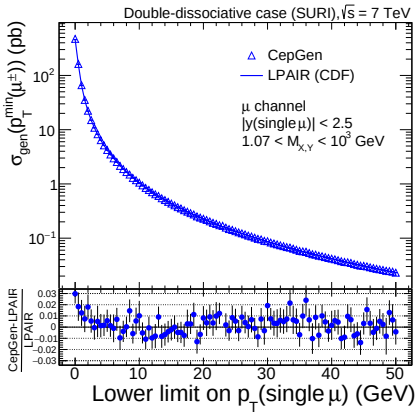

(c) Double-inelastic process

Figure A.4: Total cross section at $\sqrt{s} = 7$ TeV as a function of the minimal transverse momentum cut on single outgoing leptons. The solid lines represents the `LPAIR` prediction, while the open markers depict the C++ code equivalents.

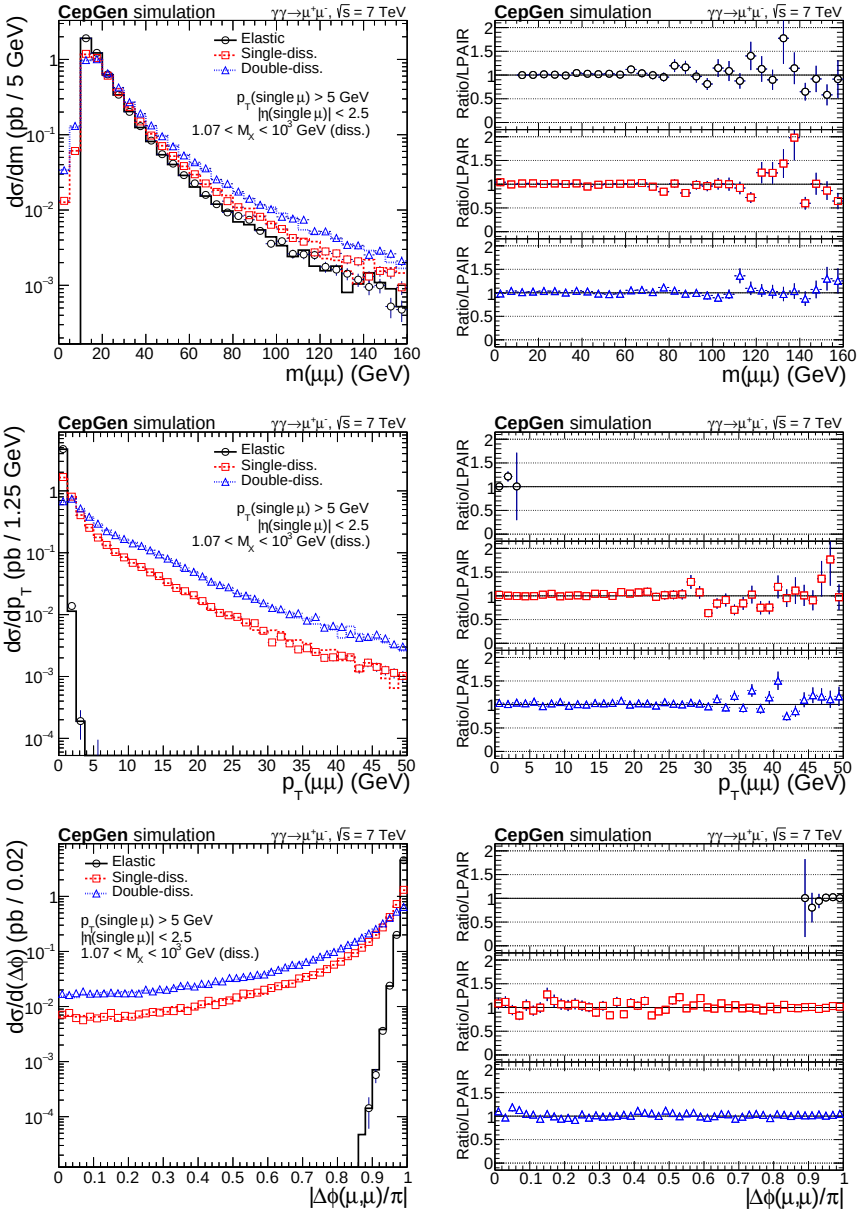

Figure A.5: Comparison of differential cross-sections with respect to three dilepton variables of interest, for 100k elastic, single- and double-dissociative dimuon events with $p_T(\text{single } \mu) > 5$ GeV. Lines in the leftmost plots correspond to the original `LPAIR` code, and markers give the `CepGen` prediction. The rhs plots give the ratio between the new C++ and the older `Fortran` "DESY" and "CDF" versions.

B

DATA ACQUISITION FOR THE CT-PPS

What would be the purpose of a brand new detector like the CT-PPS if nobody could make use of the data it outputs? Behind this rather simple question lies the whole challenge of developing a data acquisition system (or *DAQ*) to extract the biggest fraction of data out of an impressive flow of information.

Two independent DAQs can be described in this part: the one used during Summer and Fall of 2015 for a set of tests of the whole apparatus (or parts of it) under quasi-real conditions, and the final design DAQ to be integrated within the central CMS acquisition protocol.

B.1 TEST BEAM DATA ACQUISITION

The DAQ scheme to be described here is the one used during all test beams operated during the second half of 2015 at CERN's *Super Proton Synchrotron* (SPS). In an attempt to rely on the simplest architecture, the only external library to be kept was the one holding the communication protocol with the different modules composing the VME acquisition scheme.

Therefore, again for the sake of simplicity, its development remained entirely orthogonal to the final CT-PPS DAQ which will be embedded inside the full CMS acquisition framework, XDAQ [141].

As shown in section 4.5, two sets of detectors were tested during this campaign of test beams: the tracking apparatus (three layers of silicon pixels embedded in a common *Roman pots*), and two types of timing detectors (the GasToF described in section 4.3.3, along with two stations of the design Quartic detector). In this appendix, some results will be shown on the timing detectors, and especially on its *R&D* GasToF component.

B.1.1 *Readout components*

Given the tight schedule constraints to be faced for the test beam preparation, a widely used commercial version of the HPTDC chip was chosen for its direct availability and good operational knowledge. This module, a CAEN V1290A as pictured schematically

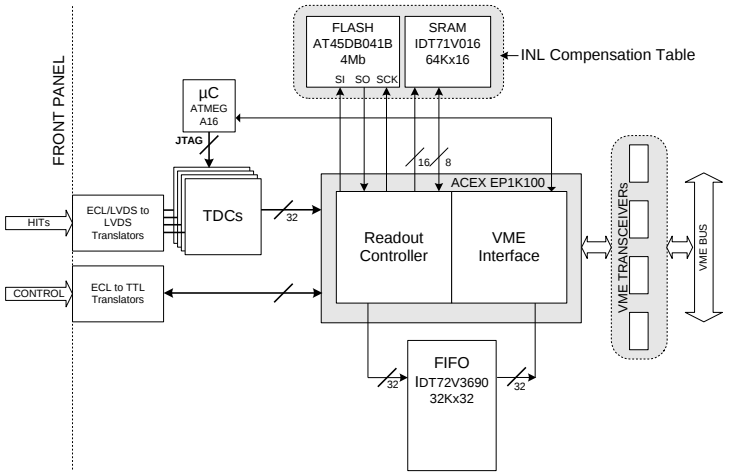

Figure B.1: Block diagram for a CAEN V1x90 series embedded HPTDC module. Figure extracted from [142].

in Fig. B.1, is a standalone component controlled and operated through a VME bus connection. Its inner HPTDC registers are reachable using a micro-controller its programming and events readout. It also provides a 1024 events deep FIFO buffer to be read continuously by the end user (typically with a VME-to-computer bridge). The highest timing resolution claimed by this commercial solution is the same as its embedded HPTDC chip, 25 ps.

To ease the manipulation of a full readout chain from a remote location, a software library described in the following section was developed to control this set of TDC modules, as well as several other boards, as pictured as Fig. B.2.

For instance, the propagation of all external input signals (common clock, trigger arrival pulse, common reset signal) through all parts of the acquisition boards is ensured by another VME board embedding a fully modular FPGA.

In this additional module all input and output ports can be controlled by the user, either using a low-level firmware to be memory flashed via a JTAG interface to the "user FPGA", or permanently programmed through a dedicated software relying on the VME bus communication.

The interface between these firmware and software components is controlled by setting a wide set of internal 32-bit registers to be defined accordingly in both parts of the driver.

Multiple requirements were to be met by this CAEN V1495 "FPGA board" [143] for the purposes of a proper testing and calibration of these HPTDC boards, as well as the operation mode in the actual experimental hall for this test beam, namely the generation/propagation of:

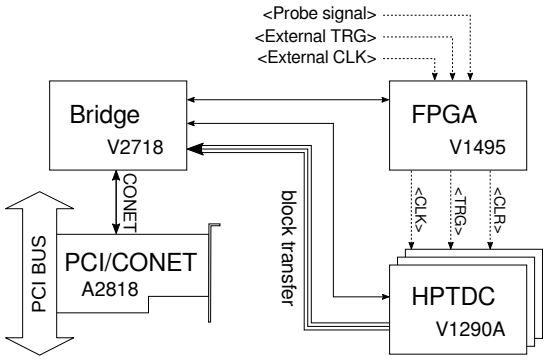

Figure B.2: Layout of the full acquisition chain for the summer-2015 CT-PPS test at H8 beam line (CERN SPS).

- a clock source, typically at the order of 40 MHz frequency, or 25 ns period,
- a common trigger, provided by the tracking detectors data acquisition module after its own triggering at the arrival of each SPS beam train,

through all hardware parts of the DAQ.

The firmware was developed to rely either on external clock and trigger sources (such as the ones provided by SPS during the test beam), but also on a fully "internal" mode, using the user FPGA's inner 80 MHz clock. For all preliminary offline tests performed in lab, this second mode allowed a direct probe of each individual TDC channel and the extraction of their calibration constants.

In addition to this synchronisation device for all HPTDCs, a second module enabled to control the threshold voltage to be applied to the NINO boards through a I^2C communication protocol. Any digital threshold value could therefore be propagated as a value in mV to be stored internally by any NINO chip used in the run.

B.1.2 *Data acquisition*

For an easy interaction between all parts of this DAQ and the end-user, a graphical user interface (GUI), along with several DQM (data quality monitoring) processes, were developed for the purpose of this test beam [144]. A block diagram of the multiple components and their relations is pictured in Fig. B.3.

The configuration of all physical modules within a run was performed using a simple XML file, containing a list of all VME components to be integrated to the readout/control, along with the setting of several local or global run parameters. For

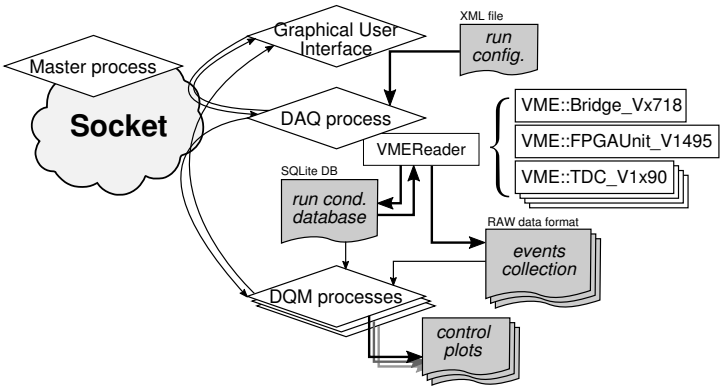

Figure B.3: Block diagram of the test beam's run control architecture. The diamond blocks represent all processe involved in the operation, while the rectangles are the software objects controlling each physical data acquisition module.

instance, three global data acquisition modes could be set in this scheme: the trigger-matching, and continuous storage modes as provided by the standalone HPTDC module, along with an additional trigger mode enabling to open a search window *after* the arrival of each trigger. This latter capability was made possible through the configuration of both the TDC and the FPGA control board.

The GUI was provided as a single window accessible to the end-user, hence providing the few critical information useful to trace any In the conception of this GUI, the whole interface was required to be as "user-proof" as possible. Hence none of the critical values, such as the high voltage settings (bias voltage, and maximal delivered current), are directly editable by the operator through this interface.

For the DQM processes, both detector and DAQ-related vistars were produced either at the end of a run, or at the end of one of its sections (a user-defined multiplicity of triggers, defining a proper statistics to study the beam and detectors behaviours). Hence, each sub-detector or DAQ component was associated to a single process triggered at a given fraction of the run, to provide an user-readable collection of useful vistars.

The communication between all these independent processes was performed through the message-passing capability of system sockets. This architecture ensures an asynchronous communication, *i.e.* the data acquisition process remains independent of any operation potentially hanging each user-controlled process.

B.1.3 *Beam timing structure*

The experimental facility used for this test beam, already described in section 4.5, can rely on a serie of optical modules acting as focussing-defocussing lenses, as pictured in Fig. B.4.

The beam arriving at the experimental hall being extracted from the SPS at a periodic time, several timing features are expected to be observed in the detectors probed.

In general, one ~ 110 seconds super-cycle contains one to three bursts, as seen in Fig. B.5a. As seen in Fig. B.5b integrating the leading edge distributions of all hits for all bursts in a run, one single burst itself has a mean duration of about 3.5 seconds.

B.2 GASTOF ACQUISITION

As described in sections 4.3.4 and 4.3.5, the `GasToF` detector had its signal extracted through a MCP-PMT with an analog-to-digital readout relying on the NINO amplifier and discriminator chips. As a consequence, the 64 channels of the first were mapped to two of the latter modules (each one of them providing 32 readout channels). In Fig. B.6, one can see the mapping introduced to split these channels into two groups.

Again, the geometrical properties of the Cerenkov cone to be developed by a transiting particle were taken into account in the choice of this channel allocation. Indeed, as most of the channels are expected to be illuminated in the central part of the sensitive area, following a circular pattern, and given only 32 channels were to be collected during the first test beam, it was chosen to maximise the signal output of the whole detector.

B.2.1 *PMT gain analysis*

As a preliminary result to characterise the MCP-PMT operational parameters, the signal-to-noise ratio was evaluated for each of the 32 inner disk's cell. The signal component is defined as the highest yield of signal edges per trigger, in a window centered on the expected hits time of arrival. The noise is the pedestal as observed inside the whole hits search region opened before each trigger, and pictured in Fig. B.7.

One can see in Fig. B.8 that this signal-to-noise ratio has a direct dependence with the bias voltage applied on the MCP.

In Fig. B.9, one can see the signal-to-noise ratio, along with its numerator/denominator for the full 64 channels in one single run taken at 2.7 kV. As pictured on this figure, the mean ratio fluctuates between 3 (for the outer ring channels) and 5 (in the higher-occupancy, central cells).

The major fraction of runs collected using the common `GasToF`/`Quartic` DAQ were therefore operating the `GasToF`'s MCP-PMT at its full gain, hence around $V_{\text{bias}} = 2.7$ kV, like the run 697 described in table B.1, and shown in Fig. B.7.

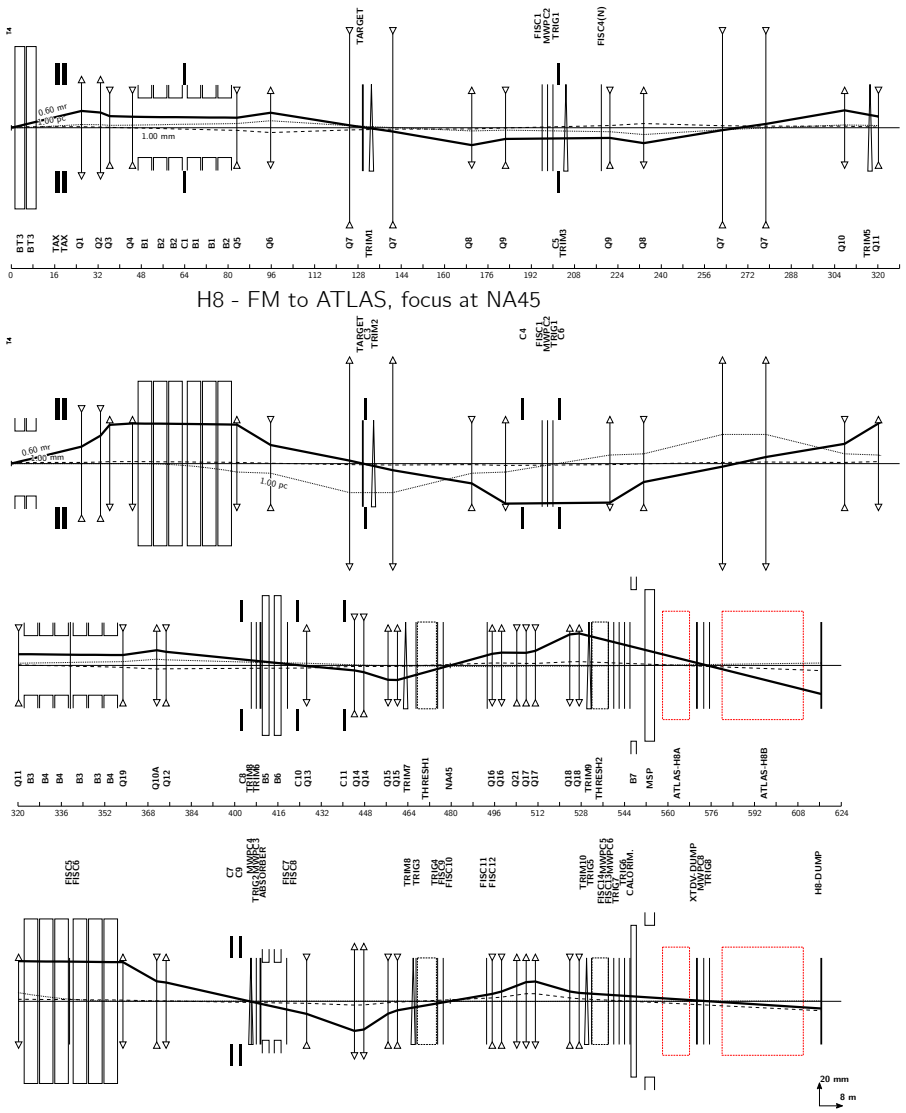

Figure B.4: Optical elements composing the H8 beamline at SPS. The beam path is pictured as a thick black solid line, while the arrowed lines are the quadrupole magnets in charge of its collimation.

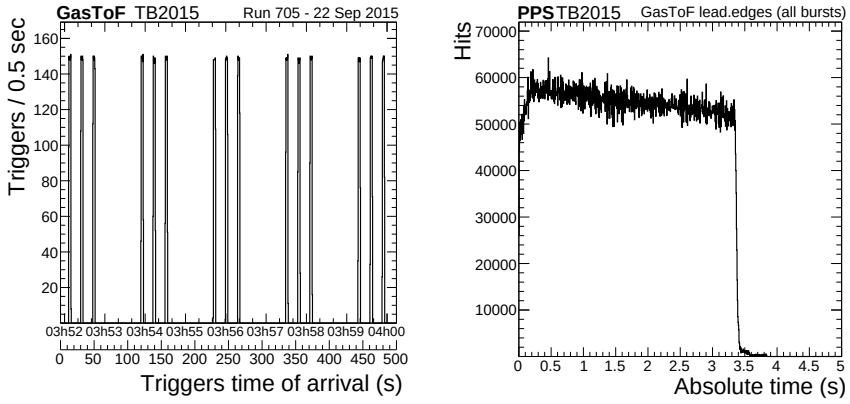

(a) (b)

Figure B.5: Arrival times for (a) each trigger inside a run as seen by the DAQ, (b) each hits inside a burst as seen by all GasToF channels. The burst timing structure is clearly visible in this second view integrating all bursts in the whole run. Data collected during Sep 2015 test beam at SPS.

A_{31}	A_{30}	A_{29}	A_{28}	A_{27}	A_{26}	A_{25}	A_{24}
A_{23}	A_{22}	B_{31}	B_{30}	B_{29}	B_{28}	A_{21}	A_{20}
A_{19}	B_{27}	B_{26}	B_{25}	B_{24}	B_{23}	B_{22}	A_{18}
A_{17}	B_{21}	B_{20}	B_{19}	B_{18}	B_{17}	B_{16}	A_{16}
A_{15}	B_{15}	B_{14}	B_{13}	B_{12}	B_{11}	B_{10}	A_{14}
A_{13}	B_{9}	B_{8}	B_{7}	B_{6}	B_{5}	B_{4}	A_{12}
A_{11}	A_{10}	B_{3}	B_{2}	B_{1}	B_{0}	A_{9}	A_{8}
A_{7}	A_{6}	A_{5}	A_{4}	A_{3}	A_{2}	A_{1}	A_{0}

Beam

Figure B.6: Channel mapping for the 64 channels of the MCP-PMT mounted on the GasToF detector during 2015 test beams at SPS. The two background shades are defining the splitting between the two sets of 32 channels to discriminated and propagated to the DAQ through the two 32-channel NINO modules.

Run #	Trigger	Trig.num.	$V_{\text{bias}}^{\text{GF}}$	$V_{\text{thres.}}^{\text{NINO}}$	Run start
697	Di.	200198	2.7 kV	240 mV	21 Sep 2015 22:33
705	S1+S2	191442	2.7 kV	240 mV	22 Sep 2015 03:51

Table B.1: A list of runs of interests used hereafter for the GasToF test beam data analysis, along with their main conditions.

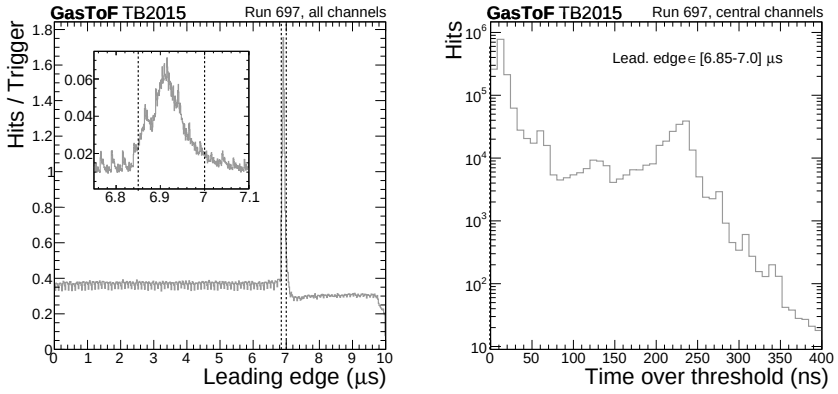

Figure B.7: Events structure for all triggers acquired in a run. Lhs. figure pictures the leading edge time of arrival in the 10 μs window opened before each trigger, while the rhs. figure shows the digital pulse width (or *time over threshold*).

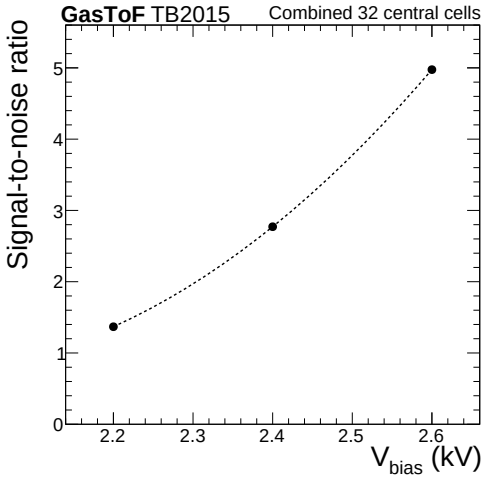

Figure B.8: Measured signal-to-noise ratio for all 32 central disk channels combined, as a function of the MCP-PMT bias voltage.

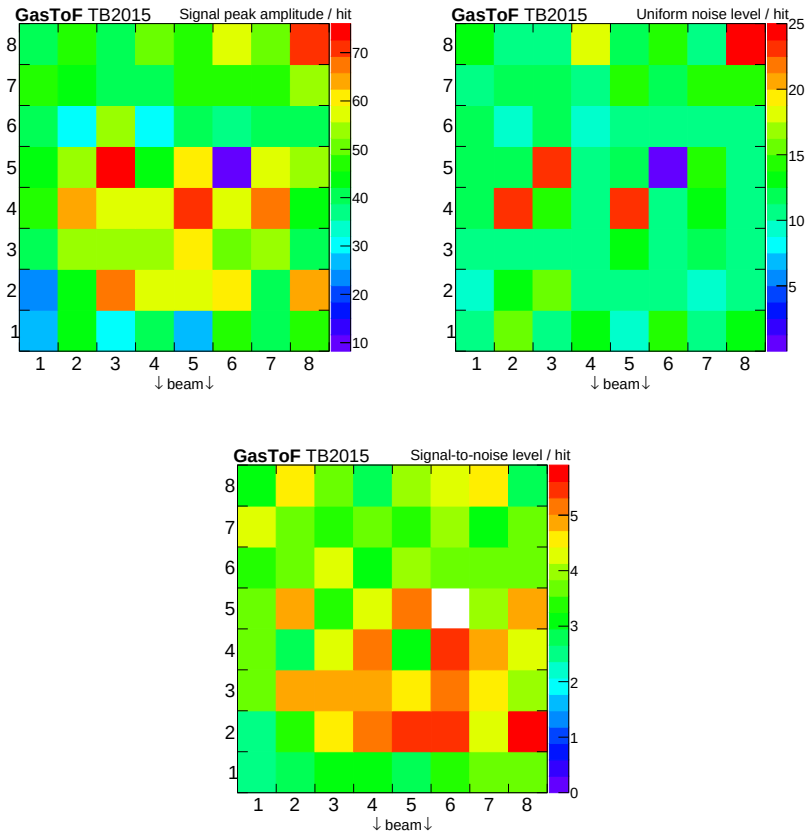

Figure B.9: Normalised noise levels, signal peak amplitude, and their ratio for all 64 GasToF channels as observed in the SPS test beam. In the latter figure, one channel (NINO B, channel 20) is left aside due to its improper cabling.

BIBLIOGRAPHY

[1] H. Geiger and E. Marsden, *The laws of deflexion of a particles through large angles*, *Philosophical Magazine Series 6* **25** (1913), no. 148 604–623, [http://dx.doi.org/10.1080/14786440408634197].

[2] R. P. Feynman, *The behavior of hadron collisions at extreme energies*, *Conf. Proc.* **C690905** (1969) 237–258.

[3] **LHCb** Collaboration, R. Aaij et al., *Observation of $J/\psi p$ resonances consistent with pentaquark states in $\Lambda_b^0 \to J/\psi K^- p$ decays*, *Phys. Rev. Lett.* **115** (2015) 072001, [arXiv:1507.03414].

[4] J. D. Bjorken, *Asymptotic sum rules at infinite momentum*, *Phys. Rev.* **179** (1969) 1547–1553.

[5] **ZEUS** Collaboration, H. Abramowicz et al., *Deep inelastic cross-section measurements at large y with the* ZEUS *detector at* HERA, *Phys. Rev. D* **90** (2014), no. 7 072002, [arXiv:1404.6376].

[6] **H1** Collaboration, T. Ahmed et al., *A measurement of the proton structure function $F_2(x_{\mathrm{Bj}}, Q^2)$*, *Nucl. Phys. B* **439** (1995) 471–502, [hep-ex/9503001].

[7] A. D. Martin, W. J. Stirling, R. S. Thorne, and G. Watt, *Parton distributions for the* LHC, *Eur. Phys. J. C* **63** (2009) 189–285, [arXiv:0901.0002].

[8] V. N. Gribov and L. N. Lipatov, *Deep inelastic ep scattering in perturbation theory*, *Sov. J. Nucl. Phys.* **15** (1972) 438–450. [Yad. Fiz.15,781(1972)].

[9] G. Altarelli and G. Parisi, *Asymptotic freedom in parton language*, *Nucl. Phys. B* **126** (1977) 298.

[10] Y. L. Dokshitzer, *Calculation of the structure functions for deep inelastic scattering and e^+e^- annihilation by perturbation theory in quantum chromodynamics*, *Sov. Phys. JETP* **46** (1977) 641–653. [Zh. Eksp. Teor. Fiz.73,1216(1977)].

[11] **Particle Data Group** Collaboration, K. Olive et al., *Review of Particle Physics*, *Chin. Phys. C* **38** (2014) 090001.

[12] I. J. R. Aitchison and A. J. G. Hey, *Gauge theories in particle physics: A practical introduction. Vol. 2: Non-Abelian gauge theories: QCD and the electroweak theory*. Graduate student series in physics. IOP, Bristol, 2004.

[13] J. Goldstone, A. Salam, and S. Weinberg, *Broken symmetries*, *Phys. Rev.* **127** (1962) 965–970.

[14] **CMS** Collaboration, S. Chatrchyan et al., *Observation of a new boson at a mass of* 125 *GeV with the CMS experiment at the* LHC, *Phys. Lett. B* **716** (2012) 30–61, [arXiv:1207.7235].

[15] **ATLAS** Collaboration, G. Aad et al., *Observation of a new particle in the search for the Standard Model Higgs boson with the ATLAS detector at the* LHC, *Phys. Lett. B* **716** (2012) 1–29, [arXiv:1207.7214].

[16] F. Englert and R. Brout, *Dynamical theory of weak and electromagnetic interactions*, *Phys. Lett. B* **49** (1974) 77–80.

[17] P. W. Higgs, *Broken symmetries and the masses of gauge bosons*, *Phys. Rev. Lett.* **13** (1964) 508–509.

[18] C. Degrande, N. Greiner, W. Kilian, O. Mattelaer, H. Mebane, T. Stelzer, S. Willenbrock, and C. Zhang, *Effective field theory: A modern approach to anomalous couplings*, *Annals Phys.* **335** (2013) 21–32, [arXiv:1205.4231].

[19] S. Nussinov, *Colored quark version of some hadronic puzzles*, *Phys. Rev. Lett.* **34** (1975) 1286–1289.

[20] F. E. Low, *A model of the bare pomeron*, *Phys. Rev. D* **12** (1975) 163–173.

[21] V. N. Gribov, *Possible asymptotic behavior of elastic scattering*, *JETP Lett.* **41** (1961) 667–669.

[22] D. d'Enterria and G. Gil da Silveira, *Observing light-by-light scattering at the Large Hadron Collider*, *Phys. Rev. Lett.* **111** (2013) 080405, [arXiv:1305.7142].

[23] R. S. Gupta, *Probing quartic neutral gauge boson couplings using diffractive photon fusion at the* LHC, *Phys. Rev. D* **85** (2012) 014006, [arXiv:1111.3354].

[24] S. Atag, S. C. Inan, and I. Sahin, *Extra dimensions in photon-induced two lepton final states at the* CERN-LHC, *Phys. Rev. D* **80** (2009) 075009, [arXiv:0904.2687].

[25] S. Atag, S. C. Inan, and I. Sahin, *Extra dimensions in $\gamma\gamma \to \gamma\gamma$ process at the* CERN-LHC, *JHEP* **09** (2010) 042, [arXiv:1005.4792].

[26] N. Schul and K. Piotrzkowski, *Detection of two-photon exclusive production of supersymmetric pairs at the* LHC, *Nucl. Phys. Proc. Suppl.* **179-180** (2008) 289–297, [arXiv:0806.1097].

[27] D. M. Asner, J. B. Gronberg, and J. F. Gunion, *Detecting and studying Higgs bosons at a photon-photon collider*, *Phys. Rev. D* **67** (2003) 035009, [hep-ph/0110320].

[28] P. Lebiedowicz and A. Szczurek, *Exclusive production of heavy charged Higgs boson pairs in the $pp \to ppH^+H^-$ reaction at the* LHC *and a future circular collider*, *Phys. Rev. D* **91** (2015), no. 9 095008, [arXiv:1502.03323].

[29] C. F. von Weizsäcker, *Radiation emitted in collisions of very fast electrons (Ausstrahlung bei Stößen sehrschneller Elektronen)*, *Z. Phys.* **88** (1934) 612–625.

[30] E. J. Williams, *Correlation of certain collision problems with radiation theory*, *Kong. Dan. Vid. Sel. Mat. Fys. Med.* **13N4** (1935), no. 4 1–50.

[31] V. M. Budnev, I. F. Ginzburg, G. V. Meledin, and V. G. Serbo, *The two-photon particle production mechanism. Physical problems. Applications. Equivalent photon approximation*, *Phys. Rept.* **15** (1975) 181–281.

[32] F. J. Ernst, R. G. Sachs, and K. C. Wali, *Electromagnetic form factors of the nucleon*, *Phys. Rev.* **119** (1960) 1105–1114.

[33] L. N. Hand, D. G. Miller, and R. Wilson, *Electric and magnetic form factor of the nucleon*, *Rev. Mod. Phys.* **35** (1963) 335.

[34] J. R. Dunning, K. W. Chen, A. A. Cone, G. Hartwig, N. F. Ramsey, J. K. Walker, and R. Wilson, *Electromagnetic structure of the neutron and proton*, *Phys. Rev. Lett.* **13** (1964) 631–635.

[35] J. de Favereau de Jeneret, V. Lemaitre, Y. Liu, S. Ovyn, T. Pierzchala, K. Piotrzkowski, X. Rouby, N. Schul, and M. Vander Donckt, *High energy photon interactions at the* LHC, arXiv:0908.2020.

[36] D. d'Enterria and J.-P. Lansberg, *Study of Higgs boson production and its $b\bar{b}$ decay in $\gamma\gamma$ processes in proton-nucleus collisions at the* LHC, *Phys. Rev. D* **81** (2010) 014004, [arXiv:0909.3047].

[37] J. de Favereau de Jeneret, *Tests of the standard model in photoproduction at* HERA *and the* LHC. PhD thesis, Université catholique de Louvain, April, 2009.

[38] N. Schul, *Measurement of two-photon interactions at the* LHC. PhD thesis, Université catholique de Louvain, July, 2011.

[39] A. D. Martin, V. A. Khoze, and M. G. Ryskin, *Rapidity gap survival probability and total cross sections*, in *Proceedings, workshop:* HERA *and the* LHC *workshop series on the implications of* HERA *for* LHC *physics*, pp. 488–494, 2008. arXiv:0810.3560.

[40] M. Strikman and C. Weiss, *Rapidity gap survival in central exclusive diffraction: Dynamical mechanisms and uncertainties*, in *Proceedings, workshop:* HERA *and the* LHC *workshop series on the implications of* HERA *for* LHC *physics*, pp. 495–502, 2008. arXiv:0812.1053.

[41] M. G. Ryskin, A. D. Martin, and V. A. Khoze, *Soft processes at the* LHC. *II. Soft-hard factorization breaking and gap survival*, *Eur. Phys. J. C* **60** (2009) 265–272, [arXiv:0812.2413].

[42] L. A. Harland-Lang, V. A. Khoze, M. G. Ryskin, and W. J. Stirling, *The phenomenology of central exclusive production at hadron colliders*, *Eur. Phys. J. C* **72** (2012) 2110, [arXiv:1204.4803].

[43] S. Baranov, O. Duenger, H. Shooshtari, and J. Vermaseren, *LPAIR: A generator for lepton pair production*, in *Hamburg 1991, Proceedings, Physics at* HERA, vol. 3, p. 1478, 1991.

[44] J. A. M. Vermaseren, *Two-photon processes at very high energies*, *Nucl. Phys. B* **229** (1983) 347.

[45] A. Suri and D. R. Yennie, *The space-time phenomenology of photon absorption and inelastic electron scattering*, *Annals Phys.* **72** (1972) 243.

[46] H. Plothow-Besch, *PDFLIB: A library of all available parton density functions of the nucleon, the pion and the photon and the corresponding α_s calculations*, *Comput. Phys. Commun.* **75** (1993) 396–416.

[47] T. Sjöstrand, *The Lund Monte Carlo for jet fragmentation and e^+e^- physics:* Jetset *version 6.2*, *Comput. Phys. Commun.* **39** (1986) 347–407.

[48] G. Gil da Silveira, L. Forthomme, K. Piotrzkowski, W. Schäfer, and A. Szczurek, *Central $\mu^+\mu^-$ production via photon-photon fusion in proton-proton collisions with proton dissociation*, *JHEP* **1502** (2015) 159, [arXiv:1409.1541].

[49] V. V. Sudakov, *Vertex parts at very high-energies in quantum electrodynamics*, *Sov. Phys. JETP* **3** (1956) 65–71. [Zh. Eksp. Teor. Fiz. 30, 87 (1956)].

[50] G. Gil da Silveira, L. Forthomme, K. Piotrzkowski, W. Schäfer, and A. Szczurek, "pptoll, a k_T-factorisation approach generator for the two-photon production of lepton pairs at *pp* colliders." To be released.

[51] G. P. Lepage, *A new algorithm for adaptive multidimensional integration*, *J.Comput.Phys.* **27** (1978) 192.

[52] A. Szczurek and V. Uleshchenko, *Nonpartonic components in the nucleon structure functions at small Q^2 in the broad range of x_{Bj}*, *Eur. Phys. J. C* **12** (2000) 663–671, [hep-ph/9904288].

[53] M. Łuszczak, W. Schäfer, and A. Szczurek, *Two-photon dilepton production in proton-proton collisions: two alternative approaches*, arXiv:1510.00294.

[54] R. Fiore, A. Flachi, L. L. Jenkovszky, A. I. Lengyel, and V. K. Magas, *Explicit model realizing parton hadron duality*, *Eur. Phys. J. A* **15** (2002) 505–515, [hep-ph/0206027].

[55] R. W. Brown and K. O. Mikaelian, *W^+W^- and ZZ pair production in e^+e^-, pp, $p\bar{p}$ colliding beams*, *Phys. Rev. D* **19** (1979) 922.

[56] M. Łuszczak, A. Szczurek, and C. Royon, *W^+W^- pair production in proton-proton collisions: small missing terms*, *JHEP* **02** (2015) 098, [arXiv:1409.1803].

[57] M. Łuszczak, *Production of W^+W^- pairs via subleading processes at the* LHC, in *Proceedings, 2nd Conference on Large Hadron Collider Physics Conference (LHCP 2014)*, 2014. arXiv:1410.5848.

[58] P. Lebiedowicz, R. Pasechnik, and A. Szczurek, *QCD diffractive mechanism of exclusive W^+W^- pair production at high energies*, *Nucl. Phys. B* **867** (2013) 61–81, [arXiv:1203.1832].

[59] G. Belanger, F. Boudjema, Y. Kurihara, D. Perret-Gallix, and A. Semenov, *Bosonic quartic couplings at* LEP-2, *Eur. Phys. J. C* **13** (2000) 283–293, [hep-ph/9908254].

[60] M. Maniatis, A. von Manteuffel, and O. Nachtmann, *Anomalous couplings in $\gamma\gamma \to W^+W^-$ at* LHC *and* ILC, *Nucl. Phys. Proc. Suppl.* **179-180** (2008) 104–108.

[61] **OPAL** Collaboration, G. Abbiendi, C. Ainsley, P. F. Åkesson, et al., *Constraints on anomalous quartic gauge boson couplings from $\nu\bar{\nu}\gamma\gamma$ and $q\bar{q}\gamma\gamma$ events at* CERN LEP-2, *Phys. Rev. D* **70** (Aug, 2004) 032005.

[62] T. Pierzchała and K. Piotrzkowski, *Sensitivity to anomalous quartic gauge couplings in photon-photon interactions at the* LHC, *Nucl. Phys. Proc. Suppl.* **179-180** (2008) 257, [arXiv:0807.1121].

[63] O. Eboli, M. Gonzalez-Garcia, and S. Lietti, *Bosonic quartic couplings at* CERN LHC, *Phys. Rev. D* **69** (2004) 095005, [hep-ph/0310141].

[64] O. Eboli, M. Gonzalez-Garcia, and J. Mizukoshi, *$pp \to jje^\pm\mu^\pm\nu\nu$ and $jje^\pm\mu^\mp\nu\nu$ at $O(\alpha^6)$ and $O(\alpha^4\alpha_s^2)$ for the study of the quartic electroweak gauge boson vertex at* CERN LHC, *Phys. Rev. D* **74** (2006) 073005, [hep-ph/0606118].

[65] A. Belyaev, N. D. Christensen, and A. Pukhov, *CalcHEP 3.4 for collider physics within and beyond the Standard Model*, *Comput. Phys. Commun.* **184** (2013) 1729–1769, [arXiv:1207.6082].

[66] J. Alwall, M. Herquet, F. Maltoni, O. Mattelaer, and T. Stelzer, *MadGraph 5 : Going Beyond*, *JHEP* **06** (2011) 128, [arXiv:1106.0522].

[67] W. Wittmer, A. Verdier, and F. Zimmermann, *Correcting the* LHC *β^* at collisions*, *Conf. Proc.* **C030512** (2003) 2237.

[68] R. Assmann, M. Ferro-Luzzi, et al., LHC *beam parameters for the physics run at* 3.5 *TeV*, tech. rep., CERN, Geneva, Mar, 2010.

[69] Y. Papaphilippou, H. Bartosik, G. Rumolo, and D. Manglunki, *Operational beams for the* LHC, Tech. Rep. arXiv:1412.7857, CERN, Dec, 2014. Comments: Submitted for publication in a CERN *Yellow Report* (YR).

[70] E. J. N. Wilson, *An introduction to particle accelerators*. Oxford University Press, 2001.

[71] S. Y. Lee, *Accelerator physics*. World Scientific, 1999.

[72] V. Karimäki, *The CMS tracker system project: Technical Design Report*. Technical Design Report CMS. CERN, Geneva, 1997.

[73] **CMS HF Calorimeter** Collaboration, J. P. Merlo, *CMS hadronic forward calorimeter*, *Nucl. Phys. Proc. Suppl.* **61B** (1998) 41–46. [41(1998)].

[74] **TOTEM** Collaboration, G. Anelli et al., *The* Totem *experiment at the* CERN *Large Hadron Collider*, *JINST* **3** (2008) S08007.

[75] **FP420 R&D** Collaboration, M. Albrow et al., *The FP420 & Project: Higgs and new physics with forward protons at the* LHC, *JINST* **4** (2009) T10001, [arXiv:0806.0302].

[76] **CMS** Collaboration, S. Chatrchyan et al., "Luminosity results." https://twiki.cern.ch/twiki/bin/view/CMSPublic/LumiPublicResults, 2015.

[77] **CMS** Collaboration, J. Brooke, *Performance of the CMS Level-1 trigger*, *PoS* **ICHEP2012** (2013) 508, [arXiv:1302.2469].

[78] **CMS** Collaboration, S. Chatrchyan et al., *Description and performance of track and primary vertex reconstruction with the CMS tracker*, *JINST* **9** (2014), no. 10 P10009, [arXiv:1405.6569].

[79] **CMS** Collaboration, S. Chatrchyan et al., "Tracking Physics Objects Group results." https://twiki.cern.ch/twiki/bin/view/CMSPublic/PhysicsResultsTRK, 2015.

[80] **CMS** Collaboration, S. Chatrchyan et al., "Muon Physics Objects Group results." https://twiki.cern.ch/twiki/bin/view/CMSPublic/PhysicsResultsMUO, 2015.

[81] **CMS** Collaboration, S. Chatrchyan et al., *Energy calibration and resolution of the CMS electromagnetic calorimeter in pp collisions at* $\sqrt{s} = 7$ *TeV*, *JINST* **8** (2013) P09009, [arXiv:1306.2016].

[82] **CMS** Collaboration, S. Chatrchyan et al., *Performance of electron reconstruction and selection with the CMS detector in pp collisions at* $\sqrt{s} = 8$ *TeV*, *JINST* **10** (2015), no. 06 P06005, [arXiv:1502.02701].

[83] **CMS** Collaboration, S. Chatrchyan et al., *Study of exclusive two-photon production of* W^+W^- *in pp collisions at* $\sqrt{s} = 7$ *TeV and constraints on anomalous quartic gauge couplings*, *JHEP* **1307** (2013) 116, [arXiv:1305.5596].

[84] **CMS** Collaboration, S. Chatrchyan et al., *Evidence for exclusive* $\gamma\gamma \to W^+W^-$ *production and constraints on anomalous quartic gauge couplings at* $\sqrt{s} = 8$ *TeV*, Tech. Rep. CMS-PAS-FSQ-13-008, CERN, Geneva, 2015.

[85] **CMS** Collaboration, S. Chatrchyan et al., *Exclusive photon-photon production of muon pairs in proton-proton collisions at* $\sqrt{s} = 7$ *TeV*, *JHEP* **01** (2012) 052, [arXiv:1111.5536].

[86] **CMS** Collaboration, S. Chatrchyan et al., *Search for exclusive or semi-exclusive photon pair production and observation of exclusive and semi-exclusive electron pair production in pp collisions at* $\sqrt{s} = 7$ *TeV*, *JHEP* **11** (2012) 080, [arXiv:1209.1666].

[87] **ATLAS** Collaboration, G. Aad et al., *Measurement of exclusive* $\gamma\gamma \to \ell^+\ell^-$ *production in proton-proton collisions at* $\sqrt{s} = 7$ *TeV with the ATLAS detector*, *Phys. Lett. B* **749** (2015) 242–261, [arXiv:1506.07098].

[88] A. G. Shamov and V. I. Telnov, *Two-photon lepton pair production for luminosity determination at* LHC, in *Forward physics and luminosity determination at* LHC. *Proceedings, Workshop, Helsinki, Finland, October 31-November 4, 2000*, pp. 136–143, 2000.

[89] S. van der Meer, *Calibration of the effective beam height in the ISR*, Tech. Rep. CERN-ISR-PO-68-31. ISR-PO-68-31, CERN, Geneva, 1968.

[90] C. Rubbia, *Measurement of the luminosity of* $p\bar{p}$ *collider with a (generalized)* van der Meer *method*, Tech. Rep. CERN-$p\bar{p}$-Note-38, CERN, Geneva, Nov, 1977.

[91] **LHC Programme Coordination** Collaboration, H. Burkhardt et al., "General information about luminosity calibration at the LHC." https://lpc.web.cern.ch/lpc/lumicalib.htm.

[92] **CMS** Collaboration, S. Chatrchyan et al., *Absolute calibration of luminosity measurement at CMS: Summer 2011 update*, .

[93] **CMS** Collaboration, S. Chatrchyan et al., *CMS luminosity based on pixel cluster counting - Summer 2013 update*, Tech. Rep. CMS-PAS-LUM-13-001, CERN, Geneva, 2013.

[94] **CDF** Collaboration, R. D. Field, *The underlying event in hard scattering processes*, *eConf* **C010630** (2001) P501, [hep-ph/0201192].

[95] **CMS** Collaboration, S. Chatrchyan et al., *Measurement of the underlying event in the Drell-Yan process in proton-proton collisions at* $\sqrt{s} = 7$ *TeV*, *Eur. Phys. J. C* **72** (2012) 2080, [arXiv:1204.1411].

[96] S. Alioli, P. Nason, C. Oleari, and E. Re, *A general framework for implementing NLO calculations in shower Monte Carlo programs: the* POWHEG *BOX*, *JHEP* **06** (2010) 043, [arXiv:1002.2581].

[97] T. Sjöstrand, S. Mrenna, and P. Z. Skands, *Pythia 6.4 physics and manual*, *JHEP* **05** (2006) 026, [hep-ph/0603175].

[98] G. Gil da Silveira, L. Forthomme, J. Hollar, K. Piotrzkowski, and F. Rebassoo, *Search for the exclusive two-photon production of* W^+W^- *in pp collisions at 7 TeV*, Tech. Rep. CMS-FSQ-12-010, CERN, Geneva, Feb, 2013.

[99] G. Gil da Silveira, L. Forthomme, J. Hollar, C. Mora, K. Piotrzkowski, F. Rebassoo, P. Rebello Teles, and D. Wright, *Study of exclusive two-photon production of* W^+W^- *in pp collisions at* $\sqrt{s} = 8$ *TeV and constraints on anomalous quartic gauge couplings*, Tech. Rep. CMS-AN-13-259, CERN, Geneva, Sep, 2015.

[100] **Dø** Collaboration, V. M. Abazov et al., *Search for anomalous quartic* $WW\gamma\gamma$ *couplings in dielectron and missing energy final states in* $p\bar{p}$ *collisions at* $\sqrt{s} = 1.96$ *TeV*, *Phys. Rev. D* **88** (May, 2013) 012005, [arXiv:1305.1258].

[101] G. J. Feldman and R. D. Cousins, *A unified approach to the classical statistical analysis of small signals*, *Phys. Rev. D* **57** (1998) 3873, [physics/9711021].

[102] **CMS** Collaboration, S. Chatrchyan et al., *Search for* $WW\gamma$ *and* $WZ\gamma$ *production and constraints on anomalous quartic gauge couplings in pp collisions at* $\sqrt{s} = 8$ *TeV*, *Phys. Rev. D* **90** (2014), no. 3 032008, [arXiv:1404.4619].

[103] **CMS** Collaboration, S. Chatrchyan et al., *Evidence for the electroweak* $Z\gamma$ *production in association with two jets and a search for anomalous quartic gauge couplings in pp collisions at* $\sqrt{s} = 8$ *TeV*, Tech. Rep. CMS-PAS-SMP-14-018, CERN, Geneva, 2015.

[104] **CMS** Collaboration, S. Chatrchyan et al., *Study of vector boson scattering and search for new physics in events with two same-sign leptons and two jets*, *Phys. Rev. Lett.* **114** (2015), no. 5 051801, [arXiv:1410.6315].

[105] **CMS** Collaboration, S. Chatrchyan et al., "Limits on anomalous triple and quartic gauge couplings." https://twiki.cern.ch/twiki/bin/view/CMSPublic/PhysicsResultsSMPaTGC, 2015.

[106] J. Alwall, R. Frederix, S. Frixione, V. Hirschi, F. Maltoni, O. Mattelaer, H. S. Shao, T. Stelzer, P. Torrielli, and M. Zaro, *The automated computation of tree-level and next-to-leading order differential cross sections, and their matching to parton shower simulations*, *JHEP* **07** (2014) 079, [arXiv:1405.0301].

[107] L. Forthomme, *Exploratory study of two-photon production of Z pairs at 8 TeV*, Tech. Rep. CMS-AN-15-337, CERN, Geneva, Jan, 2016.

[108] **DELPHI, OPAL, ALEPH, LEP Electroweak Working Group, L3** Collaboration, M. W. Grünewald et al., *A combination of preliminary electroweak measurements and constraints on the standard model*, hep-ex/0511027.

[109] J. Pumplin, D. R. Stump, J. Huston, H. L. Lai, P. M. Nadolsky, and W. K. Tung, *New generation of parton distributions with uncertainties from global QCD analysis*, *JHEP* **07** (2002) 012, [hep-ph/0201195].

[110] R. Rahmat, R. Kroeger, and A. Giammanco, *The fast simulation of the CMS experiment*, *J. Phys. Conf. Ser.* **396** (2012) 062016.

[111] **CMS-TOTEM** Collaboration, M. Albrow, M. Arneodo, et al., *CMS-*Totem *Precision Proton Spectrometer*, Tech. Rep. CERN-LHCC-2014-021. TOTEM-TDR-003. CMS-TDR-13, CERN, Geneva, Sep, 2014.

[112] K. Piotrzkowski, *Tagging two photon production at the* cern-lhc, *Phys. Rev. D* **63** (2001) 071502, [hep-ex/0009065].

[113] **TOTEM** Collaboration, G. Antchev et al., *First measurement of the total proton-proton cross section at the* lhc *energy of* $\sqrt{s} = 7$ *TeV*, *Europhys. Lett.* **96** (2011) 21002, [arXiv:1110.1395].

[114] **TOTEM** Collaboration, G. Antchev et al., *Luminosity-independent measurement of the proton-proton total cross section at* $\sqrt{s} = 8$ *TeV*, *Phys. Rev. Lett.* **111** (2013), no. 1 012001.

[115] **CMS-TOTEM** Collaboration, S. Chatrchyan et al., *Measurement of pseudorapidity distributions of charged particles in proton-proton collisions at* $\sqrt{s} = 8$ *TeV by the CMS and* Totem *experiments*, *Eur. Phys. J. C* **74** (2014), no. 10 3053, [arXiv:1405.0722].

[116] **CMS** Collaboration, S. Chatrchyan et al., *Pseudorapidity distribution of charged hadrons in proton-proton collisions at* $\sqrt{s} = 13$ *TeV*, *Phys. Lett. B* **751** (2015) 143–163, [arXiv:1507.05915].

[117] G. Gil da Silveira and V. P. Gonçalves, *Constraining the photon flux in two-photon processes at the* lhc, *Phys. Rev. D* **92** (2015), no. 1 014013, [arXiv:1506.01352].

[118] M. Albrow, H. Kim, S. Los, M. Mazzillo, E. Ramberg, A. Ronzhin, V. Samoylenko, H. Wenzel, and A. Zatserklyaniy, *Quartz Cerenkov counters for fast timing:* Quartic, *JINST* **7** (2012) P10027, [arXiv:1207.7248].

[119] L. Bonnet, T. Pierzchała, K. Piotrzkowski, and P. Rodeghiero, *GasToF: Ultra-fast ToF forward detector for exclusive processes at the* lhc, *Acta Phys.Polon. B* **38** (2007) 477–482, [hep-ph/0703320].

[120] L. Bonnet, J. Liao, and K. Piotrzkowski, *Study on GasToF: A 10 ps resolution timing detector*, *Nucl. Instrum. Meth. A* **762** (2014) 77–84.

[121] N. Cartiglia, C. Royon, et al., LHC *Forward Physics*, tech. rep., CERN, Sep, 2015. Comments: Submitted for publication in a CERN *Yellow Report* (YR).

[122] Photonis Inc., Lancaster, USA, *Planacon® XP85112 Photon Detector*, Jan, 2013. Rev. 03.

[123] F. Anghinolfi, P. Jarron, A. Martemyanov, E. Usenko, H. Wenninger, et al., *NINO: An ultra-fast and low-power front-end amplifier/discriminator ASIC designed for the multigap resistive plate chamber*, *Nucl. Instrum. Meth. A* **533** (2004) 183–187.

[124] M. Despeisse, P. Jarron, F. Anghinolfi, S. Tiuraniemi, F. Osmic, P. Riedler, A. Kluge, and A. Ceccucci, *Low-power amplifier-discriminators for high time resolution detection*, in *Proceedings, 2008 IEEE Nuclear Science Symposium and Medical Imaging Conference and 16th International Workshop on Room-Temperature Semiconductor X-Ray and Gamma-Ray Detectors (NSS/MIC 2008 / RTSD 2008)*, pp. 1820–1826, 2008.

[125] PICMG®, *Micro Telecommunications Computing Architecture® Short Form Specification*, Sep, 2006. Rev. 1.0.

[126] J. de Favereau, X. Rouby, and K. Piotrzkowski, *Hector: A fast simulator for the transport of particles in beamlines*, *JINST* **2** (2007) P09005, [arXiv:0707.1198].

[127] H. Grote and F. Schmidt, *MAD-X: An upgrade from MAD8*, *Conf. Proc.* **C030512** (2003) 3497.

[128] **LHC Optics** Collaboration, J. M. Jowett et al., "LHC optics web repository." http://cern.ch/lhcoptics, 2015.

[129] **GEANT4** Collaboration, S. Agostinelli et al., *Geant4: A simulation toolkit*, *Nucl. Instrum. Meth. A* **506** (2003) 250–303.

[130] **ZEUS** Collaboration, K. Piotrzkowski and U. Schneekloth, *Photoproduction tagger at* 44 m, tech. rep., DESY, Hamburg, Mar, 1994.

[131] M. Renaud, *Studies of GasToF: New, ultra-fast timing detector for the CMS experiment at* LHC, Master's thesis, Université catholique de Louvain, September, 2015.

[132] **TOTEM** Collaboration, G. Antchev et al., *Timing Measurements in the vertical Roman pots of the* TOTEM *experiment*, Tech. Rep. CERN-LHCC-2014-020. TOTEM-TDR-002, CERN, Geneva, Sep, 2014.

[133] M. Boonekamp, A. Dechambre, V. Juranek, O. Kepka, M. Rangel, et al., *FPMC: A generator for forward physics*, arXiv:1102.2531.

[134] G. Corcella, I. G. Knowles, G. Marchesini, S. Moretti, K. Odagiri, P. Richardson, M. H. Seymour, and B. R. Webber, *Herwig 6: An event generator for hadron emission reactions with interfering gluons (including supersymmetric processes)*, *JHEP* **01** (2001) 010, [hep-ph/0011363].

[135] S. Baranov, O. Duenger, H. Shooshtari, and J. Vermaseren, "LPAIR source code." https://github.com/forthommel/lpair, 2016.

[136] L. Forthomme, *CepGen: Reference manual*. Liège, Belgium, Jan, 2016. Rev. 0.5, available at http://lforthom.web.cern.ch/lforthom/work/cepgen/refman.pdf.

[137] M. Galassi, J. Davies, J. Theiler, B. Gough, G. Jungman, M. Booth, and F. Rossi, GNU *Scientific Library: Reference manual*. Network Theory Ltd., Feb., 2003.

[138] J. von Neumann, *Various techniques used in connection with random digits*, *Nat. Bureau of Standards (U.S.), Applied Mathematics Series* **12** (1951) 36–38.

[139] A. Szczurek and M. Łuszczak, *Subleading processes in production of W^+W^- pairs in proton-proton collisions*, in *Proceedings, 2015 European Physical Society Conference on High Energy Physics (EPS-HEP 2015)*, 2015. arXiv:1510.04570.

[140] B. List and A. Mastroberardino, *DIFFVM: A Monte Carlo generator for diffractive processes in ep scattering*, *Conf. Proc.* **C980427** (1998) 396–404.

[141] V. Brigljevic et al., *Using XDAQ in application scenarios of the CMS experiment*, *eConf* **C0303241** (2003) MOGT008, [hep-ex/0305076].

[142] CAEN S.p.A., Viareggio, Italy, *V1290A/N & VX1290A/N (32/16 channel multihit TDCs) Technical Information Manual*, Jul, 2012. Rev. 15.

[143] CAEN S.p.A., Viareggio, Italy, *V1495 (general purpose VME board) Technical Information Manual*, Jun, 2015. Rev. 16.

[144] CT-PPS test beam SW working group, "Run control for the CT-PPS test beam at SPS." https://github.com/pps-tb-sw/pps-tbrc, 2015.